

A review of aerodynamic flow models, solution methods and solvers – and their applicability to aircraft conceptual design

Literature study report

B. Peerlings

November 1, 2018

A review of aerodynamic flow models, solution methods and solvers – and their applicability to aircraft conceptual design

Literature study report

by

B. (Bram) Peerlings

in partial fulfilment of the requirements for the degrees of

Master of Science
in Aerospace Engineering

Student number	4079388
Project duration	June 4, 2018 – September 5, 2018 October 8, 2018 – November 1, 2018
Department	Flight Performance & Propulsion, faculty of Aerospace Engineering
Supervisor	dr. ir. R. Vos

Electronic versions of this document suitable for screen and print are available at bram.peerlings.me/en/literature-study/, using the password 'AE4020-2018'.

Contents

Preface	v
Summary	vii
List of figures	ix
List of tables	xi
List of abbreviations	xiv
List of symbols	xviii
1 Introduction	1
2 Overview of flow models	3
2.1 Navier-Stokes equations	5
2.1.1 Direct numerical simulation (DNS).	8
2.1.2 Large eddy simulation (LES).	8
2.1.3 Unsteady Reynolds-averaged Navier-Stokes equations (URANS)	8
2.1.4 Reynolds-averaged Navier-Stokes equations (RANS)	9
2.1.5 Thin-layer Navier-Stokes equations (TLNS).	9
2.1.6 Turbulence modelling	10
2.2 Boundary layer equations	10
2.3 Euler equations	11
2.4 Full potential equation	12
2.5 Linearised potential equation	13
2.6 Laplace's equation	14
2.7 Empirical methods	14
3 Overview of solution methods	15
3.1 Non-linear solution methods	15
3.1.1 Finite difference methods (FDM).	15
3.1.2 Finite element methods (FEM).	16
3.1.3 Finite volume methods (FVM)	16
3.2 Linear solution methods	16
3.2.1 Lifting line and lifting surface theory (LLT / LST)	17
3.2.2 Vortex lattice method (VLM)	18
3.2.3 Panel method	18
3.3 Boundary conditions	19
3.3.1 Far-field boundary conditions	20
3.3.2 Surface boundary conditions.	20
3.3.3 Numerical implementation	21
4 Overview of solvers	23
4.1 Two-dimensional solvers	26
4.1.1 XFOIL	26
4.1.2 Viscous Garabedian and Korn (VGK)	30
4.1.3 MSES	37
4.1.4 Ames Research Center 2D (ARC2D)	39
4.1.5 Comparative review	43

4.2	Three-dimensional solvers	45
4.2.1	Athena Vortex Lattice (AVL)	45
4.2.2	Tornado	46
4.2.3	Vortex Separation Aerodynamics (VSAERO)	49
4.2.4	MATRICS / -V	53
4.2.5	Stanford University Unstructured (SU2)	59
4.2.6	Comparative review	64
4.3	Hybrid two-/three-dimensional solvers	67
4.3.1	XFLR5	67
4.3.2	Quasi-three-dimensional aerodynamic solver (Q3D)	69
4.3.3	Comparative review	72
5	Applicability to conceptual design	73
6	Conclusions	77
7	Discussion	81
7.1	Limitations of current research	81
7.2	Recommendations for future research and development	81
8	Research outlook	83
8.1	Research goal and questions	83
8.2	Methodology	84
8.3	Planning	86
	Bibliography	89

Preface

To many a student, having to do a literature review is – simply put – a pain and something they dread. Telling friends how I have started the work on this review before summer, I am often greeted with somewhat of a pitiful look. And, to be honest, I had not exactly been looking forward to it myself.

Luckily, things turned out quite different and I am happy with as well as proud of the report that currently lies before you. Fellow students at Science Communication showed me how to best go about an assignment like this and even managed to get me to like doing these reviews. Browsing older or newer reports or articles, coming across other researchers struggling with the same problem as yourself, or having found a solution idea you so desperately needed turns out to be very rewarding! Most of the days working on this review, I found myself going home feeling a little smarter and better understanding the subject matter – aerodynamic flow models, solution methods and aerodynamic solver codes. I managed to shine a light in (most of) these previously black boxes and uncovered similarities, differences and trends. Particularly fascinating was to review how various researchers think about the use of these models and tools in the conceptual design phase and how they see that field of engineering developing. As you will more formally read in the introduction, these four topics form the pillars of this report.

Two other things about reading this report I would like to discuss in this preface. First of all: the report is best viewed in colour. There are some figures so densely packed with information, that it was simply impossible to not use colour to discern between different data sets. A further advantage is that reading this document in colour makes the in-text citations stand out, so that it becomes much easier to skip over the citation and quickly get back on track with the remainder of the sentence. It is hoped that this improves the readability of the report and makes the citations distract as little as possible. Citations form a second aspect relevant to discuss in this reading guide. Contrary to the numerical citations customary in the aerospace industry (especially in publications by the American Institute of Aeronautics and Astronautics), I have chosen for author-year-citations. I feel having this information in-text is a massive benefit, as it immediately shows how recent (or old) a reference is (and, by extension, how recent an idea or development is) and allows to identify authors throughout reading this report. Also, some additional references are included that point to a more extensive discussion of the topic at hand. In most of these cases, the citation also includes reference to a chapter, section or page, to help find the relevant information sooner.

Last, I would like to take the opportunity to express my gratitude to a number of people – without whom this review would not have been as complete, thorough or focused. First of all, thanks to Roelof Vos, Maurice Hoogreef and Martijn Roeloefs for suggesting aerodynamic solvers to include. A second and well-deserved word of appreciation goes out to Martijn, for his extensive and valuable feedback on an earlier version of this report, which has especially helped me in further improving the various comparative reviews. Last, I would like to thank Roderick Schildkamp, for pointing me to the wonderful book on computational aerodynamics by [Cummings et al.](#). It has helped solve many mysteries and was instrumental in the aforementioned moments of increased understanding of the subject matter that is presented here.

Bram Peerlings
Delft, November 1, 2018

Summary

This literature study report is written in preparation for a subsequent graduation research project that aims to develop a methodology for uncertainty quantification in (aerodynamic) models, in order to contribute to improve decisions made in the conceptual aircraft design process. In the current text, the assumptions, simplifications and limitations of various aerodynamic solvers have been investigated, as well as their performance compared. A more fundamental discussion of flow models (from Navier-Stokes to Laplace's equation) and non-linear (FDM, FEM, FVM) and linear (LLT, VLM, panel methods) solution methods precede an analysis of 11 solvers of different fidelity levels.

Of the two-dimensional codes, XFOIL (panel method and boundary layer model), VGK (full potential FDM and BL model), MSES (Euler FVM and BL model) and ARC2D (thin-layer NS using FDM) were investigated. In three dimensions, the research comprised vortex lattice methods VLM and Tornado, VSAERO (panel method and BL model), MATRICS-V (full potential FVM and BL model) and SU2 (Euler, inviscid NS and turbulent RANS using FVM or FEM). XFLR5 and Q3D, combining 2D boundary layer models with 3D linear potential codes, were classified as 'hybrid' solvers and analysed. Given their different flow models, these codes most notably vary in terms of including viscosity, the applicable Mach number range and limitations to geometry modelling.

Unsurprisingly, it was concluded that the higher-fidelity codes generally match experimental results best. In 2D codes, predicting shock strength and shock location were found to be most difficult. The 3D codes mostly differentiated themselves based on the geometric detail that could be modelled. In this case, higher-fidelity models more clearly outperformed lower-fidelity codes. Problems with accurately predicting transition and separation (insofar supported by the computational tool in question) were – to a greater or lesser extent – seen throughout the entire range of solvers considered.

The downside of these higher-fidelity codes is their increased computational cost – both directly in terms of computer time and indirectly because of preparatory work, such as geometry modelling and meshing. Although various authors see application of more advanced CFD codes earlier in the (conceptual) design process as a key towards enabling technologies such as early MDO, others believe conceptual design should remain focused on the high-level parameters and not pay too much attention the details. Also, scholars feel that current (drafting-based) CAD-software suitable for generating detailed enough geometries required by advanced simulations are unsuitable for rapid design and iteration common in conceptual design. In conclusion, it is felt a lower limit is set by the requirement that a solver should be able to definitively distinguish between concepts and a (currently fairly stringent) upper limit by computational cost and geometry requirements.

List of figures

2.1	Hierarchical overview of aerodynamic flow models	4
2.2	Boundary layer properties	11
3.1	Elementary flow solutions	17
3.2	Superposition of a finite number of horseshoe vortices along the lifting line, showing the trailing-vortex system	18
3.3	Distributed horseshoe vortices over a swept wing with 12 panels	19
3.4	Panelling of a McDonnell Douglas DC-10 jet transport	19
3.5	Surface and far-field boundary conditions on an airfoil in inviscid flow	21
3.6	Panel representation of an airplane, showing a single control point for boundary layer application	21
4.1	Airfoil and wake panels in XFOIL, showing panel numbering and singularity distributions	26
4.2	Comparison of lift and drag coefficient for the HTR 1555 inboard rotor airfoil as predicted by XFOIL and found in experiment	30
4.3	Physical and computing planes in VGK	33
4.4	Comparison of incidence angle, moment coefficient and drag coefficient as predicted by VGK and found in experiment	35
4.5	Coordinate transformation in ARC2D	41
4.6	Comparison of experimental and numerical results for a NACA0012 airfoil	42
4.7	Comparison of aerodynamic coefficients as predicted by AVL and PAN AIR	47
4.8	Comparison between a vortex sling as applied in Tornado and a horseshoe vortex as applied in most other VLMs	48
4.9	Comparison of lift coefficient variation with angle of attack as predicted (inviscid and viscous) by Tornado and found in experiment	49
4.10	Comparison of pressure coefficients of a DLR-F4 wing-body configuration as predicted by MATRICS-V and found in experiment	59
4.11	Comparison between geometric representations using a 3D panel method (PAN AIR) and a vortex lattice method (AVL)	65
4.12	Vortex lattice method implementations	68
4.13	Comparison of aerodynamic coefficients for a NACA 24-30-0 wing at subsonic speed as predicted by Q3D, VSAERO and MATRICS-V and found in experiment	71
5.1	Traditional (drafting) versus parametric design	75
5.2	Possible combinations of lower and upper fidelity limits	75
6.1	Hierarchical overview of aerodynamic solvers	78
8.1	N ² -diagram of the Aircraft Design Initiator	85
8.2	Graduation research project planning	87

List of tables

4.1	Overview of solvers	24
4.2	Combinations of flow model(s) and solution method(s) used in solvers	25
4.3	Boundary conditions supported by the compressible and incompressible RANS solver in SU2	61
8.1	Prioritised testing matrix, showing which insights about assumptions or modelling differences are gained from comparisons	84

List of Abbreviations

Abbreviation	Definition
AE	Aerospace Engineering
AIC	Aerodynamic Influence Coefficient matrix
ARC2D	Ames Research Center 2D
ARC3D	Ames Research Center 3D
ARS	Algebraic Reynolds-Stress
AVL	Athena Vortex Lattice
BL	Boundary Layer
CAD	Computer Aided Design
CFD	Computational Fluid Dynamics
DDES	Delayed Detached Eddy Simulation
DERA	Defence Evaluation and Research Agency
DES	Detached Eddy Simulation
DLR	German Aerospace Centre (Deutsches Zentrum für Luft- und Raumfahrt)
DNS	Direct Numerical Simulation
ESDU	Engineering Sciences Data Unit
FAS	Full Approximation Storage
FDM	Finite Difference Method
FEM	Finite Element Method
FVM	Finite Volume Method
ILU	Incomplete Lower Upper decomposition
JST	Jameson, Schmidt & Turkel (numerical scheme)
L0, L1, L2, L3	Fidelity level 0 (low) to 3 (high)
LES	Large Eddy Simulation
LEVMI	Linear Eddy-Viscosity Model
LLT	Lifting Line Theory
LST	Lifting Surface Theory
MATRICES	Multi-component Aircraft Transonic Inviscid Computation System
MAV	Micro Aerial Vehicle
MIT	Massachusetts Institute of Technology
NACA	National Advisory Committee for Aeronautics
NASA	National Aeronautics and Space Agency
NLR	Netherlands Aerospace Centre (former National Aerospace Laboratory)
NS	Navier-Stokes
ODE	Ordinary Differential Equation
ONERA	French Aerospace Centre (Office National d'Etudes et de Recherches Aérospatiales)
PAN AIR	Panel Aerodynamics
PDE	Partial Differential Equation
PMARC	Panel Method Ames Research Center
Q3D	Quasi-three-Dimensional aerodynamic solver
RAE	Royal Aircraft Establishment
RANS	Reynolds-Averaged Navier-Stokes
RMS	Reynolds-Stress Model
RST	Reynolds-Stress Transport
S-A	Spalart-Allmaras (turbulence model)

Abbreviation	Definition
SC	Science Communication
SIP	Strongly Implicit Procedure
SST	Menter Shear Stress Transport (turbulence model)
STOL	Short Take-Off and Landing
SU2, SU ²	Stanford University Unstructured
TE	Trailing Edge
TLNS	Thin-Layer Navier-Stokes
TRANS	Transient Reynolds-Averaged Navier-Stokes
T-S	Tollmien-Schlichting (instability wave)
UAV	Unmanned Aerial Vehicle
URANS	Unsteady Reynolds-Averaged Navier-Stokes
VGK	Viscous Garabedian and Korn
VII	Viscous-Inviscid Interaction
VLM	Vortex Lattice Method
VSAERO	Vortex Separation Aerodynamics

List of Symbols

Latin symbols

Symbol	Context	Definition	Unit
$3c/4$		Three-quarter chord point	[-]
a		Acceleration	[m/s ²]
a		Speed of sound	[m/s]
AR		Aspect ratio, b^2/S	[-]
b		Wing span	[m]
C	MATRICES / -V	Crossflow factor	[-]
c		Chord length	[m]
$c/4$		Quarter chord point	[-]
C^*	VSAERO	Unnamed parameter, Equation (4.22)	[-]
C_τ	XFOIL, MSES	Shear stress coefficient	[-]
$C_{\tau_{EQ}}$	XFOIL, MSES	Equilibrium shear stress coefficient	[-]
C_{D_f}		Skin friction drag coefficient	[-]
C_{D_p}		Pressure drag coefficient	[-]
C_{D_v}		Viscous drag coefficient	[-]
C_{D_w}		Wake drag coefficient	[-]
C_{f1}	MATRICES / -V	Skin friction drag coefficient in x -direction	[-]
C_{f2}	MATRICES / -V	Skin friction drag coefficient in y -direction	[-]
$c_{l,max}$		Maximum 2D lift coefficient	[-]
C_D		3D drag coefficient	[-]
C_D	XFOIL	Dissipation coefficient	[-]
c_d		2D drag coefficient	[-]
C_E	MATRICES / -V	Entrainment coefficient	[-]
C_f		Skin friction coefficient	[-]
c_f		Local skin friction coefficient	[-]
C_L		3D lift coefficient	[-]
c_l		2D lift coefficient	[-]
c_m		2D pitching moment coefficient	[-]
C_p		Specific heat at constant temperature	[J/K]
c_p		Pressure coefficient	[-]
d_{ij}	XFOIL	Mass-influence matrix (panel i on j)	[-]
D_S	MATRICES / -V	Spurious drag	[N]
$D_{W_{sr}}$	MATRICES / -V	Shock remainder wave drag	[N]
D_{W_G}	MATRICES / -V	Garabedian wave drag	[N]
D_i	MATRICES / -V	Induced drag	[N]
E	SU2	Total energy per unit mass	[J/kg]
e		Internal energy	[J]
F		Force	[N]
f, f		Body force	[N]
F^C	SU2	Convective fluxes	[-]
F^V	SU2	Viscous fluxes	[-]
Fr		Froude number	[-]
H	SU2	Enthalpy	[J]
H	XFOIL	Boundary layer shape parameter, δ^*/θ	[-]

Symbol	Context	Definition	Unit
\bar{H}	VGK	Transformed boundary layer shape parameter	[-]
H^*	XFOIL	Boundary layer kinetic energy shape parameter, θ^*/θ	[-]
H^{**}	XFOIL	Boundary layer density shape parameter, δ^{**}/θ	[-]
H_{avg}	MSES	Average boundary layer shape parameter	[-]
h_1, h_2	MATRICS / -V	Coordinate system coefficients	[-]
H_k	XFOIL	Boundary layer kinematic shape parameter, constant boundary layer density	[-]
i		Identifier (node, panel, ...)	[-]
J	MATRICS / -V	Jacobian for transformation from physical to computational domain	[-]
K	VSAERO	Factor for the local contribution to ϕ	[-]
k		Thermal conductivity	[W/(mK)]
k		Turbulent kinetic energy	[J]
k_1, k_2, k_3	MATRICS / -V	Coordinate system coefficients	[-]
L		Lift force	[N]
l_1, l_2, l_3	MATRICS / -V	Coordinate system coefficients	[-]
M		Mach number	[-]
m		Mass	[kg]
\dot{m}	VGK	Mass flow	[-]
m_j	XFOIL	Mass defect at panel j	
N	XFOIL	Number of surface panels	[-]
n, \tilde{n}, N	XFOIL, VGK, MSES	Logarithm of the amplification factor of the frequency of the most unstable Tollmien- Schlichting wave	[-]
\mathbf{n}		Surface normal vector	[-]
n_{crit}	XFOIL	Logarithm of the amplification factor of the frequency of the most unstable Tollmien- Schlichting wave at which transition is forced	[-]
N_w	XFOIL	Number of wake panels	[-]
n_x	MATRICS / -V	Downstream pointing normal on the shock remainder surfaces S	[-]
P	VSAERO	Position in flowfield	[-]
P	MATRICS / -V	Artificial viscosity flux in x -direction	[-]
\bar{P}	MATRICS / -V	Reference artificial velocity flux in x -direction, $\bar{P} \sim u/q$	[-]
p		Pressure	[N/m ²]
p_d	MATRICS / -V	Pressure downstream of the shock remainder	[N/m ²]
p_u	MATRICS / -V	Pressure upstream of the shock remainder	[N/m ²]
Pr		Prandtl number	[-]
Q	MATRICS / -V	Artificial viscosity flux in y -direction	[-]
\bar{Q}	MATRICS / -V	Reference artificial velocity flux in y -direction, $\bar{Q} \sim v/q$	[-]
\mathbf{Q}	ARC2D	State vector	[kg/m ³ , kg/(sm ²), kg/(sm ²), J]
q	MATRICS / -V	(Total) velocity	[m/s]
\dot{q}		Heat transfer per unit time and unit area	[J/(sm ²)]
q_{nd}	MATRICS / -V		[m/s]
q_e	MATRICS / -V		[m/s]
q_s	MATRICS / -V	Local streamwise acceleration	[m/s]
R	MATRICS / -V	Artificial viscosity flux in z -direction	[-]

Symbol	Context	Definition	Unit
\bar{R}	MATRICS / -V	Reference artificial velocity flux in z -direction, $\bar{R} \sim w/q$	[-]
r	VSAERO	Length of r	[m]
\mathbf{r}	VSAERO	Position vector of point A relative to point B	[m, m, m]
Re		Reynolds number	[-]
Re_θ	XFOIL	Boundary layer momentum thickness Reynolds number	[-]
$Re_{\theta c}$	SU2	Critical Reynolds number	[-]
s		Local streamwise coordinate, distance along surface	[m]
S_S	MATRICS / -V	Upstream surfaces of shock remainders	[-]
S_T	MATRICS / -V	Trefftz plane	[-]
T		Temperature	[K]
t		Time	[s]
t/c		Thickness to chord ratio, relative thickness	[-]
\mathbf{U}	SU2	State vector	[kg/m ³ , kg/(sm ²), kg/(sm ²), kg/(sm ²), kg J/m ³]
u		Velocity-component in x -direction	[m/s]
u'		Perturbation velocity-component in x -direction	[m/s]
u_{INV}	XFOIL	Inviscid edge velocity distribution	[m/s]
u_d	MATRICS / -V		[m/s]
u_u^*	MATRICS / -V	Velocity (in x -direction) at sonic shock piont	[m/s]
v		Velocity-component in y -direction	[m/s]
v'		Perturbation velocity-component in y -direction	[m/s]
\mathbf{V}, V		Velocity	[m/s]
$V_{M>1}$	MATRICS / -V	Supersonic enclosure in the flow	[-]
V_{out}		Velocity at outflow boundary of computational domain	[m/s]
V_n	VSAERO	Velocity normal to surface	[m/s]
w		Velocity-component in z -direction	[m/s]
w'		Perturbation velocity-component in z -direction	[m/s]

Greek symbols

Symbol	Context	Definition	Unit
α		Angle of attack	[rad]
α_i		Induced angle of attack	[rad]
β		Sideslip angle	[rad]
β^2	SU2	Artificial compressibility parameter	[-]
β_w	MATRICS / -V	Sideslip angle of the wake	[rad]
δ		Nominal boundary layer thickness	[m]
$\delta(x, y)$	LST	Vortex sheet strength	[m/s]
δ^*		Boundary layer displacement thickness	[m]
δ_ρ	MATRICS / -V	Boundary layer density thickness, $\delta_\rho = \int (\rho_e - \rho)/\rho_e$	[-]
δ_i	MATRICS / -V	Boundary layer mass integral thickness, in x - (1) or y -direction (2)	[-]
δ_{ij}	SU2	Kronecker delta function	[-]
ϵ		Dissipation rate of turbulent kinetic energy	[J/s]

Symbol	Context	Definition	Unit
η		Thin shear layer coordinate (parallel to surface)	[m]
Γ		Circulation	[-]
γ		Heat capacity ratio	[-]
γ	SU2	Intermittency	[-]
$\gamma(x, y)$	LLT, LST	Vortex sheet strength	[m/s]
γ_{0_i}	XFOIL	Vortex strength at $\alpha = 0^\circ$	[m/s]
γ_{90_i}	XFOIL	Vortex strength at $\alpha = 90^\circ$	[m/s]
Γ_i	VLM	Horseshoe vortex strength on panel i	[m/s]
λ		Bulk viscosity coefficient	[-]
λ	VGK	Pressure gradient parameter	[-]
μ		Molecular viscosity coefficient	[Ns/m ²]
μ	VSAERO	Doublet singularity density	[m ² /s]
μ^*	SU2	Molecular viscosity coefficient	[Ns/m ²]
μ_P	VSAERO	Doublet singularity density pertaining to the point P	[m ² /s]
μ_W	VSAERO	Doublet singularity density pertaining to the wake outer edge of the boundary layer	[m ² /s]
ν		Kinematic viscosity coefficient, μ/ρ	[m ² /s]
ω		Dissipation rate of turbulent kinetic energy per unit energy	[1/s]
Ω	SU2	Computational domain	[-]
ϕ		Velocity potential	[m ² /s]
ϕ_l	VSAERO	Lower surface velocity potential	[m ² /s]
ϕ_u	VSAERO	Upper surface velocity potential	[m ² /s]
ρ		Density	[kg/m ³]
σ	VSAERO	Source singularity density	[m ² /s]
τ_{ij}		Stress in i -direction on a plane perpendicular to j	[N/m ²]
θ		Boundary layer momentum thickness	[m]
θ_{ij}	MATRICS / -V	Boundary layer momentum integral thickness, in x, y -direction	[m]
ξ		Vorticity	[rad/s]
ξ		Thin shear layer coordinate (perpendicular to surface)	[m]

Common subscripts

Subscript	Definition
0	Static
<i>dyn</i>	Dynamic
<i>e</i>	Edge of the boundary layer
<i>exit</i>	Exit of the wake
<i>i</i>	Identifier (node, panel, ...)
<i>TE</i>	Trailing edge
<i>tot</i>	Total
<i>turb</i>	Turbulent
<i>x</i>	In x -direction
<i>y</i>	In y -direction
<i>z</i>	In z -direction
∞	Freestream
*	Sonic conditions (MATRICES / -V)

1

Introduction

Models come in a variety of shapes and sizes. Although all are aimed to describe the world around us – or part thereof – their uses are vastly different, resulting in differences in model complexity and uncertainty. Especially when using models for decision making, it is of utmost importance to be aware of the inner workings, assumptions and methods, in order to also appreciate the output at its correct value.

This report will be a background text in a graduation research project regarding uncertainty quantification in aerodynamic models applicable in conceptual design. It aims to answer two research questions:

1. Which (kind of) flow models, solution methods and combinations thereof (i.e. solvers) are suitable for aerodynamic analysis in a conceptual design process?
2. What assumptions, simplifications and limitations are associated to these flow models, solution methods and solvers?

In order to keep a broader scope, the order of answering these questions has been reversed. As such, the current report first of all aims to provide an overview of the various types of aerodynamic flow models and solution methods and present and discuss a number of solvers – implementations of (a) flow model(s) and (a) solution method(s) into a software program. This presentation and subsequent discussion is intended to shine a light on the ‘black boxes’ some of the solvers are and provide a concise, yet complete and well-supported, overview of the underlying methods and mechanisms relied upon by a certain piece of code. The second objective is to establish what (types of) models are relevant during conceptual design. Due to time limitations, literature on the topic of uncertainty quantification – also relevant for the graduation research project – will be reviewed as part of the main thesis work, building on e.g. [Roelofs and Vos \(2018\)](#).

The remainder of the report is structured as follows. Chapter [2](#) presents a review of the various classes of aerodynamic flow models. Chapter [3](#) treats methods used to solve these flow equations. Chapter [4](#), then, takes a more detailed look at various implementations of these solutions methods. A discussion concerning the applicability of various flow models, solution methods and aerodynamic solvers to aircraft conceptual design is presented in Chapter [5](#). In Chapter [6](#), conclusions are drawn, with a discussion following in Chapter [7](#). Based on this, Chapter [8](#), provides an outlook for the aforementioned graduation research project for which this literature study serves as a basis.

2

Overview of flow models

This chapter presents an overview of different aerodynamic flow models. In general, flows are governed by three basic principles: the conservation of mass, momentum (an application of Newton's Second Law, $F = m \cdot a$) and energy. The way these laws of conservation are translated into equations – a continuity equation, a momentum equation and an energy equation – however differs.

Figure 2.1 presents an overview of the models that will be treated in this chapter. The graphic serves as a guideline and is structured as follows. Moving down the vertical axis, the number of assumptions increases. This simplifies the flow model and reduces computational cost. Following the horizontal axis to the right, the extent to which a flow model is driven by empirical models increases. This too decreases computational cost.

At the top of the figure, various forms of the Navier-Stokes can be found, that differ by the extent to which they resolve or model turbulence. Section 2.1 goes into further detail. Apart from the time-dependent Navier-Stokes equations, that section pays most attention to their Reynolds-averaged counterparts, which are – of the Navier-Stokes equations – the flow model most widely used in airplane aerodynamics (Gerritsma, 2002; Elham, 2013). The Navier-Stokes equations are regarded as the highest fidelity flow models in existence, classified level L3 (Gu et al., 2018; Ciampa et al., 2013; Jungo et al., 2018).

Moving down, one can either keep left and follow the inviscid flow track, or move right towards the viscous thin-layer Navier-Stokes (TLNS) or boundary layer (BL) equations. As is further explained in Sections 2.1.5 and 2.2, respectively, these introduce additional assumptions to make viscous simulation available at relatively low cost. The boundary layer equations are often matched to an inviscid model using viscous-inviscid interaction methods (also discussed in Section 2.2) to yield a solution that holds inside as well as outside of the boundary layer. Although these flow models are not classified in terms of fidelity level in any of the aforementioned publications, the current author feels they are best positioned between levels L3 (the “most detailed representation of the physics phenomena”) and L2 (a “more detailed representation of the physics phenomena”) (Jungo et al., 2018, p. 617) – given their additional assumptions compared to L3-models. As such, there are classified level L2.5.

Found in level L2 are the Euler equations, treated in Section 2.3, derived from the Navier-Stokes equations but completely neglecting viscous effects. Assuming irrotational flow yields the full potential equation (discussed in Section 2.4), which can be further simplified by either linearising it to arrive at the linearised potential or Prandtl-Glauert equation (in Section 2.5), or assuming incompressible flow. This last assumption results in Laplace's equation, which is treated in greater detail in Section 2.6. The full potential equation, as well as its derivatives, are classified as level L1-models, indicating they are “physics based analysis tools, based on a *simplified* representation of the physics phenomena” (Jungo et al., 2018, p. 617, emphasis in original). L0, then, is formed by the purely empirical tools, on which some words are spent in Section 2.7.

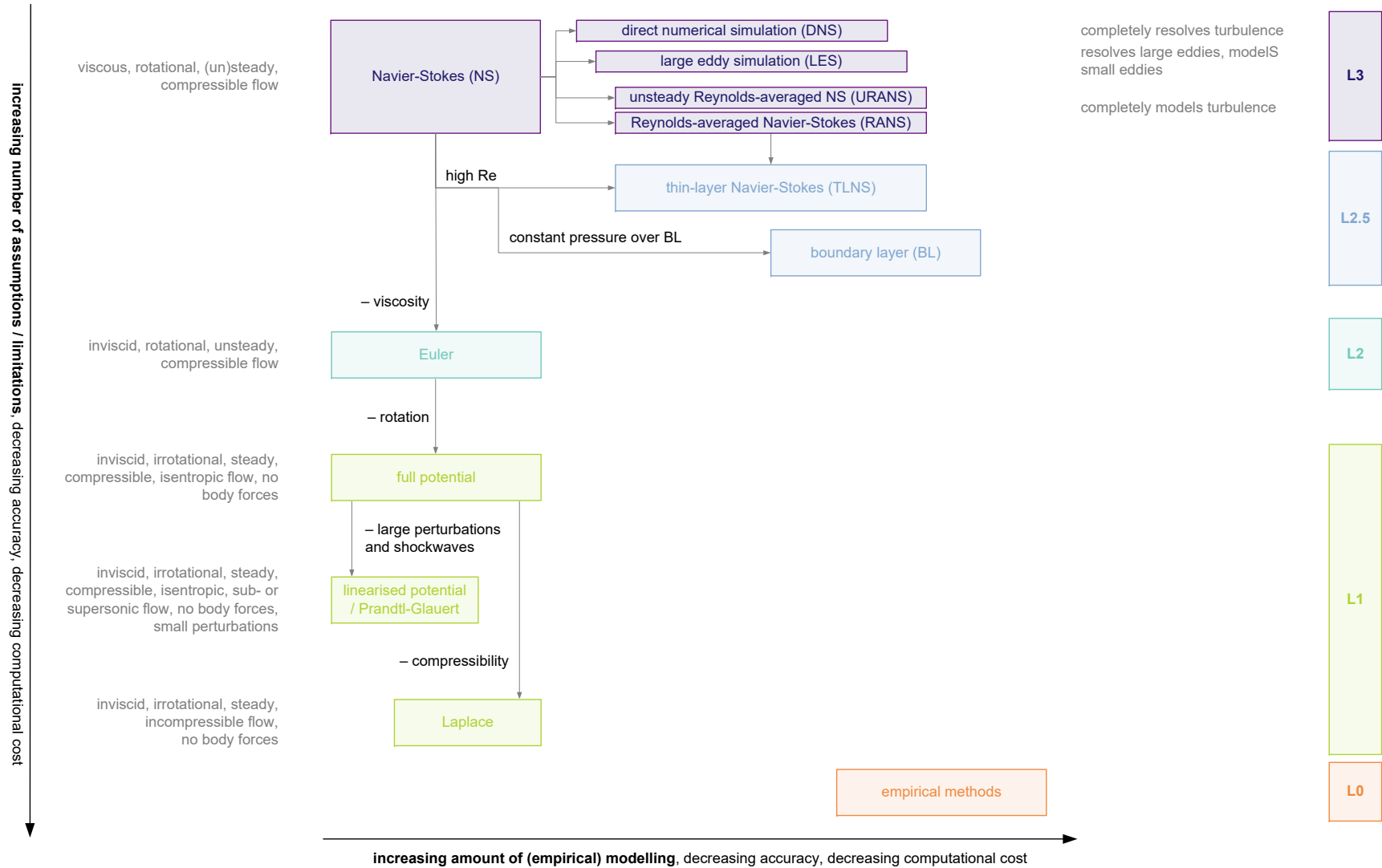


Figure 2.1: Hierarchical overview of aerodynamic flow models, based on Jameson (2004, p. 11), Mariens (2012), Schmidt (2013), Gu et al. (2018), Cummings et al. (2015, p. 139), Gerritsma (2002) in Elham (2013, p. 77), Anderson (2002) and Spalart (2000). Larger-size versions available through bram.peerlings.me/en/literature-study/ using password "AE4020-2018"

2.1. Navier-Stokes equations

The Navier-Stokes equations represent the most accurate flow model that exists and describe viscous, rotational and compressible flow. The Navier-Stokes equations themselves describe the conservation of momentum – only one of the governing laws mentioned in the introduction of this chapter – and require additional expressions for the conservation of mass and energy (the latter only in case of compressible flow).

The Navier-Stokes equations are a set of non-linear partial differential equations. Multiple representations exist, with [Anderson et al. \(2009, Ch. 2\)](#) adhering to the form shown in Equation (2.1). (Other forms are shown in e.g. [Peyret and Viviand \(1975\)](#).) These equations hold for a fixed-mass particle and are shown in the *conservation form*. This means that they are based on the forces and accelerations acting on a fixed point in the flow (Eulerian approach), rather than these acting on a particle moving with the flow (Lagrangian approach) ([Peyret and Viviand, 1975](#)).

$$\frac{\partial(\rho u)}{\partial t} + \nabla \cdot (\rho u \mathbf{V}) = -\frac{\partial p}{\partial x} + \frac{\partial \tau_{xx}}{\partial x} + \frac{\partial \tau_{yx}}{\partial y} + \frac{\partial \tau_{zx}}{\partial z} + \rho f_x \quad (2.1a)$$

$$\frac{\partial(\rho v)}{\partial t} + \nabla \cdot (\rho v \mathbf{V}) = -\frac{\partial p}{\partial y} + \frac{\partial \tau_{xy}}{\partial x} + \frac{\partial \tau_{yy}}{\partial y} + \frac{\partial \tau_{zy}}{\partial z} + \rho f_y \quad (2.1b)$$

$$\frac{\partial(\rho w)}{\partial t} + \nabla \cdot (\rho w \mathbf{V}) = -\frac{\partial p}{\partial z} + \frac{\partial \tau_{xz}}{\partial x} + \frac{\partial \tau_{yz}}{\partial y} + \frac{\partial \tau_{zz}}{\partial z} + \rho f_z \quad (2.1c)$$

The right-hand sides of these equations – one in each direction of a Cartesian coordinate system – represent the sum of forces. The first term is the pressure force in a particular direction, the next three terms are shear forces (the viscous terms) and the fifth and final term represents the body force. The left-hand sides of Equation (2.1) represent force and acceleration. The shear stress components are shown in Equation (2.2).

$$\tau_{xx} = \lambda \nabla \cdot \mathbf{V} + 2\mu \frac{\partial u}{\partial x} \quad (2.2a)$$

$$\tau_{yy} = \lambda \nabla \cdot \mathbf{V} + 2\mu \frac{\partial v}{\partial y} \quad (2.2b)$$

$$\tau_{zz} = \lambda \nabla \cdot \mathbf{V} + 2\mu \frac{\partial w}{\partial z} \quad (2.2c)$$

$$\tau_{xy} = \tau_{yx} = \mu \left(\frac{\partial v}{\partial x} + \frac{\partial u}{\partial y} \right) \quad (2.2d)$$

$$\tau_{xz} = \tau_{zx} = \mu \left(\frac{\partial u}{\partial z} + \frac{\partial w}{\partial x} \right) \quad (2.2e)$$

$$\tau_{yz} = \tau_{zy} = \mu \left(\frac{\partial w}{\partial y} + \frac{\partial v}{\partial z} \right) \quad (2.2f)$$

When these are substituted in Equation (2.1), the complete Navier-Stokes equations for Newtonian fluids are obtained, as shown in Equation (2.3).

$$\begin{aligned} \frac{\partial(\rho u)}{\partial t} + \frac{\partial(\rho u^2)}{\partial x} + \frac{\partial(\rho uv)}{\partial y} + \frac{\partial(\rho uw)}{\partial z} = \\ -\frac{\partial p}{\partial x} + \frac{\partial}{\partial x} \left(\lambda \nabla \cdot \mathbf{V} + 2\mu \frac{\partial u}{\partial x} \right) + \frac{\partial}{\partial y} \left[\mu \left(\frac{\partial v}{\partial x} + \frac{\partial u}{\partial y} \right) \right] + \frac{\partial}{\partial z} \left[\mu \left(\frac{\partial w}{\partial y} + \frac{\partial v}{\partial z} \right) \right] + \rho f_x \end{aligned} \quad (2.3a)$$

$$\begin{aligned} \frac{\partial(\rho v)}{\partial t} + \frac{\partial(\rho uv)}{\partial x} + \frac{\partial(\rho v^2)}{\partial y} + \frac{\partial(\rho vw)}{\partial z} = & \\ - \frac{\partial p}{\partial y} + \frac{\partial}{\partial x} \left[\mu \left(\frac{\partial v}{\partial x} + \frac{\partial u}{\partial y} \right) \right] + \frac{\partial}{\partial y} \left(\lambda \nabla \cdot \mathbf{V} + 2\mu \frac{\partial v}{\partial y} \right) + \frac{\partial}{\partial z} \left[\mu \left(\frac{\partial w}{\partial y} + \frac{\partial v}{\partial z} \right) \right] + \rho f_y & \end{aligned} \quad (2.3b)$$

$$\begin{aligned} \frac{\partial(\rho w)}{\partial t} + \frac{\partial(\rho uw)}{\partial x} + \frac{\partial(\rho vw)}{\partial y} + \frac{\partial(\rho w^2)}{\partial z} = & \\ - \frac{\partial p}{\partial z} + \frac{\partial}{\partial x} \left[\mu \left(\frac{\partial u}{\partial z} + \frac{\partial w}{\partial x} \right) \right] + \frac{\partial}{\partial y} \left[\mu \left(\frac{\partial w}{\partial y} + \frac{\partial v}{\partial z} \right) \right] + \frac{\partial}{\partial z} \left(\lambda \nabla \cdot \mathbf{V} + 2\mu \frac{\partial w}{\partial z} \right) + \rho f_z & \end{aligned} \quad (2.3c)$$

In order to be able to solve the Navier-Stokes equations, it is necessary to include a form of the continuity equation, expressing conservation of mass. An example is shown in Equation (2.4) (Anderson et al., 2009, Ch. 2):

$$\frac{\partial \rho}{\partial t} + \nabla \cdot (\rho \mathbf{V}) = 0 \quad (2.4)$$

Again, normalised with respect to the volume of the particle, this equation states that the sum of the time rate of change of mass in a control volume and the mass flux through the boundary of that volume is equal to 0.

If the density is not constant, another equation is required to solve the set: the energy equation. For a fixed point in the flow, it is expressed as shown in Equation (2.5) (Anderson et al., 2009, Ch. 2).

$$\begin{aligned} \frac{\partial}{\partial t} \left[\rho \left(e + \frac{V^2}{2} \right) \right] + \nabla \cdot \left[\rho \left(e + \frac{V^2}{2} \mathbf{V} \right) \right] = \rho \dot{q} & \\ + \frac{\partial}{\partial x} \left(k \frac{\partial T}{\partial x} \right) + \frac{\partial}{\partial y} \left(k \frac{\partial T}{\partial y} \right) + \frac{\partial}{\partial z} \left(k \frac{\partial T}{\partial z} \right) & \\ - \frac{\partial(u p)}{\partial x} - \frac{\partial(v p)}{\partial y} - \frac{\partial(w p)}{\partial z} & \\ + \frac{\partial(u \tau_{xx})}{\partial x} + \frac{\partial(u \tau_{yx})}{\partial y} + \frac{\partial(u \tau_{zx})}{\partial z} & \\ + \frac{\partial(v \tau_{xy})}{\partial x} + \frac{\partial(v \tau_{yy})}{\partial y} + \frac{\partial(v \tau_{zy})}{\partial z} & \\ + \frac{\partial(w \tau_{xz})}{\partial x} + \frac{\partial(w \tau_{yz})}{\partial y} + \frac{\partial(w \tau_{zz})}{\partial z} & \\ + \rho \mathbf{f} \cdot \mathbf{V} & \end{aligned} \quad (2.5)$$

The left-hand side expresses the (temporal and spatial) rate of change of energy of the element, consisting of both internal and kinetic energy. On the right-hand side, $\rho \dot{q}$ is the rate of volumetric heating (given by \dot{q}) of the element (hence the multiplication with ρ). The second line is the thermal conduction through all six faces of the element (in which k is the thermal conductivity). Next, on the third line, the rate of work done by pressure forces acting on the element is shown. The following three lines (with the τ -terms) represent the work done on the element by stress forces acting on the surface of the element. The last line shows the body forces. The derivatives of τ liken the terms in Equation (2.1), but are multiplied with the velocity components in the three dimensions (as work is force multiplied with displacement, and the time derivative of work therefore is change in force multiplied with change in displacement, i.e., speed). Furthermore, the shear stresses shown in Equation (2.2) can be used to further specify Equation (2.5).

The Navier-Stokes equations can also be written in vector form. In that case, the continuity, momentum and energy equations are combined (from top to bottom) as shown in Equation (2.6) and Equation (2.7) (Anderson et al., 2009, Ch. 2). These are still shown in conservation form.

$$\frac{\partial \mathbf{U}}{\partial t} + \frac{\partial \mathbf{F}}{\partial x} + \frac{\partial \mathbf{G}}{\partial y} + \frac{\partial \mathbf{H}}{\partial z} = \mathbf{J} \quad (2.6)$$

$$\begin{aligned} \mathbf{U} &= \begin{pmatrix} \rho \\ \rho u \\ \rho v \\ \rho w \\ \rho \left(e + \frac{v^2}{2} \right) \end{pmatrix} \\ \mathbf{F} &= \begin{pmatrix} \rho u \\ \rho u^2 + p - \tau_{xx} \\ \rho uv - \tau_{xy} \\ \rho uw - \tau_{xz} \\ \rho \left(e + \frac{v^2}{2} \right) u + up - k \frac{\partial T}{\partial x} - u\tau_{xx} - v\tau_{xy} - w\tau_{xz} \end{pmatrix} \\ \mathbf{G} &= \begin{pmatrix} \rho v \\ \rho uv - \tau_{yx} \\ \rho v^2 + p - \tau_{yy} \\ \rho vw - \tau_{yz} \\ \rho \left(e + \frac{v^2}{2} \right) v + vp - k \frac{\partial T}{\partial y} - u\tau_{yx} - v\tau_{yy} - w\tau_{yz} \end{pmatrix} \\ \mathbf{H} &= \begin{pmatrix} \rho w \\ \rho uw - \tau_{zx} \\ \rho vw - \tau_{zy} \\ \rho w^2 + p - \tau_{zz} \\ \rho \left(e + \frac{v^2}{2} \right) w + wp - k \frac{\partial T}{\partial z} - u\tau_{zx} - v\tau_{zy} - w\tau_{zz} \end{pmatrix} \\ \mathbf{J} &= \begin{pmatrix} 0 \\ \rho f_x \\ \rho f_y \\ \rho f_z \\ \rho (uf_x + vf_y + wf_z) + \rho \dot{q} \end{pmatrix} \end{aligned} \quad (2.7)$$

Taken together, the five equations presented above (or their combination in vector form) can be used to find flow properties (such as pressure and velocity) in viscous, rotational, unsteady, compressible flows. However, only for a few particular types of flow – in which a various terms are equal to 0 – can *exact* solutions be found. For other problems, numerical (and non-exact) solution methods have to be applied¹. These are the four varieties shown in Figure 2.1: direct numerical simulation (DNS), large eddy simulation (LES), the unsteady Reynolds-averaged Navier-Stokes (URANS) equations and the steady Reynolds-averaged Navier-Stokes (RANS) equations. The upcoming sections treat these in greater detail.

¹Although these are indeed solution methods and therefore might seem to belong in the chapter discussing those (Chapter 3), it was decided to treat these here. Contrary to the solution methods discussed in the aforementioned chapter, the solution methods discussed here truly change the *problem*, and not only the (numerical) approach with which to solve it.

2.1.1. Direct numerical simulation (DNS)

DNS is the most accurate form (or solution method) for the Navier-Stokes equations. Although it is not exact due to discretisation steps and possible numerical errors, the method does not average or neglect any terms, or approximate these using (semi-)empirical relations (Ferziger and Perić, 2002, Sec. 9.2). All turbulence is resolved. As such, it will not be surprising that the computational cost of DNS is very high (Argyropoulos and Markatos, 2015) – so high that DNS is expected to only be ready for commercial application after 2080 (Spalart, 2000)². One reason for this is that the computational domain has to be large enough to capture all the largest turbulent flow structures, yet fine enough to also resolve the smallest ones.

2.1.2. Large eddy simulation (LES)

LES counters the problem of excessive computational cost by focusing on resolving only the large eddies (determined by the size of a spatial filter), which are more energetic and therefore more important for the transfer of mass, energy and momentum (Ferziger and Perić, 2002, Sec. 9.3). Smaller turbulence scales are modelled by a (semi-)empirical turbulence model (discussed in greater detail in Section 2.1.6). This is warranted as the large eddies are most influenced by the geometry of the problem, whereas smaller scale turbulent structures are more universal and can therefore be described using *subgrid scale models* (CFD Online, 2013; Blazek, 2007; Speziale, 1998), without sacrificing too much accuracy. The details thereof are however beyond the scope of the current text. Ultimately, these simplifications reduce the amount of required grid points, realising the reduction in computational cost (Blazek, 2007). Still, Spalart (2000) expects readiness only after 2045².

Related to LES are detached eddy simulation (DES) and delayed detached eddy simulation (DDES), but these variants are deemed too far out of scope to be treated in this text. Further information on these can be found in e.g. Cummings et al. (2015, Sec. 8.10) and (Spalart, 2000).

2.1.3. Unsteady Reynolds-averaged Navier-Stokes equations (URANS)

Also somewhat related to LES are the unsteady Reynolds-averaged Navier-Stokes equations, sometimes also known as transient Reynolds-averaged Navier-Stokes equation (TRANS). The method was developed from the desire to have a tool computationally less costly than LES, but one still able to capture transient flow phenomena – which ‘ordinary’ (steady) RANS cannot do (Salim et al., 2011) as turbulence models and closure relations are based on steady flows. Although a clear cut definition could not be found in literature, the primary difference between steady and unsteady RANS in terms of (mathematical or numerical) implementation is the fact that steady RANS averages over the entire time interval, whereas URANS does so over the interval of a single time step (Nanda, 2016). This yields a so-called ensemble average³ (Nanda, 2016; Salim et al., 2011; Léonard et al., 2015). Whereas LES uses a spatial filter to determine which turbulence is resolved and which is modelled, one might say that URANS effectively uses a time-based filter.

Results obtained with URANS are varied. Some authors note it as an improvement (Iaccarino et al. (2003) in case of modelling periodic vortex shedding, for example), whereas other flow phenomena (as documented by e.g. Salim et al. (2011) and Léonard et al. (2015)) still require LES to be properly simulated. Salim et al. (2011, p. 5) limit the applicability of URANS to “non-stationary flows such as periodic and quasi-periodic flows involving deterministic structures”. Spalart (2000) mentions good results with URANS for bluff bodies and similar flows.

²Assuming a 5-fold increase in computer power every 5 years.

³An ensemble average is what one would get if one would average all possible results of a simulation at a particular point in space. This is different from a time average, where the quantities at a particular point *in one simulation* are averaged.

2.1.4. Reynolds-averaged Navier-Stokes equations (RANS)

Even though LES and URANS all have brought down the computational cost of performing Navier-Stokes simulations, these are still (prohibitively) high, especially at high Reynolds numbers (Blazek, 2007) and in case of complex geometries (Ferziger and Perić, 2002). Elham (2013), citing Gerritsma (2002), notes that the full Navier-Stokes equations and their solution methods are *fundamental*. Reynolds-averaged Navier-Stokes (RANS) equations, on the other hand, further simplify the problem and make the solution method available for practical purposes. In other words: *airplane aerodynamics* (Elham, 2013; Gerritsma, 2002).

Mathematically, the (steady) RANS equations can be derived by time-averaging⁴ the flow variables into mean and time-dependent⁵ components (Blazek, 2007; Elham, 2013; Leschziner, 2010). This is the so-called Reynolds decomposition, which splits up the problem into two parts. First is the averaged part, of largest interest to engineers, which is numerically solved (Leschziner, 2010). Second is the fluctuating part (i.e., turbulence), which becomes zero when time-averaged (Cummings et al., 2015). This is replaced by a semi-empirical turbulence model that closes the RANS equations by providing a value for the turbulent viscosity and describes the Reynolds stresses (a stress term added as a result of Reynolds-averaging the Navier-Stokes equations) and the turbulent heat flux (Blazek, 2007) – features previously described by the fluctuating parts of the NS equations.

The derivation of the three-dimensional RANS equations is quite lengthy and, as such, is not repeated here. Cummings et al. (2015, Sec. 8.8) treat it for incompressible flow; Vos and Farokhi (2015, Sec. 2.6) and Pletcher et al. (2012, Sec. 5.2) discuss the RANS-equations for compressible flow. Because both velocity and density are Reynolds-decomposed in this case (and the two are co-dependent), a mass-weighted averaging is used to keep the equations from getting overly complicated (Blazek, 2007; Wilcox, 2006). Details on that process can be found in the aforementioned works.

2.1.5. Thin-layer Navier-Stokes equations (TLNS)

Somewhat intermediate to the viscous Navier-Stokes equations in all its forms and the inviscid Euler equations (treated in Section 2.3) are the thin-layer Navier-Stokes (TLNS) equations. These were developed using the same philosophy as the boundary layer equations (further discussed in Section 2.2), in the sense that viscous effects parallel to the flow are neglected. This holds as long as the Reynolds number is sufficiently high ($Re \geq 10^4$). As the pressure across the boundary layer (perpendicular to the flow) is allowed to vary (something that is not the case when using boundary layer theory) (Baldwin and Lomax, 1978), the TLNS equations can describe separated flow – as long as the separation is not too massive (Pulliam, 1986). This is the major advantage compared to the boundary layer equations and formed the reason for the development of the thin-layer approximation in the 1970s. This approximation is formally defined (quoted from Pulliam (1986, p. 12) and Mouch and Lan (1993, p. 3)) as requiring that

- all body surfaces be mapped onto coordinate surfaces;
- grid spacing is clustered to the body surfaces such that sufficient resolution for a particular Reynolds number is obtained; and
- all the viscous derivatives in the ξ direction [parallel to the surface] are neglected, while the terms in η direction [perpendicular to the surface] are retained.

Sources provide different (and conflicting) information regarding the time-dependency of TLNS. Cummings et al. (2015) on one hand (p. 139) indicate the TLNS equations follow from the RANS equations, as does Gerritsma (2002), cited in Elham (2013, p. 77). On the other hand, when deriving the TLNS equations (Cummings et al., 2015, p. 151) the time-dependent NS equations are used as starting point – and not the Reynolds-averaged ones. This seems to correspond with Simpson (1989), discussing *unsteady* TLNS solutions and also deriving the TLNS equations from the time-dependent NS equations,

⁴As the RANS equations are time-averaged, the 'full' Navier-Stokes equations are sometimes also referred to as the *time-dependent* Navier-Stokes equations.

⁵The name *Reynolds-averaged Navier-Stokes* does not mean the Reynolds number is averaged. The number and these equations are simply named after the same person.

just as Pulliam (1986). Baldwin and Lomax (1978, p. 3), however, explicitly state that “[t]he equations to be solved in a thin-layer approximation are based on the time-averaged or subgrid scale models of the Navier-Stokes equations”, pointing to RANS. The fact that TLNS-solver ARC2D (the topic of Section 4.1.4) uses turbulence models does the same.

Further disagreement seems to exist on the necessity (or applicability) of a viscous-inviscid interaction method (more thoroughly discussed in Section 2.2) in combination with TLNS. Pulliam and Steger (1978, p. 2) state “[u]nlike boundary-layer theory the thin layer model avoids the difficulty of matching an inviscid layer with a viscous layer”, whereas Mouch and Lan (1993) report on doing exactly that (matching ARC2D, discussed in Section 4.1.4, with panel code PMARC).

2.1.6. Turbulence modelling

As discussed in Section 2.1.4, RANS-simulations do not resolve turbulence, but model it. This is done by any of a wide variety of turbulence models (Argyropoulos and Markatos, 2015) based on empirical data (Cummings et al., 2015). The use of a turbulence model is to provide a value for the aforementioned Reynolds stresses. This can be done directly – using Reynolds stress models (RSM) – or indirectly, using the Boussinesq assumption (Wilcox, 2006). This assumption, stating that the Reynolds stress scales with the average strain rate, can be used to relate the Reynolds stresses to the mean flow parameters (Vos and Farokhi, 2015; Cummings et al., 2015). This means that “the effect of turbulence can be represented as an increased viscosity, [so that] the total viscosity is divided into a laminar [...] and a turbulent [...] component” (Palacios et al., 2013, p. 15). In other words: the viscosity μ (part of the stress components for the Navier-Stokes equation, shown in isolation in Equation (2.2) and in the x -, y - and z -equations in Equation (2.3)) is split up into a dynamic one, μ_{dyn} , and a turbulent one, μ_{turb} , of which the latter is obtained from the turbulence model (Palacios et al., 2013).

Blazek (2007, p. 56) describes the direct and indirect methods as second- and first-order closure models, respectively. The Reynolds-stress transport (RST) model and the algebraic Reynolds-stress (ARS) model are examples of the more flexible – but also more complex – second-order methods. Although better able to describe complex turbulent flow phenomena, these second-order methods also have some numerical problems.

As such, first-order methods (also known as *linear eddy-viscosity models* or LEVMs) that adhere to the Boussinesq assumption, are therefore more widely used in practice (Leschziner, 2010). Within this group of models, there are zero-, one- and multiple-equation models that, as their names suggest, use zero, one or multiple transport equations. Zero-equation models are completely empirical and cannot describe history effects, leading to problems in case of separated flows. The one- and multiple-equation models do take history effects into account. Well-known examples are the Spalart-Allmaras model (one-equation, Spalart and Allmaras (1992)), the $k - \epsilon$ -model (two-equation by Launder and Spalding (1974), k for turbulent kinetic energy and ϵ for the dissipation rate thereof) and the $k - \omega$ -model (two-equation by Wilcox (1988), k again turbulent kinetic energy and ω the dissipation rate per unit energy). Further details of these methods will be discussed if and when relevant and are treated in the cited works. Besides, Wilcox (2006) and Blazek (2007) can be used as references.

The turbulence models discussed in the previous paragraph are mostly applicable to higher Reynolds number flows. In predicting flow properties near the wall, a region where viscous effects dominate the flow (i.e., where the Reynolds number is lower), modified turbulence models have been proposed. Argyropoulos and Markatos (2015) review some of these. As they are deemed of little interest for the applications considered here (transport aircraft), these models are not discussed further.

2.2. Boundary layer equations

Boundary layer equations (just like the thin-layer Navier-Stokes equations) are based on the notion that at large enough Reynolds numbers, the effects of viscosity are only limited to a small region of the flow: the boundary layer. The boundary layer and some of its properties are shown in Figure 2.2:

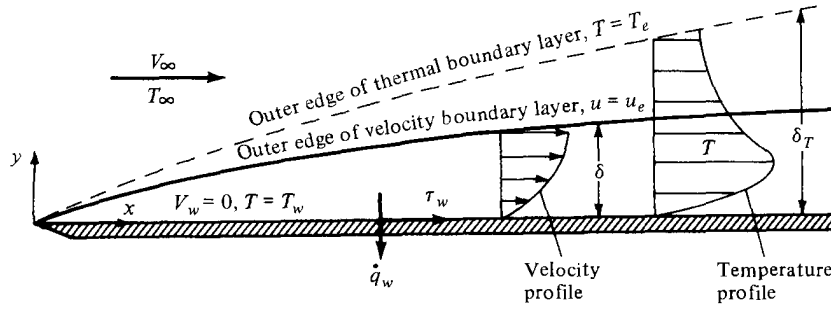


Figure 2.2: Boundary layer properties (Anderson, 2001, p. 790)

Starting from the Navier-Stokes equations, the boundary layer equations are found by dropping terms of smaller orders of magnitude (and therefore of little importance to the final result) in order to create a set of equations that is manageable. A key simplification is neglecting the viscous diffusion terms that are seen parallel to the flow, as their contribution to the viscous effects is so low. Various types and forms of boundary layer equations exist, for example differing between 2D or 3D, steady or unsteady flows, and with or without the assumption of incompressible flow (Cummings et al., 2015, Sec. 3.13). A primary assumption of all boundary layer models is that the pressure is constant normal to the wall, throughout the thickness of the boundary layer. This assumption, however, makes boundary layer equations unsuited for computation of separated flows (Cummings et al., 2015; Hassan and Muntz, 2000).

Just as most forms of the Navier-Stokes equations, boundary layers need so-called *closure relations* to be solved. These are empirical relations and can be compared conceptually to the turbulence models treated in Section 2.1.6.

The coupling of the viscous boundary layer and inviscid flow model (often potential flow) is achieved using a viscous-inviscid interaction (VII) method. This is an iterative process, as the location of the boundary layer edge is initially unknown, as is the flow velocity at that edge. Of course, the flow speed of the viscous and inviscid models have to be equal at that edge, in order to prevent shear stresses. Further details of these interaction methods are provided if and where relevant. A more general description, including a historical perspective, can be found in Lock and Williams (1987).

2.3. Euler equations

Whereas the NS equations and boundary layer equations model viscous effects, the Euler equations assume inviscid flow. This means that Equations (2.1) and (2.3) are simplified to Equation (2.8), shown below.

$$\frac{\partial (\rho u)}{\partial t} + \nabla \cdot (\rho u \mathbf{V}) = -\frac{\partial p}{\partial x} + \rho f_x \quad (2.8a)$$

$$\frac{\partial (\rho v)}{\partial t} + \nabla \cdot (\rho v \mathbf{V}) = -\frac{\partial p}{\partial y} + \rho f_y \quad (2.8b)$$

$$\frac{\partial (\rho w)}{\partial t} + \nabla \cdot (\rho w \mathbf{V}) = -\frac{\partial p}{\partial z} + \rho f_z \quad (2.8c)$$

As the derivation of the continuity equation does not depend on viscous effects, Equation (2.4) remains unchanged. The energy equation, previously shown in Equation (2.5), does change. As such, an inviscid formula can be derived, as done in Equation (2.9). Note that the terms describing thermal conductivity also disappear, because of the definition of inviscid flow.

$$\begin{aligned} \frac{\partial}{\partial t} \left[\rho \left(e + \frac{V^2}{2} \right) \right] + \nabla \cdot \left[\rho \left(e + \frac{V^2}{2} \right) \mathbf{V} \right] = p\dot{q} \\ - \frac{\partial (up)}{\partial x} - \frac{\partial (vp)}{\partial y} - \frac{\partial (wp)}{\partial z} \\ + \rho \mathbf{f} \cdot \mathbf{V} \end{aligned} \quad (2.9)$$

Although neglecting viscous effects might seem to limit applicability of the Euler equations substantially, research has shown that outside the boundary layer, inviscid flow models are a good approximation (Jameson, 2004).

2.4. Full potential equation

A further simplification to modelling flow is to assume the flow is irrotational – something that generally does not hold for the part of the flow domain downstream of a shock wave (Freestone, 2004). That means that fluid particles are modelled as moving along a streamline without rotating or deforming. In an irrotational flow, the vorticity ξ – equal to $\nabla \times \mathbf{V}$ – is 0 (Anderson, 2001, pp. 145, 158). Combining this with the notion that the curl of the gradient of a scalar function is zero yields Equation (2.10):

$$\mathbf{V} = \nabla \phi \quad (2.10)$$

ϕ is the velocity potential, here a function of x , y and z . Writing this in scalar form yields Equation (2.11):

$$u = \frac{\partial \phi}{\partial x} \quad (2.11a)$$

$$v = \frac{\partial \phi}{\partial y} \quad (2.11b)$$

$$w = \frac{\partial \phi}{\partial z} \quad (2.11c)$$

Assuming steady flow (meaning that flow properties, such as pressure and density, only depend on their location in the flow), Equation (2.11) can then be substituted in the continuity equation (Equation (2.4), with $\frac{\partial \rho}{\partial t} = 0$). Combining this with the momentum equation and assuming isentropic flow and zero body forces yields the full potential equation (also known as non-linear potential equation) shown in Equation (2.12) (Anderson, 2002, Ch. 8):

$$\begin{aligned} \left[1 - \frac{1}{a^2} \left(\frac{\partial \phi}{\partial x} \right)^2 \right] \frac{\partial^2 \phi}{\partial x^2} + \left[1 - \frac{1}{a^2} \left(\frac{\partial \phi}{\partial y} \right)^2 \right] \frac{\partial^2 \phi}{\partial y^2} + \left[1 - \frac{1}{a^2} \left(\frac{\partial \phi}{\partial z} \right)^2 \right] \frac{\partial^2 \phi}{\partial z^2} \\ - \frac{2}{a^2} \left(\frac{\partial \phi}{\partial x} \right) \left(\frac{\partial \phi}{\partial y} \right) \frac{\partial^2 \phi}{\partial x \partial y} - \frac{2}{a^2} \left(\frac{\partial \phi}{\partial x} \right) \left(\frac{\partial \phi}{\partial z} \right) \frac{\partial^2 \phi}{\partial x \partial z} - \frac{2}{a^2} \left(\frac{\partial \phi}{\partial y} \right) \left(\frac{\partial \phi}{\partial z} \right) \frac{\partial^2 \phi}{\partial y \partial z} = 0 \end{aligned} \quad (2.12)$$

To remove the speed of sound a from the equation, the energy equation is used. Given the assumptions of no body forces and isentropic flow (i.e., adiabatic and reversible), it can be shown that the total enthalpy along a streamline is constant (Anderson, 2002, Ch. 6). For a perfect gas, this allows for expressing a fully in terms of constants and the velocity potential, as shown in Equation (2.13):

$$a^2 = a_\infty^2 - \frac{\gamma - 1}{2} \left[\left(\frac{\partial \phi}{\partial x} \right)^2 + \left(\frac{\partial \phi}{\partial y} \right)^2 + \left(\frac{\partial \phi}{\partial z} \right)^2 \right] \quad (2.13)$$

Note that whereas previous sections dealt with sets of multiple equations, the full potential equation is a single equation – combining the continuity, momentum and energy equations.

2.5. Linearised potential equation

Even though the full potential equation is a lot simpler than previous flow equations, the fact that it is a non-linear partial differential equation makes it difficult to solve. Linearising the full potential equation solves that problem (Anderson, 2002, Ch. 9). This is done by decomposing the velocity in an unperturbed and a perturbed component.

Given a freestream velocity in x -direction, $V_x = V_\infty + u'$, $V_y = v'$ and $V_z = w'$, with u' , v' and w' denoting the perturbation velocities. These can be used to derive a perturbation velocity potential ϕ so that $(x, y, z) = V_\infty x + \phi(x, y, z)$. Substitution of this expression and multiplication by a^2 transforms the potential equation shown in Equation (2.12) into Equation (2.14). Note that time-derivatives of ϕ are expressed as perturbation velocities.

$$\begin{aligned} & [a^2 - (V_\infty + u')^2] \frac{\partial u'}{\partial x} + [a^2 - v'^2] \frac{\partial v'}{\partial y} + [a^2 - w'^2] \frac{\partial w'}{\partial z} \\ & - 2(V_\infty + u')v' \frac{\partial u'}{\partial y} - 2(V_\infty + u')w' \frac{\partial u'}{\partial z} - 2v'w' \frac{\partial v'}{\partial z} = 0 \end{aligned} \quad (2.14)$$

Similarly, Equation (2.13) can be rewritten as Equation (2.15):

$$a^2 = a_\infty^2 - \frac{\gamma - 1}{2} [2u'V_\infty + u'^2 + v'^2 + w'^2] \quad (2.15)$$

Substitution of Equation (2.15) into Equation (2.14) then yields Equation (2.16):

$$\begin{aligned} (1 - M_\infty^2) \frac{\partial u'}{\partial x} + \frac{\partial v'}{\partial y} + \frac{\partial w'}{\partial z} = & \\ & M_\infty^2 \left[(\gamma + 1) \frac{u'}{V_\infty} + \left(\frac{\gamma + 1}{2} \right) \frac{u'^2}{V_\infty^2} + \left(\frac{\gamma - 1}{2} \right) \frac{v'^2 + w'^2}{V_\infty^2} \right] \frac{\partial u'}{\partial x} \\ & + M_\infty^2 \left[(\gamma - 1) \frac{u'}{V_\infty} + \left(\frac{\gamma + 1}{2} \right) \frac{v'^2}{V_\infty^2} + \left(\frac{\gamma - 1}{2} \right) \frac{w'^2 + u'^2}{V_\infty^2} \right] \frac{\partial v'}{\partial y} \\ & + M_\infty^2 \left[(\gamma - 1) \frac{u'}{V_\infty} + \left(\frac{\gamma + 1}{2} \right) \frac{w'^2}{V_\infty^2} + \left(\frac{\gamma - 1}{2} \right) \frac{u'^2 + v'^2}{V_\infty^2} \right] \frac{\partial w'}{\partial z} \\ & + M_\infty^2 \left[\frac{v'}{V_\infty} \left(1 + \frac{u'}{V_\infty} \right) \left(\frac{\partial u'}{\partial y} + \frac{\partial v'}{\partial x} \right) + \frac{w'}{V_\infty} \left(1 + \frac{u'}{V_\infty} \right) \left(\frac{\partial u'}{\partial z} + \frac{\partial w'}{\partial x} \right) \right. \\ & \quad \left. + \frac{u'w'}{V_\infty^2} \left(\frac{\partial w'}{\partial y} + \frac{\partial v'}{\partial z} \right) \right] \end{aligned} \quad (2.16)$$

In order to linearise Equation (2.16), only small perturbations are considered. This yields that for $0 \leq M_\infty \leq 0.8$ and $M_\infty \geq 1.2$, the second line of Equation (2.16) is small compared to the first term on the left hand side and can thus be ignored. Similarly, for $M_\infty \leq 5$, the third and fourth line are small compared to $\frac{\partial v'}{\partial y}$ and $\frac{\partial w'}{\partial z}$, respectively, so that the former terms can also be ignored. Lastly, the term on the fifth and sixth line is approximately zero. Therefore, the linearised potential equation reduces to Equation (2.17), shown below:

$$(1 - M_\infty^2) \frac{\partial u'}{\partial x} + \frac{\partial v'}{\partial y} + \frac{\partial w'}{\partial z} = (1 - M_\infty^2) \frac{\partial^2 \phi}{\partial x^2} + \frac{\partial^2 \phi}{\partial y^2} + \frac{\partial^2 \phi}{\partial z^2} = 0 \quad (2.17)$$

As shown before, Equation (2.17) is limited to small perturbations and can only be used outside transonic and hypersonic flow regions. It is also known as the Prandtl-Glauert equation (Cummings et al., 2015).

2.6. Laplace's equation

The full potential equation (discussed in Section 2.4) was linearised using perturbation velocities in Section 2.5. However, if incompressible flow is assumed (valid for $M_\infty < 0.3$), the full potential equation reduces to a partial differential equation that is linear in and of itself: Laplace's equation.

The full potential equation was derived based on the continuity equation shown in Equation (2.4). For steady flow, $\frac{\partial \rho}{\partial t} = 0$ and for compressible flow, ρ is constant such that $\nabla \cdot (\rho \mathbf{V}) = \nabla \cdot \mathbf{V}$, which yields Equation (2.18) (Anderson, 2001, Ch. 3):

$$\nabla \cdot \mathbf{V} = 0 \quad (2.18)$$

Given Equation (2.11), this can be rewritten as Equation (2.19), which is Laplace's equation:

$$\frac{\partial^2 \phi}{\partial x^2} + \frac{\partial^2 \phi}{\partial y^2} + \frac{\partial^2 \phi}{\partial z^2} = \nabla^2 \phi = 0 \quad (2.19)$$

The same result can be achieved from Equation (2.12) by realising that $a \rightarrow \infty$ for incompressible flow (Anderson, 2002, Ch. 8), causing the terms in square brackets to go to 1 and the terms on the second line to go to 0. Also, as $a \rightarrow \infty$, $M_\infty \rightarrow 0$, so that the term between brackets in Equation (2.17) becomes equal to 1, also resulting in Equation (2.19).

Even though Laplace's equation can also be derived from the linearised potential equation, it is important to note that the assumption of small perturbations need not apply for Laplace's equation. This assumption was used to simplify Equation (2.16), but that simplification is not necessary for incompressible flow: all these terms are multiplied with M_∞^2 , which – as shown in the previous paragraph – tends to 0 when ρ is constant.

As Laplace's equation is linear and has exact solutions, it does not have to be discretised to be solved. Solution methods for Laplace's equation are discussed in Section 3.2.

2.7. Empirical methods

At the bottom right of Figure 2.1, empirical methods can be found. Although these do not *model* the flow, they can be used to estimate aerodynamic performance (Gu et al., 2018) – which is what the aforementioned flow models are ultimately used for in aerodynamic design. Empirical methods can be used for rough estimates of properties like lift coefficient, drag coefficient, aerodynamic efficiency at the complete aircraft (Gu et al., 2018) or system level (e.g. Roskam (1985)).

Various empirical methods exist. Well-known are the IHS Engineering Sciences Data Unit Aerospace Package (ESDU, IHS) and the US Air Force data compendium or DATCOM (Hoak, 1978). Whereas the DATCOM is focused on estimating stability and control derivatives, the ESDU spans much more topics, ranging from atmospheric properties to structures and from drag estimation to power plant integration effects. Empirical relations and reference data useful for conceptual aircraft design (weight estimation, sizing, performance) can be found in many aircraft design textbooks, such as Roskam (1985), Torenbeek (1982), Raymer (1992), Sadraey (2013) and Sforza (2014).

3

Overview of solution methods

With the exception of empirical methods used for aerodynamic performance estimation, the flow models treated in Chapter 2 only *describe* the flow. Although these equations ‘speak words’, as Anderson (2001) reminds us, they do not readily show velocity and pressure distributions throughout the flow, let alone aerodynamic force coefficients. In order to find these parameters, mathematical methods are applied to find solutions to the flow models.

In general, two types of solution methods can be distinguished: non-linear and linear methods. These are treated in Sections 3.1 and 3.2, respectively. Furthermore, Section 3.3 treats the topic of boundary conditions, which are used to constrain the solution of the differential equations used. The discussion in this chapter is mostly concerned with the underlying concepts – as Chapter 4 will show, various implementations exist of any of the methods shown here.

3.1. Non-linear solution methods

Non-linear solution methods are, as the name suggests, applied to solve non-linear flow models, such as the RANS and Euler equations and the full potential equation. They split the fluid domain into a finite number of elements to which the conservation laws (of mass, momentum and energy) are applied. Most often, either finite volume (FVM), element (FEM) or difference (FDM) methods are used (Blazek, 2007; Mariens, 2012).

3.1.1. Finite difference methods (FDM)

Finite difference methods are the oldest (Mariens, 2012; Bakker, 2006). They are based on a Taylor series expansion (Anderson, 2001; Kuzmin; Blazek, 2007; Anderson et al., 2009) at each grid point or *node*, where the partial derivatives in the flow model are replaced with (and therefore approximated by) “algebraic difference quotients” (Anderson et al., 2009, p. 88). This yields a set of algebraic equations that can be solved over the entire grid, providing field variables (such as pressure, density and velocity) at the nodes. As the values at node i are computed based on the values at node $i - 1$, the grid needs to be structured in a Cartesian coordinate system (Blazek, 2007). Furthermore, if the nodes are too far apart, the conservation laws no longer hold. On the other hand, the method is easy to understand and apply (Bakker, 2006).

3.1.2. Finite element methods (FEM)

Finite element methods – best known from application in structural analysis problems, but also used in fluid dynamics – take a different approach. First, a grid is generated, which can be structured or unstructured (Anderson et al., 2009). Then, points are defined, which can lay inside an element or on its boundary, at which the solution will be obtained. Next, so-called *basis functions* are chosen, that determine the variation of the flow properties inside each element. Outside the element for which they are defined, these basis functions are zero (Blazek, 2007). These can be linear or higher-order, but their form has to be assumed up front (Anderson et al., 2009). Contrary to FDM and FVM approaches, finite element methods solve an integral representation of the differential equation. (Blazek (2007) and Anderson et al. (2009) further detail ways to obtain this integral form.) The major disadvantage of FEM is increased computational cost and the fact that it less suited for turbulent flow (Bakker, 2006). Also, it is deemed more difficult to understand conceptually. On the other hand, the accuracy that can be obtained by FEM is unmatched by any of the other methods treated here. This can be explained by the fact that FEM aims to solve an integral form of a PDE, rather than the PDE itself (Anderson et al., 2009, Ch. 10).

3.1.3. Finite volume methods (FVM)

Finite volume methods are the last non-linear method discussed here and might be most closely related to the physical phenomena observed in the flow. The discretisation step splits the flow field up into so-called *cells*, which can lie in an structured or unstructured grid (Bakker, 2006). In addition to a computational node placed in the centre of each cell, there are nodes on the boundaries. These nodes can then be defined as the centre of a *control volume*. If the computational node is chosen, the cell acts as a control volume; if a boundary node is chosen, the control volume is made by the union of adjacent cells, or a new volume with the node as centre (Blazek, 2007). Ultimately, the conservation laws are directly applied to the control volumes. An important advantage of actually solving for these conserved variables is that discontinuities (such as shocks) do not form a problem for the finite volume method (Anderson et al., 2009). Also, the FVM is generally considered more easy to understand as it more closely resembles the physical problem, especially when compared to FEM. It is however not free from disadvantages, as it is less accurate in viscous flow regions and higher order accuracy is difficult to obtain (Anderson et al., 2009, Ch. 11). The first downside is caused by the lack of a FEM-like *weak formulation* that allows higher-order derivatives to be translated into lower-order ones, the second by the fact that it is difficult to implement curved boundaries in FVM, limiting most methods to piecewise constant or piecewise linear functions. Still, the method is very popular today (Blazek, 2007).

3.2. Linear solution methods

Whereas flow models higher up the hierarchy shown in Figure 2.1 are non-linear, Laplace's equation (introduced in Section 2.6) is in fact linear. Because of this, well-known solutions to simpler flows can be superimposed to find solutions to more complicated ones. Various so-called *elementary solutions* (Anderson, 2001) (also known as *singularities* by Bertin and Cummings (2009) or *basic solutions* by Katz and Plotkin (1991)) exist. They are schematically visualised in Figure 3.1 and listed below:

- **uniform flow**, coming from one direction at freestream velocity;
- **source flow**, emanating radially outward from a single point;
- **doublet flow**, a combination of two sources of equal but opposite strength, resulting in a “double-lobed circular flow pattern” (Anderson, 2001, p. 223); and
- **vortex flow**, with concentric streamlines.

Of these four, only vortex flow produces lift. This can be explained by the fact that the circulation around the streamline of a vortex flow is finite and the relation of circulation to lift by the Kutta-Joukowski theorem shown in Equation (3.1):

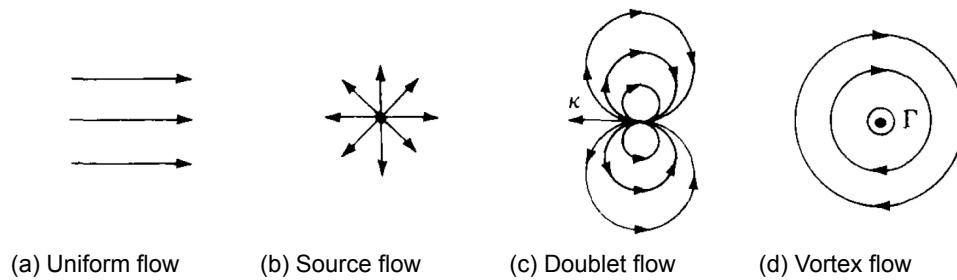


Figure 3.1: Elementary flow solutions (Anderson, 2001)

$$L = \rho_{\infty} V_{\infty} \Gamma \quad (3.1)$$

A line of vortices ‘behind’ each other (as a line perpendicular to a point on this page) is a vortex filament. Vortex filaments have a constant strength Γ along its length and cannot end in a flow – but have to continue to infinity, or form a closed loop (Anderson, 2001, Ch. 5). From Γ , the velocity can be found using the Biot-Savart law (a solution to Laplace’s equation) and the lift follows from the Kutta-Joukowski theorem.

Multiple linear solution methods exist and are discussed in the remainder of this section, which is again largely based on Anderson (2001). The lifting line and lifting surface theory are treated in Section 3.2.1, the vortex lattice method (VLM) in Section 3.2.2 and the panel method in Section 3.2.3. Ultimately, however, all methods aim to find a singularity distribution (either vortices or a combination of basic elements) such that particular boundary conditions are met. These are discussed further in Section 3.3.

3.2.1. Lifting line and lifting surface theory (LLT / LST)

In lifting line theory (LLT), the wing (or other lifting surface) is replaced by a bound (i.e., fixed in the flow, rather than moving with it) vortex filament, spanning from wing tip to wing tip and located at the line connecting the aerodynamic centres of the wing sections. As a vortex filament cannot end in the flow, it is assumed the bound vortex gives rise to two free vortices at each of the wing tips. These free vortices continue downstream to infinity and – together with the bound vortex – form a *horseshoe vortex*.

Yet, just a single horseshoe vortex is not able to properly describe the lift distribution. To solve this problem, multiple horseshoe vortices can be superimposed, as shown in Figure 3.2. If an infinite number of horseshoe vortices is combined this way, the vortex distribution along the lifting line becomes continuous ($\Gamma(y)$) and the downstream vortices form a vortex sheet. From this vortex sheet, the lift distribution, lift force and induced drag can be computed, as further detailed in Anderson (2001).

For straight wings (i.e., without sweep) with a moderate to high aspect ratio (above 4, as a general rule-of-thumb (Anderson, 2001)), the lifting line theory provides reasonable results. However, the method is not fit for use with other wing types and geometries. This is solved by placing an infinitesimal number of lifting lines in chordwise direction to yield a vortex sheet. Its strength is given by $\gamma(x, y)$. The trailing vortices form another vortex sheet, with strength $\delta(x, y)$. Both γ and δ also depend on y as multiple horseshoe vortices are superimposed on each lifting line. These two vortex sheets form a lifting surface over the wing. From the trailing edge onward, the trailing vortices extending to infinity form a wake vortex sheet. This is known as the lifting surface theory (LST).

Following the Biot-Savart law, both the lifting surface and the wake vortex sheet induce a normal velocity at every point on the wing, designated $w(x, y)$. The flow tangency boundary condition forces the sum of $w(x, y)$ and the component of the freestream normal to the wing (a result of wing tip vortices, which induce downwash and rotate the relative wind upward from the freestream direction) to be equal to zero. This solution, then, again allows for finding the relevant aerodynamic variables.

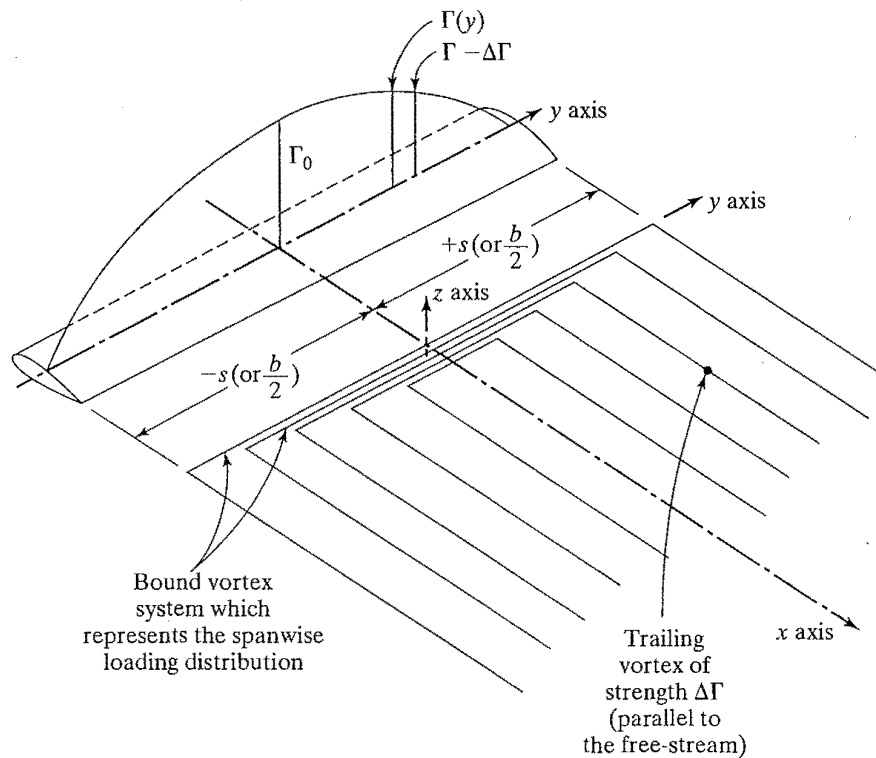


Figure 3.2: Superposition of a finite number of horseshoe vortices along the lifting line, showing the trailing-vortex system (Bertin and Cummings, 2009, p. 324)

A limitation that holds both for the lifting line and lifting surface theory is that thin airfoils (or other lifting surfaces) are assumed. The lift slopes are also considered to be linear, which only holds for small angles of attack.

3.2.2. Vortex lattice method (VLM)

The vortex lattice method (VLM) takes a simpler approach to the same concept already used in the LST. First, the surface is split up in quadrilateral panels. Then, a horseshoe vortex with strength Γ_i is placed on the quarter-chord line of each panel. The downstream trailing components of this vortex follow the edges of the panel. This way, the entire surface is covered in horseshoe vortices, as visualised in Figure 3.3. Using the Biot-Savart law and applying the flow tangency condition at control points at 75% of each panel's chord, the vortex strengths can be computed. These – in turn – can be used to compute lift and induced drag.

Compared to the lifting surface theory, the vortex lattice method is simpler because the numerical solution directly computes the unknown vortex strength Γ_i (compare Figure 3.2, showing overlapping horseshoe vortices, with Figure 3.3, without). Despite this, the underlying assumptions (thin airfoils at a small angle of attack) have not changed, as the vortex filaments are placed on the local chord line (i.e., 'inside' the body) Mariens (2012).

3.2.3. Panel method

Contrary to the methods presented above, the panel method has been extended for analysis of three-dimensional geometries (Hess, 1988), such as thicker airfoils, fuselages, engine nacelles, and so on. This can be seen in Figure 3.4, showing a panel representation of a McDonnell Douglas DC-10, and in Figure 3.6, showing a less densely panelled generic transport aircraft. Since the 1960s, they have

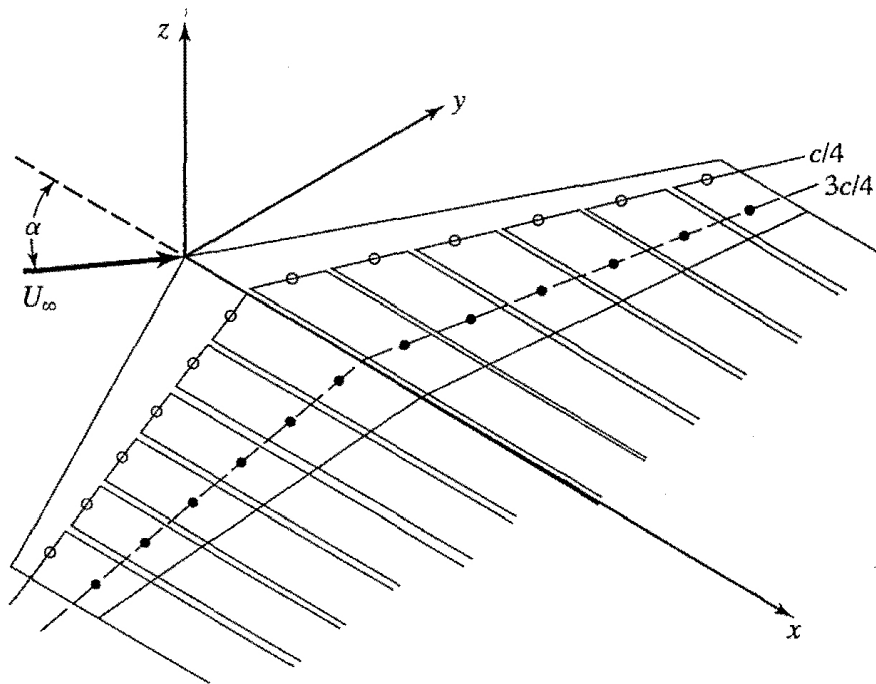


Figure 3.3: Distributed horseshoe vortices over a swept wing with 12 panels (Bertin and Cummings, 2009, p. 355)

seen widespread use (Schippers, 1988). As with the VLM, the geometry is covered in (quadrilateral or triangular (Mason, 1995)) panels and a singularity (or distribution of identical or different singularities) is added to each panel, based on the assumed flow type (lifting or non-lifting, linearly or quadratically varying, etc.) at that panel. A set of equations can be set up and subsequently solved to find the singularity strengths at each panel. These can in turn be used to find the velocity and pressure fields.

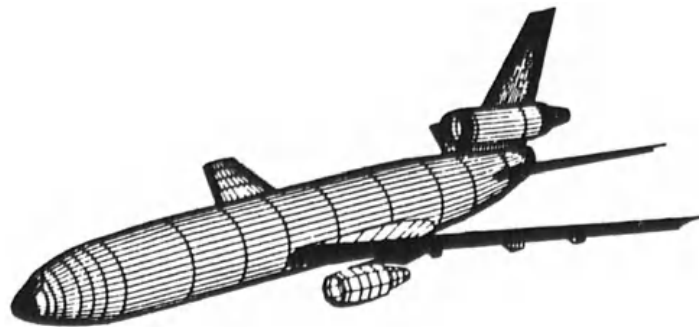


Figure 3.4: Panelling of a McDonnell Douglas DC-10 jet transport, illustrating the ability of panel methods to accurately represent three-dimensional geometries (Hess, 1988, p. 173)

3.3. Boundary conditions

As the physical flow models treated in Chapter 2 that are based on partial differential equations each can describe a multitude of flows, boundary conditions have to be specified in order to ‘fix’ the solution. It is therefore no surprise that different aerodynamic solvers employ different boundary conditions. This is to a large extent caused by the type of partial differential equation that is used to describe the flow (Cummings et al., 2015; Hirsch, 2007). Still, some underlying concepts are shared by all. These are explained in this section, starting with boundary conditions at the far-field (‘infinity’) before moving on to boundary conditions at the wall or surface. Lastly, some implementation aspects are discussed.

3.3.1. Far-field boundary conditions

In most applications, the flow far away from the object of interest is at free stream conditions (Cummings et al., 2015). Aligning the surface of interest with the x -axis, this means that the y - and z -components of the velocity are zero and $u = V_\infty$ (Anderson, 2001). According to Anderson (2001) these conditions apply both upstream and downstream (Bertin and Cummings (2009) seems to implicitly agree), Cummings et al. (2015) proposes to only enforce this condition at the inflow boundary and to set $\partial V_{out}/\partial x = 0$ at the outflow boundary. In viscous problems, the total temperature and total pressure are also specified (Cummings et al., 2015; Hirsch, 2007). Rather than prescribing fixed conditions, Riemann invariants can be used. This method relies on finding the characteristics of the flow near the boundary conditions, and using these to find the actual values to be fixed at the boundary (Cummings et al., 2015) (see Anderson (1995), Anderson (2001), Blazek (2007), Cummings et al. (2015) and Hirsch (2007)).

3.3.2. Surface boundary conditions

Moving to the object that is in the flow, the viscosity of the flow determines which boundary conditions are applicable. If viscosity is completely neglected, there is no physical principle that makes flow ‘stick’ to the surface. If the wall is solid, there is no mass flowing through the wall, such that the velocity must be tangent to the surface at all points – leading to the name of *wall tangency* or *flow tangency* condition (Anderson, 1995). It means that, assuming a fixed, rigid and solid surface, Equation (3.2) holds at the surface (Blazek, 2007).

$$\mathbf{V} \cdot \mathbf{n} = 0 \quad (3.2)$$

\mathbf{V} is the velocity vector; \mathbf{n} the surface normal. In case of potential flow, Equation (3.2) can be rewritten to Equation (3.3) (Anderson, 2001):

$$\mathbf{V} \cdot \mathbf{n} = (\nabla\phi) \cdot \mathbf{n} = 0 \quad (3.3)$$

As $\mathbf{n} \neq 0$, Equation (3.3) can only be satisfied if the change in potential normal to the surface is 0 or – equivalently – if the change in stream function (indicated by ϕ) along the surface (measured by s) is 0, as shown in Equation (3.4) (Anderson, 2001):

$$\frac{\partial\phi}{\partial n} = 0 \quad (3.4a)$$

$$\frac{\partial\phi}{\partial s} = 0 \quad (3.4b)$$

Physically, it ensures that the surface is a stream line of the flow (Anderson, 2001). This situation is sketched in Figure 3.5. If the surface is porous (or modelled as such, for example in case of an inlet or exhaust) or a boundary layer model is coupled, a non-zero normal velocity is allowed.

In linear potential flows (governed by Laplace’s equation, as discussed in Section 2.6), boundary conditions determine the distribution of singularity strengths (Bertin and Cummings, 2009). The Kutta condition – stating $\gamma_{TE} = 0$ – prescribes that for bodies with a sharp trailing edge, the stagnation point is at that trailing edge so that the flows coming from the upper and lower surfaces join smoothly. In panel methods, the strength of the source distribution is bounded being equal to the normal velocity to the panel surface. The vortex strengths in a VLM code can be found by having them satisfy the flow tangency boundary condition.

Contrary to the inviscid case, viscous flow does stick to the surface due to shear stresses at the wall. This is modelled using the so-called *no-slip* boundary condition, that dictates all velocity components at the wall to be zero (Blazek, 2007). As viscosity also brings possible heat transfer effects, a second

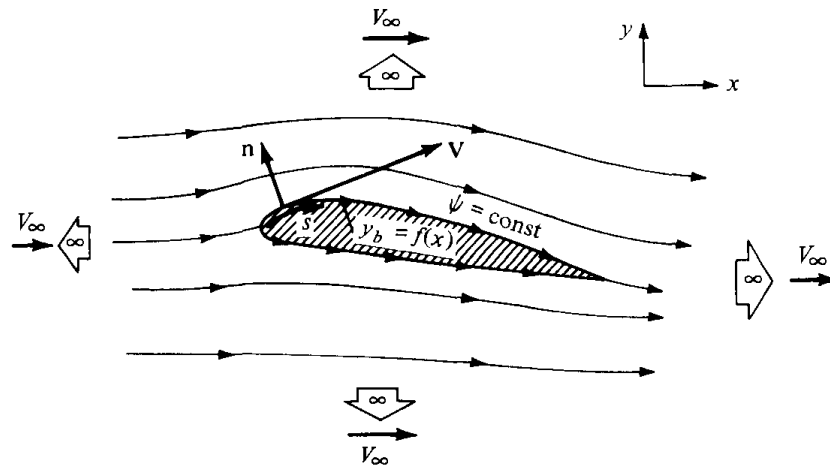


Figure 3.5: Surface and far-field (following Anderson's notion of outflow velocity equal to V_∞) boundary conditions on an airfoil in inviscid flow (Anderson, 2001, p. 209)

boundary condition is required. This can either be a prescribed wall temperature or a specified heat flux normal to the surface. For adiabatic flows, this is zero. At the edge of a viscous boundary layer, y tends to ∞ , $u = U_e$ and $h = h_e$, to ensure no step discontinuities from the viscous to the inviscid flow domain (Anderson, 2001).

Boundary conditions that prescribe a particular value to one of the dependent variables along the boundary (such as the temperature requirement) are *Dirichlet boundary conditions*. *Neumann boundary conditions*, on the other hand, define the value of the derivative of a dependent variables (such as the heat flux). Combinations also exist, which are called *Robin boundary conditions* (Cummings et al., 2015). Neumann boundary conditions are often used for analysis problems where the value of certain quantities of interest on the boundary is unknown. Dirichlet conditions, on the other hand, are often regarded as design conditions. Using these, it is possible to find a boundary (such as an airfoil shape) that satisfies a prescribed flow.

3.3.3. Numerical implementation

Given the fact that surface conditions prescribe the flow parallel or perpendicular to the surface, it is of crucial importance that the control points (illustrated in Figure 3.6) at which the boundary layers are applied coincide with the actual boundary of the surface (Anderson, 2001). To make this more straightforward, coordinate transformations are often applied. This can entail a transformation of the grid (as is done for thin-layer Navier-Stokes, discussed in Section 2.1.5), but it is also possible to transform the boundary conditions. The fact that boundary conditions are applied at each control point also explains part of the steep rise of computational cost with an increasing amount of panels or grid points.

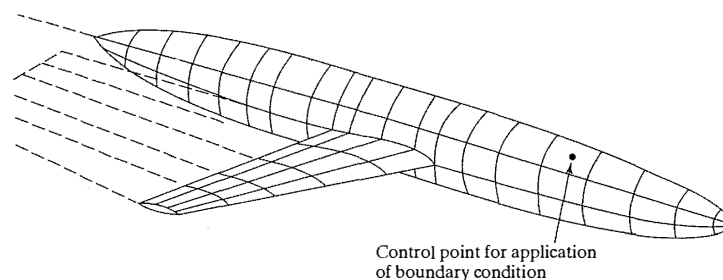


Figure 3.6: Panel representation of an airplane, showing a single control point for boundary layer application. Adapted from Bertin and Cummings (2009, p. 350)

Similarly, when modelling the far-field boundary conditions, one of the major challenges is determining how far is far enough. Imposing far-field boundary conditions too close to the object of interest reduces accuracy or effectively invalidates the solution, but taking more distance than necessary increases the size of the computational domain – and thereby computational cost (Thomas and Salasf, 1986). The type of flow also steers this choice, because information propagation is different (more wide-spread) in subsonic flow than in supersonic flow (Cummings et al., 2015).

A more elaborate discussion of the numerical implementation of various boundary conditions can be found in Blazek (2007, Ch. 8), Cummings et al. (2015), Ferziger and Perić (2002), Hirsch (2007), Moran (1984) and Katz and Plotkin (1991).

4

Overview of solvers

Chapter 2 treated models to describe the flow and Chapter 3 discussed the concepts behind some popular solution methods to these flow models. However, just as there were multiple solution methods for a particular flow model, there are multiple variants or implementation of a particular solution method. These implementations, referred to as *aerodynamic solvers* or just *solvers*, are the subject of the current chapter.

It is split up in three sections. Section 4.1 treats solvers used for two-dimensional cases: infinite wings and airfoils. Section 4.2 discusses solvers that are three-dimensional in nature. As some solvers combine two- and three-dimensional computations, ‘hybrid’ or 2.5D solvers also exist. These tools are the subject of Section 4.3. The subsections discussing 2D and 3D solvers first treat the flow model. If applicable, this subsection is further split to discuss separate inviscid and viscous routines, and their coupling. Boundary layer transition and separation – if applicable – are also treated. Then, the solution procedure is discussed, mostly dealing with relevant numerical details. Boundary conditions are either treated in the flow model or solution method parts, depending on which is most applicable. Finally, some words are spent on the type and format of the output, as well as reported results obtained with the program under consideration, often in comparison to other simulation methods or wind tunnel results¹. The subsections pertaining to hybrid solvers are split up into two, discussing the two- or three-dimensional aspects of the program. A comparative review highlighting the main similarities and differences of the methods of a particular type (2D, 3D or hybrid) is found at the end of each section (Section 4.1.5, Section 4.2.6 and Section 4.3.3, respectively).

Table 4.1 provides a more detailed overview of the solvers considered in this chapter, split in the 2D / 3D / hybrid-categories introduced before. The first group of columns shows when the solver was first developed, which flow model and solution method(s) are used and whether it supports analysis and/or design use. The second group shows to what extent viscosity is included and whether the solver is limited (or best suited to) a particular Mach or Reynolds number range. Please note Mach number ranges are to be read as “up to”. The third set of columns show the distribution (e.g. open source or commercial, the latter giving a cost advantage but a possible quality disadvantage (Vogeltanz, 2015)), a reference to the primary publication of the method and the amount that publication has been cited (in Google Scholar) – to provide an indication of popularity of the solver. The last column shows the section and page number in the current text where the solver is further detailed.

Table 4.2 shows which flow model(s) – in rows – and solution method(s) – in columns – are used in each of the solvers. For clarity, two- and three-dimensional solvers are separated, with the intermediate hybrid solvers included in both groups.

¹Validation based on experimental results might seem best, but if a method makes particular assumptions that make it fundamentally different from the experiment, the comparison is unfair.

Table 4.1: Overview of solvers (Mariens et al., 2014; Deperrois, 2011b; Drela and Youngren, 2010; Drela, 2007; Maskew, 1982a; Mariens, 2012; Freestone, 2004; Drela, 1994; Atkin and Gowree, 2012; Florjancic, 2015; Myers, 2012; Palacios et al., 2013; Drela, 1989)

	Solver	Year	Model	Method	Use	Viscosity	Mach \leq	Reyn.	Distribution	Publication	Cited	Section
2D	XFOIL	1986	Laplace	2D panel	Analysis + design	Optional (BL + VII)	0.7	“low”	Open source	Drela (1989)	1529	4.1.1, p. 26
	VGK	1970s	Full potential	FDM	Analysis	Optional (BL + VII)	Sub-sonic ²		Commercial / academic	Freestone (2004)	8	4.1.2, p. 30
	MSES	1994	Euler	FVM	Analysis + design	Optional (BL + VII)	Trans-sonic	“low”	Commercial / academic	Drela (1990)	134	4.1.3, p. 37
	ARC2D	1984	Euler, TLNS	FDM	Analysis	Optional			Commercial (US)	Pulliam (1984)	151	4.1.4, p. 39
3D	AVL	1988	Laplace	VLM	Analysis	User-input	0.6		Open source		95 ³	4.2.1, p. 45
	Tornado	2001	Laplace	VLM	Analysis	No			Open source	Melin (2000)	232	4.2.2, p. 46
	VSAERO	1982	Laplace	3D panel	Analysis	Yes (BL + VII)	Sub-sonic		Commercial	Maskew (1982b)	67	4.2.3, p. 49
	MATRICES / -V	1986 / 1992	Full potential	FVM	Analysis	No / Yes (BL + VII)	Trans-sonic	“high”		van der Vooren et al. (1986) / van der Wees and van Muijden (1992)	2 / 6	4.2.4, p. 53
	SU2	2012	Euler, RANS, laminar NS	FVM / FEM	Analysis + design	Optional	Hyper-sonic		Open source	Palacios et al. (2013)	225	4.2.5, p. 59

Continued on next page

²Flow solutions for locally supersonic flows closely correspond to reality, as long as the Mach number of the flow directly upstream of the shock does not exceed 1.3 ([Freestone, 2004](#)).

³Number of search results for Scopus-query TITLE-ABS-KEY(AVL or “Athena Vortex Lattice”) AND TITLE-ABS-KEY(a*foil OR wing OR a*plane OR a*craft OR aerial or aero* or Drela), 17/08/2018.

Table 4.1: Overview of solvers (Mariens et al., 2014; Deperrois, 2011b; Drela and Youngren, 2010; Drela, 2007; Maskew, 1982a; Mariens, 2012; Freestone, 2004; Drela, 1994; Atkin and Gowree, 2012; Florjancic, 2015; Myers, 2012; Palacios et al., 2013; Drela, 1989) – continued

	Solver	Year	Model	Method	Use	Viscosity	Mach \leq	Reyn.	Distribution	Publication	Cited	Section
Hybrid	XFLR5	2003	Laplace	2D panel + LLT / VLM / 3D panel	Analysis + design	Optional (BL + VII)	0.7	“low”	Open source	Deperrois (2011b)	18	4.3.1, p. 67
	Q3D	2012	Laplace (+ Full potential / Euler)	2D panel + VLM	Analysis	Optional (BL + VII)	Transonic			Mariens et al. (2014)	21	4.3.2, p. 69

Table 4.2: Combinations of flow model(s) – in rows – and solution method(s) – in columns – used in solvers

	2D						3D							
	FDM	FEM	FVM	LLT	VLM	Panel	FDM	FEM	FVM	LLT	VLM	Panel		
Navier-Stokes														
Laminar NS														
RANS							SU2 SU2							
TLNS	ARC2D													
Boundary layer	VGK Q3D	Q3D				XFOIL XFLR5 Q3D	MATRICS-V					VSAERO		
Euler	ARC2D MSES						SU2 SU2							
Full potential	VGK						MATRICS / -V							
Laplace							XFOIL						XFLR5 AVL Tornado XFLR5 Q3D	VSAERO XFLR5

4.1. Two-dimensional solvers

This section treats two-dimensional solvers. These are called two-dimensional as they model an infinite wing and effects such as crossflow or tip vortices are thereby neglected. 2D solvers are used for analysis (and/or design) of airfoils. Contrary to most three-dimensional programs, discussed in Section 4.2, 2D codes often include a viscous component. This is because 2D boundary layers are much easier to solve than 3D boundary layers.

In the next few sections, the programs XFOIL (Section 4.1.1), VGK (Section 4.1.2), MSES (Section 4.1.3) and ARC2D (Section 4.1.4) are treated in further detail. Section 4.1.5 provides a comparative review of these solvers.

4.1.1. XFOIL

XFOIL was developed in 1986 by Mark Drela and Harold Youngren at MIT (Drela and Youngren, 2013a, 2001). It is a very popular command-line operated 2D “inviscid linear-vorticity panel method” with an optional boundary layer model based on source distributions in order to model viscous effects on the potential flow (Drela, 1989, p. 1). The code includes a Karman-Tsien compressibility correction to provide more accurate results at higher subsonic Mach numbers. The program is particularly suited to low Reynolds number⁴ airfoils, which is why it is often used for design and analysis (the program supports both) of unmanned or micro aerial vehicles (e.g. Ahn and Lee (2012)).

A user manual to the current version (6.9) is available (Drela and Youngren, 2001). In addition, Drela (1989) outlines the theoretical formulations of XFOIL. Unless indicated otherwise, the information in the remainder of this section is based on these references.

Flow model

XFOIL includes both an inviscid and a viscous formulation, treated in the following sections.

Inviscid formulation

The inviscid flowfield is composed from a freestream flow, a vortex sheet (on the surface of the airfoil) and a source sheet (on both the surface of the airfoil and the wake). The vortex strength on each panel varies linearly, whereas the source strengths on the airfoil are constant per panel. In the wake, the source strengths vary linearly. The panels themselves are flat, with the amount user-specified (default 160) and more panels placed in regions of higher curvature. The trailing edge gap is closed by a vertical panel, on which a source and a vortex singularity are placed. The Kutta condition ($\gamma_{TE} = 0$) is modelled as $\gamma_1 + \gamma_N = 0$, with γ_1 and γ_N corresponding to the TE-most point on the upper and lower surface, respectively. If the trailing edge is sharp (i.e., without trailing edge gap), the aforementioned procedure will not work and the Kutta condition is applied by summing the weighted averages of the three TE-most vortices on both surfaces. Figure 4.1 illustrates this.

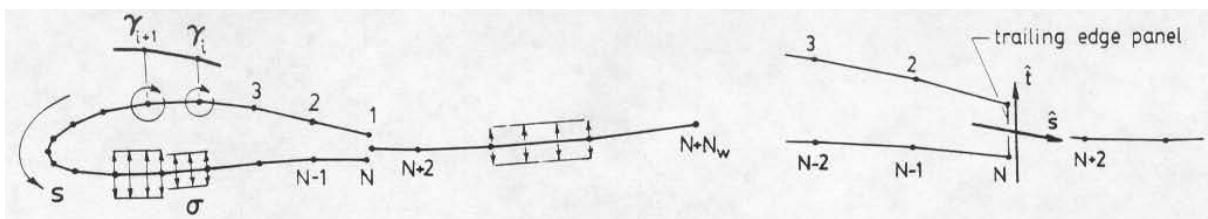


Figure 4.1: Airfoil and wake panels in XFOIL, showing panel numbering and singularity distributions (Drela, 1989, p. 2)

Inviscid vortex strengths are found by combining vorticity distributions at freestream angles of attack of

⁴Definitions what ‘low’ is, however, differ substantially. Drela (1989) describes these as $\leq 0.5 \cdot 10^6$, others range from ‘below 10^5 ’ to ‘ 10^6 and higher’ (Morgado et al., 2016; Mushynski and Jon, 2017; Castegnaro, 2017; Fernandes et al., 2014; Van Treuren, 2015).

0° and 90°, calculated by XFOIL itself, as shown in Equation (4.1):

$$\gamma_i = \gamma_{0_i} \cos \alpha + \gamma_{90_i} \sin \alpha \quad (4.1)$$

Viscous formulation

The viscous calculation method is largely identical to an earlier code called ISES, also developed by Drela (Drela and Giles, 1987a; Giles and Drela, 1987), improved with a new boundary layer formulation for blunt trailing edges. The methodology implemented in both codes, documented in Drela and Giles (1987b), is a two-equation integral formulation, based on dissipation closure. Although integral formulations (solving one or more ODEs) are usually regarded as less accurate than formulations based on differential techniques (solving a set of PDEs), the former are easier to solve and less computationally expensive – an important asset to an iterative design tool. The two equations used in the XFOIL code are shown in Equations (4.2) and (4.3):

$$\frac{d\theta}{d\xi} + (2 + H - M_e^2) \frac{\theta}{u_e} \frac{du_e}{d\xi} = \frac{C_f}{2} \quad (4.2)$$

$$\theta \frac{dH^*}{d\xi} + [2H^{**} + H^* (1 - H)] \frac{\theta}{u_e} \frac{du_e}{d\xi} = 2C_D - H^* \frac{C_f}{2} \quad (4.3)$$

Equation (4.2) shows the von Kármán momentum integral equation; Equation (4.3) the kinetic energy shape parameter equation, derived in Drela (1985). In this set of equations, H^* (the kinetic energy shape parameter), H^{**} (the density shape parameter), C_f (the skin friction coefficient) and C_D (dissipation coefficient) are unknown, but assumed dependent on H_k (the kinematic shape parameter with constant density across the boundary layer), M_e (Mach number at the end of the boundary layer) and Re_θ (momentum thickness Reynolds number). H_k is related to the regular shape parameter H and M_e as given in Equation (4.4) (Whitfield, 1978)⁵:

$$H_k = \frac{H - 0.290M_e^2}{1 + 0.113M_e^2} \quad (4.4)$$

Laminar flow In laminar flow, straight-line approximations to the Falkner-Skan one-parameter profile family are used to establish $H^* = H^*(H_k)$, $C_f = C_f(H_k, Re_\theta)$ and $C_D = C_D(H^*, H_k, Re_\theta)$, further detailed in Drela and Giles (1987b) (Coder and Maughmer, 2014). An expression for H^{**} is derived by Whitfield (1978, Eq. (46)) (using the symbol $H_{\delta^{**}}$) for a turbulent flow, but is also used in the laminar case as “ H^{**} has a fairly small effect in transonic flows and is negligible at low subsonic speeds” (Drela and Giles, 1987b, p. 1349). It is shown in Equation (4.5):

$$H^{**} = \left(\frac{0.064}{H_k - 0.8} + 0.251 \right) M_e^2 \quad (4.5)$$

Turbulent flow For turbulent flows, different closure relations are used, based on Swafford (1980, Eqs. (12), (30)). These hold for a separated, turbulent boundary layer and assume a smooth, impermeable and adiabatic wall. With this approach, H_k becomes a function of Re_θ , H_k itself and H_0 , a function of Re_θ . The contributions to dissipation of the wall layer (scaling with C_f) and the wake layer (scaling with C_τ) are summed in C_D . As the Reynolds stresses respond somewhat slower to changing conditions, a lag is introduced using the rate equation shown in Equation (4.6). This equation, used in XFOIL, is different from the one used in ISES (documented in Drela and Giles (1987b)) and has yielded better lift and drag predictions near stall conditions (Drela, 1989).

⁵Whitfield (1978) uses the symbol H_{δ^*} for H and \bar{H} for H_k . Equation (4.4) is obtained by rewriting Equation (44) in Whitfield (1978) for \bar{H} .

$$\frac{\delta}{C_\tau} \frac{dC_\tau}{d\xi} = 5.6 \left(\sqrt{C_{\tau_{EQ}}} - \sqrt{C_\tau} \right) + 2\delta \left(\frac{4}{3\delta^*} \left[\frac{C_f}{2} - \left(\frac{H_k - 1}{6.7H_k} \right)^2 \right] - \frac{1}{u_e} \frac{du_e}{d\xi} \right) \quad (4.6)$$

Since version 6.99, the shear lag constant (5.6) and weight (6.7) can be user-adjusted (Drela and Youngren, 2013b).

Transition The transition point is predicted based on Orr-Sommerfeld spatial amplification theory. Whereas the full e^n method (van Ingen, 1956) assumes transition to occur when the most unstable Tollmien-Schlichting wave has grown by a factor of n (in case of XFOIL, the default value is 9, yielding $e^9 \approx 8100$), XFOIL uses an envelope method (van Ingen, 2008; Lasauskas and Naujokaitis, 2009; Morgado et al., 2016). This does not track the amplification of individual Tollmien-Schlichting waves, but gives the total amplification at a point – that is, the amplitude of the frequency that is most amplified at that location. It is computationally less expensive than the full method, but also somewhat less accurate (Dini et al., 1992).

The actual growth is modelled by Equation (4.7), in which the terms on the right hand side of the equation are empirically determined from solutions to Orr-Sommerfeld equation (first term) and from properties of the Falkner-Skan family of profiles (second term) (Drela and Giles, 1987b; Drela, 1989). These expressions are shown in Drela and Giles (1987b, Eqs. (29), (32)-(35)).

$$\frac{d\tilde{n}}{d\xi} = \frac{d\tilde{n}}{dRe_\theta}(H_k) \cdot \frac{dRe_\theta}{d\xi}(H_k, \theta) \quad (4.7)$$

\tilde{n} is the logarithm of the amplification factor. Rather than directly integrating $d\tilde{n}$ with respect to $d\xi$, Equation (4.7) is discretized and solved for \tilde{n} , which is treated as a boundary layer variable.

Besides transition, XFOIL is able to model separation (Drela, 1989; Fernandes et al., 2014). This includes separation bubbles.

Wake Only turbulent wakes are considered, as laminar wakes do not occur in the flows considered (Drela and Giles, 1987b). In ISES, the wake consists of two boundary layers without wall shear (Drela and Giles, 1987a). XFOIL, however, treats the wake “as one viscous layer so that only one θ and one δ^* variable is present at each wake station” (Drela, 1989, p. 7). Initial momentum and displacement thicknesses are found by summing the upper and lower trailing edge values. C_τ is obtained by taking a θ -weighted average of upper and lower surface values.

Viscous / inviscid coupling

At the core of the viscous-inviscid interaction method used in XFOIL are two separate flow regimes, discussed in the previous sections, that meet at the boundary layer edge (indicated with subscript $(\)_e$). At the airfoil surface, u_e is set equal to the vorticity (γ on the suction side, $-\gamma$ on the pressure side) at each panel. In the wake, u_e is equal to the gradient of the stream function component normal to the wake. With the notion that the strength of the source is equal to the gradient of the mass defect at each panel, u_e can be expressed as shown in Equation (4.8):

$$u_{ei} = u_{INV_i} + \sum_{j=1}^{N+N_w-1} d_{ij} m_j \quad ; \quad 1 \leq i \leq N + N_w \quad (4.8)$$

In this equation, u_{INV_i} is the edge velocity distribution without viscous effects, d_{ij} is the mass-influence matrix (determined by the geometry of the airfoil and wake, as well as freestream angle of attack) and m_j the mass defect at panel j . N and N_w are the number of grid points on the airfoil and wake, respectively.

Solution procedure

Solving the viscous system of equations requires finding values for θ , δ^* and a third variable – C_τ in case of turbulent flows, \tilde{n} in case of a laminar boundary layer. The corresponding three coupled and non-linear equations are the momentum equation (Equation (4.2)), the kinetic energy shape parameter equation (Equation (4.3)) and either the lag equation shown in Equation (4.6) (turbulent case) or the amplification equation shown in Equation (4.7) (laminar case). Discretisation is done using two-point central differencing (Drela, 1989), or a hybrid between that and backward Euler in case of Equation (4.3), due to numerical difficulties otherwise coming into play (Drela and Giles, 1987b). The transition interval is treated as two subintervals, with the boundary layer variables obtained through interpolation of the values at neighbouring grid points. Right after transition, $\sqrt{C_\tau}$ is set to 70% of its equilibrium value.

Shifting attention to the coupled inviscid / viscous system, the fact that Equation (4.8) is an explicit expression forms a solvable set of equations when combined with Equations (4.2), (4.3) and (4.6) or (4.7). It is solved by a full Newton method, which yields fast solution times given the regular grids used.

Output

XFOIL output consists of pressure distributions and polars, the latter specifying lift coefficient, drag coefficient (total and pressure drag, such that friction drag can be readily computed as $C_{Df} = C_D - C_{Dp}$), moment coefficient and transition locations on the top and bottom surface. Both pressure distribution and polars can be shown on screen and written to file. XFOIL also provides some basic graphing capabilities, with the ability to save plots to file.

Results

The accuracy of XFOIL is well recognised (Morgado et al., 2016; Selig, 2003) and the program has proven its performance (Ben Mosbah et al., 2016; Madsen and Filippone, 1995; Coutu et al., 2010) as an “excellent airfoil design and analysis tool”, which is substantially easier to use than more complex CFD-codes (Morgado et al., 2016, p. 212). The transition from laminar to turbulent flow is well-predicted (Ben Mosbah et al., 2016). Bodling et al. (2017, p. 11) however note that XFOIL assumes instantaneous transition, whereas higher-order methods show transition behaviour over a finite distance. Nevertheless, a comparison with experimental results of a NACA 0012 profile shows XFOIL predicting the pressure distribution “remarkably well”. Despite these results, others (using a NACA 4415 airfoil) note a 10% difference between experimental and computer pressure values (Popov et al., 2009).

In describing separation, various authors note some shortcomings to the program. The separation point predicted by XFOIL does not always match higher-fidelity codes, which causes XFOIL to predict the stall angle less accurately (Ahn and Lee, 2012). In Venters and Helenbrook (2013) and Maughmer and Coder (2010), separation is predicted later than it occurs in experiments. Accuracy in the stalled regime is therefore also reduced (de Oliveira et al., 2012; Lasauskas and Naujokaitis, 2009; Fuglsang et al., 2016). Compared to experiments and/or more advanced solvers, accurate predictions are observed for the linear part of the lift, drag and moment polars (Ahn and Lee, 2012; Coder and Maughmer, 2014; Ferrer and Munduate, 2009; Lasauskas and Naujokaitis, 2009), although Castegnaro (2017) notes a general overprediction of c_l , which reduces with increasing Reynolds number. Multiple authors agree on the notion that $c_{l,max}$ is regularly overpredicted, as illustrated in Figure 4.2 (Coder and Maughmer, 2014; Venters and Helenbrook, 2013; Lasauskas and Naujokaitis, 2009; Fuglsang et al., 2016; Maughmer and Coder, 2010). Vaithyanathasamy et al. (2018) explain this behaviour by the fact that the empirical closure relations used by XFOIL assume equilibrium flow and therefore are not suited for describing the complex vortex shedding behaviour observed in separated flow. Related to this are some concerns of underpredicted values for c_d , especially (but not strictly limited to) thicker airfoils, such as those used in wind turbines (Ramanujam et al., 2016; Kirk et al., 2014; Maughmer and Coder, 2010). In case of a NACA 63₃-418 airfoil, a 12% underprediction at the minimum drag point was observed (Ramanujam et al., 2016). This is supposedly caused by the limitations of the viscid-inviscid interaction method, underpredicting the boundary layer momentum thickness.

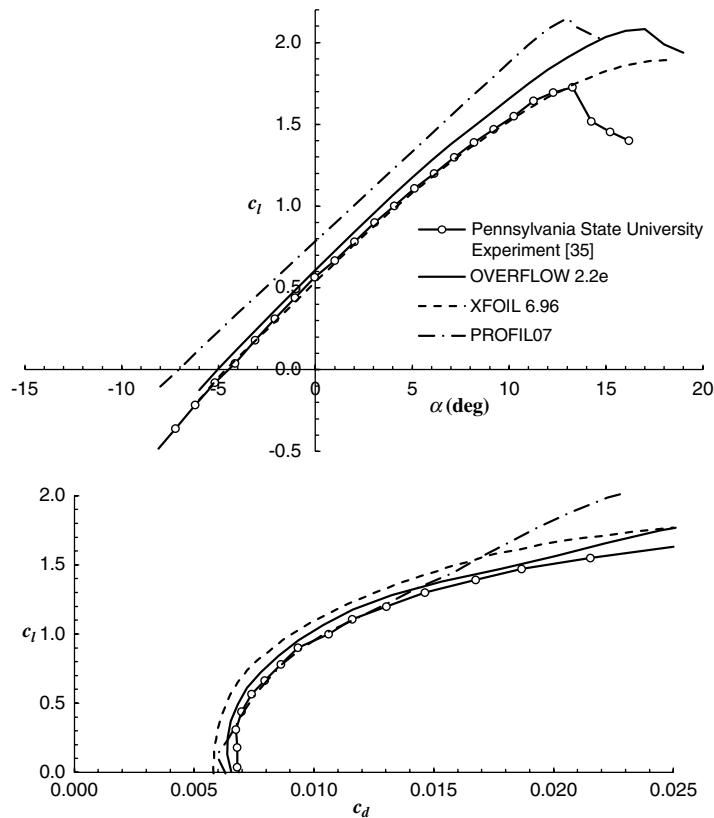


Figure 4.2: Comparison of lift and drag coefficient for the HTR 1555 inboard rotor airfoil (at $Re = 2.0 \cdot 10^6$) as predicted by XFOIL and found in experiment, illustrating good agreement on the linear part of the lift slope, the overprediction of maximum lift coefficient and the underprediction of drag coefficient by XFOIL (Corder and Maughmer, 2014, p. 188), experimental data from Maughmer and Somers (2007)

4.1.2. Viscous Garabedian and Korn (VGK)

VGK (short for *viscous Garabedian and Korn*, after Garabedian and Korn (1971)) is a “computational method for determining two-dimensional transonic attached flow past a lifting aerofoil immersed in a subsonic freestream” (Freestone, 2004, p. 6). It includes both inviscid and viscous formulations and although the program is limited to single-element airfoils, it can also be used for analysis of airfoils with deflected control surfaces. Furthermore, the code predicts the effects of shock waves. The program is an implementation of the full potential equations for steady compressible flow, which are solved using a finite difference method. VGK has been developed by the Royal Aircraft Establishment / Defence Evaluation and Research Agency (RAE / DERA), but is currently commercially licensed by QinetiQ (QinetiQ). First publications about the program stem from 1996 (Freestone, 2004), although Atkin and Gowree (2012) state development goes back to the late 1970s and reports from the 1980s indeed also mention the program (Blockley and Hodges, 1982).

In addition to the commercial license, the software and extensive documentation is also available through IHS ESDU (data items 96028, 96029, 97030, 98031, 99032, 01033 and 03015) (Freestone, 2004, 2010, 2011, 1998, 1999, 2001; Innes et al., 2004), of which especially Freestone (2004) and Freestone (2010) (a report on the underlying principles and a MS-DOS user manual) have proven insightful. Unless indicated otherwise, the information in the remainder of this section is based on these two references.

Flow model

Although VGK was developed for viscous analysis, it also contains an inviscid module. Both, together with their coupling, are treated in the next sections. As the flow is modelled using the full potential

equation (assuming irrotational flow), the program is limited to small shocks. According to [Freestone \(2004\)](#), the results are valid for flows in which the Mach number just before the shock wave is lower than 1.3, a number also identified by [Holst \(2000\)](#) as a limiting value for potential theory. Any shocks are assumed to be isentropic.

Inviscid formulation

As VGK solves the full (non-linearised) potential equation, there are no elemental flows from which the inviscid flowfield can be made up. Instead, the full potential equation is simply solved on the grid, discussed later in this section. In order to fix the solution, a boundary condition is set that enforces a non-zero normal velocity at the inviscid surface, to allow for the growth of the boundary layer. Also, a jump in velocity is set across the streamline dividing the viscous and inviscid regions.

Viscous formulation

In the viscous formulation, five boundary layer parameters are computed. These are the boundary-layer thicknesses δ (thickness, only in case of a turbulent boundary layer), δ^* (displacement thickness) and θ (momentum thickness), the transformed boundary layer shape parameter \bar{H} and the local skin friction coefficient c_f . These values are found for both surfaces (upper and lower), as well as in the wake. The methods employed to find these parameters differ between the cases of laminar and turbulent flows.

The overall drag is determined from either a near-field or a far-field approach. The former method is based on summing the drag contributions from the surface pressures and the surface shear stresses, whereas the latter adds viscous and wave-drag contributions. The viscous drag coefficient is determined from the momentum thickness of the wake, the wave drag is calculated using either of two methods (the first-order method or the improved method), documented in [Lock \(1995\)](#). Normally, the far-field method is more accurate, due to the difficulty associated with accurately determining the surface pressure. However, for flows with significant wave drag, the wave drag determination might yield greater inaccuracies.

Laminar flow The laminar boundary layer is calculated using the method of [Thwaites \(1949\)](#), starting from the stagnation point, where the momentum thickness can be fixed. [Thwaites](#) focuses on an approximation of the skin friction and momentum or displacement thickness, rather than on the velocity distributions. Derivations can be found in [Moran \(1984, Sec. 7.5\)](#) or [Vos and Farokhi \(2015, Sec. 6.5.2\)](#), but the result of the method is Equation (4.9a), which can be related to a newly defined pressure gradient parameter in Equation (4.9b). This can then be used to compute the shear stress parameter and shape factor through empirical relations ([Vos and Farokhi, 2015](#)).

$$\theta = \sqrt{\frac{0.45\nu}{u_e^6} \int_0^x u_e^5 dx} \quad (4.9a)$$

$$\lambda = \frac{\theta^2}{\nu} \frac{du_e}{dx} \quad (4.9b)$$

This method is however an incompressible method. Using the Stewartson-Illingworth transformation ([Stewartson, 1949](#)), the real (compressible) problem can be transformed into an incompressible one, such that application of the aforementioned method is warranted – also if density cannot be assumed constant. This transformation itself, however, is only applicable to boundary layers that are thermally insulating, or in which the viscosity varies as the absolute temperature and the Prandtl number of the flow is unity ([Stewartson, 1949](#)). These limitations are therefore also applicable to problems analysed in VGK.

Turbulent flow The turbulent boundary layer is analysed in VGK using the ‘lag-entrainment’ method, which holds for two-dimensional, axisymmetric, adiabatic and compressible flow ([Green et al., 1977, 1973](#)). Entrainment is the process in which flow from outside the (turbulent) boundary layer moves inside the boundary layer – causing it to grow – due to turbulent mixing ([Head, 1958; Moran, 1984](#)). This method consists of solving three simultaneous (ordinary) differential equations: the momentum-integral

and entrainment equations are the same used in the method from which the current method was derived (Head, 1958); a new 'lag'-equation is derived from the turbulent kinetic energy equation (which, in turn, follows from the Navier-Stokes equations (Green et al., 1977)).

Transition There is no transition model incorporated in VGK. Instead, the transition location is user-specified on both surfaces. An exception to this is the situation in which laminar separation is predicted, based on the local skin-friction coefficient reducing below a threshold value of $2 \cdot 10^{-6}$. In that case, a transition to turbulent flow is assumed to occur at that point – if the flow was not already turbulent at this location due to a user-specified transition location upstream.

When the above threshold is reached, separation is also assumed, as true separation calculations are beyond the capabilities of the program. For separated flow, the local skin-friction coefficient is fixed at the threshold value, in order to allow the attached-flow boundary-layer calculation to continue to the trailing edge of the surface. If this happens, it is noted in the log file. The results should not be substantially impacted if this artificial skin-friction coefficient is set at only one or two grid points. (BVGK, which is a further development based on VGK, is able to deal with separation, as long as these regions are small.)

Wake The wake is formed by the extension of the upper and lower surface boundary layers, that join downstream from the trailing edge. A boundary condition prescribes a jump in velocity across the dividing streamline to allow for wake thickness and curvature. Rather than determining the exact location of the wake far downstream and calculating the relevant parameters at that location, VGK approximates these values by computing them at the grid line(s) running downstream from the trailing edge. This is based on the assumption made in the program that variations of Mach number and pressure along such a grid line correspond to these same variations along the wake. Contrary to in the boundary layer, the skin friction coefficient in the wake is 0.

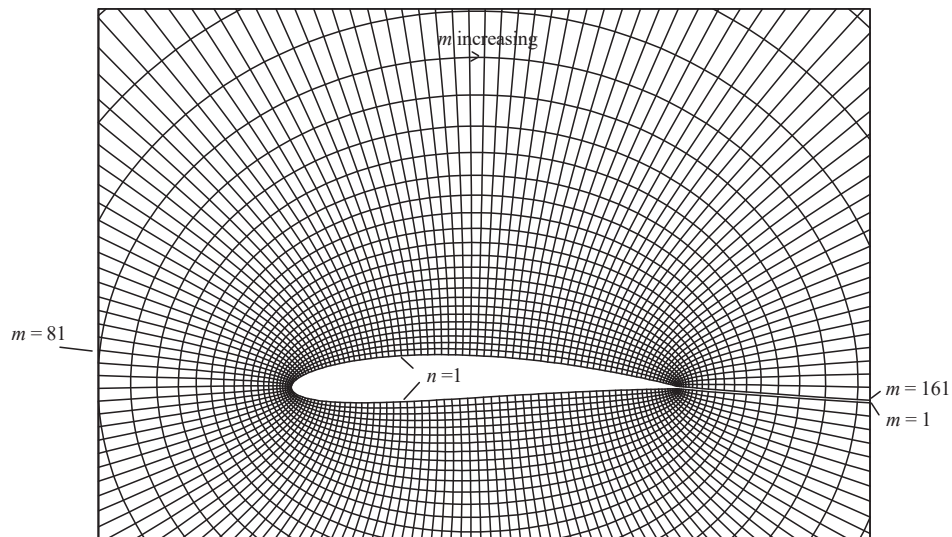
Viscous / inviscid coupling

VGK employs a so-called *direct method* of coupling the viscous and inviscid flow elements, as described in Lock and Williams (1987). Although its name might suggest otherwise, this viscous-inviscid interaction method too is an iterative procedure. It starts by estimating the source strength at a particular grid point, from which a velocity gradient can then be computed. This velocity gradient, in turn, is used to compute the development of the boundary layer, from which a boundary layer growth rate can be determined. This is then fed back to the inviscid computation, which is restarted. The scheme reaches convergence when the difference between the boundary layer interface location estimated by the two calculation methods (inviscid and viscous) is diminished.

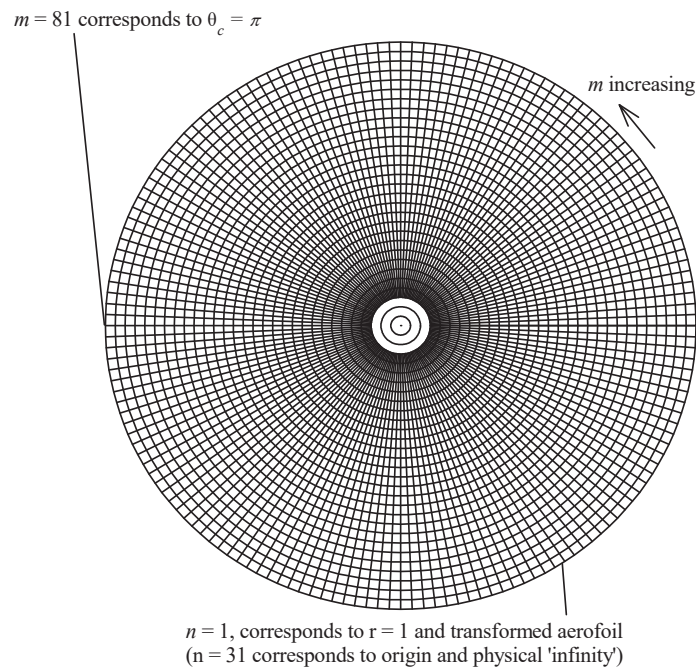
Solution procedure

Rather than taking a rectangular grid, VGK maps the infinite flow region outside the profile conformally onto the inside of a circle (Catherall et al., 1969; Blockley and Hodges, 1982). This mapping is not exact, as the grid points are an interpolation between the coordinates of the airfoil being analysed. Given enough grid points, the differences between the original geometry and the interpolation are small. Still, these differences might reduce accuracy of the boundary conditions at the airfoil surface. The number of grid points can be user-specified. Figure 4.3 shows the physical and computing planes, illustrating the conformal mapping.

The partially-conservative finite difference equations are solved using a relaxation method (Collyer and Lock, 1978). In each new iteration, the potential at the grid points is recalculated and compared with the previous value, until the difference is sufficiently small. The relaxation factor, which is a setting that can be adjusted by the user, controls the convergence rate. The flow solution is deemed converged when the grid differences (or residuals) are so small that further updates to the grid values do not substantially impact the value of the flow parameters in the solution. Central differencing is used in subsonic regions; backward differencing for supersonic part of the flow.



(a) Physical plane



(b) Computing plane (radial lines omitted near origin for clarity)

Figure 4.3: Physical and computing planes in VGK (Freestone, 2004, p. 7)

Output

The output of VGK is saved in binary files, as documented in Freestone (2010). Both a brief and a full version of the results are available. The brief version consists of a pressure distribution, lift, drag and moment coefficients for a specified angle of attack. In case the lift coefficient is fixed, the output includes the corresponding angle of attack. In the inviscid case, the drag coefficient is the pressure drag coefficient, whereas in the viscous formulation, the skin friction drag, the viscous drag coefficient (obtained using the far-field method discussed earlier) and the two wave drag coefficients are also included.

The full output adds to this the first- and second-order derivatives of the airfoil geometry (dz/dx and d^2z/dx^2), a set of coordinates in the physical and computing planes, the value of p/p_0 (local static pressure of freestream stagnation pressure) and the local Mach number at the edge of the boundary-

layer M_e . Besides these values on the airfoil surface, they are output for the wake – separately for the upper and lower surface. In viscous runs, VGK also saves upper and lower surface boundary layer data (shape factor, displacement thickness, momentum thickness, local skin-friction coefficient and, in case of a turbulent one, boundary layer thickness) to the full results file.

Results

Blockley and Hodges (1982, p. 7) described VGK as the “most accurate viscous transonic flow method currently available” and quote Ashill and Weeks (1978) reporting on good agreement between computational and experimental results. Although the method has been improved upon a number of times since then (Atkin and Gowree, 2012; Blockley and Hodges, 1982), results obtained using the original VGK method still have good accuracy, as long as the applicable flow type and domain (attached boundary layer, $M < 1.3$) are respected (Padulo et al., 2009; Freestone, 2004). Due to the viscous-inviscid interaction method, VGK is limited in accurately describing separated flow (i.e. the post-stall region) (Atkin and Gowree, 2012). The theory document itself (Freestone, 2004) supports these conclusions – both the accuracy at lower Mach numbers and the rising inaccuracy at higher speeds. Atkin and Gowree (2012) state the lag-entrainment method employed by VGK matches more advanced RANS turbulence models in describing the history effects in turbulent boundary layers and VGK even outperforms current (2012) RANS-codes in predicting the flows around the stagnation point.

Some results from the comparisons with experimental data are shown in Figure 4.4. In case of two drag computed drag values computed by VGK (corresponding to the first-order or the improved method), these have been averaged. Figure 4.4a shows incidence angle underpredicted at equal lift coefficient – equivalent to the overprediction of lift at constant incidence angle resulting from the Euler-comparison. Similarly, Figure 4.4b shows an underprediction of pitching moment coefficient and Figure 4.4c shows that drag coefficient is underpredicted too. These three graphs, all from the same set of experiments with largely comparable supercritical, 14% thick airfoils with forced transition at $0.05c$ show the errors reduce with increasing Reynolds number (dashed lines versus dotted lines). This can be explained by the fact that with increasing Reynolds number, flow separation is prevented or delayed. If the lift coefficient increases, the absolute deviation in incidence angle increases, whereas it decreases in a relative sense. Differences with respect to drag and moment coefficients are largely unaffected by lift coefficient or incident angle. In all cases shown in these figures, the strength of shock waves was slightly underpredicted, and their location somewhat aft. Other than that, pressure distribution predictions are in good agreement, with the exception of some airfoil parts facing rearward or trailing edge separation.

Figure 4.4d shows a different result: less consistent underprediction of c_d and an increasing error with higher c_l . This might be caused by the lower Reynolds number ($Re = 3 \cdot 10^6$) or the thinner (12.3% versus 14%) airfoil. Figures 4.4e and 4.4f show the difference in drag coefficient compared to that Boeing A4 supercritical airfoil, compared to lift coefficient and Mach number. Both generally indicate overprediction of drag, which seems to worsen with increasing c_l – especially at higher Mach numbers (Figure 4.4e).

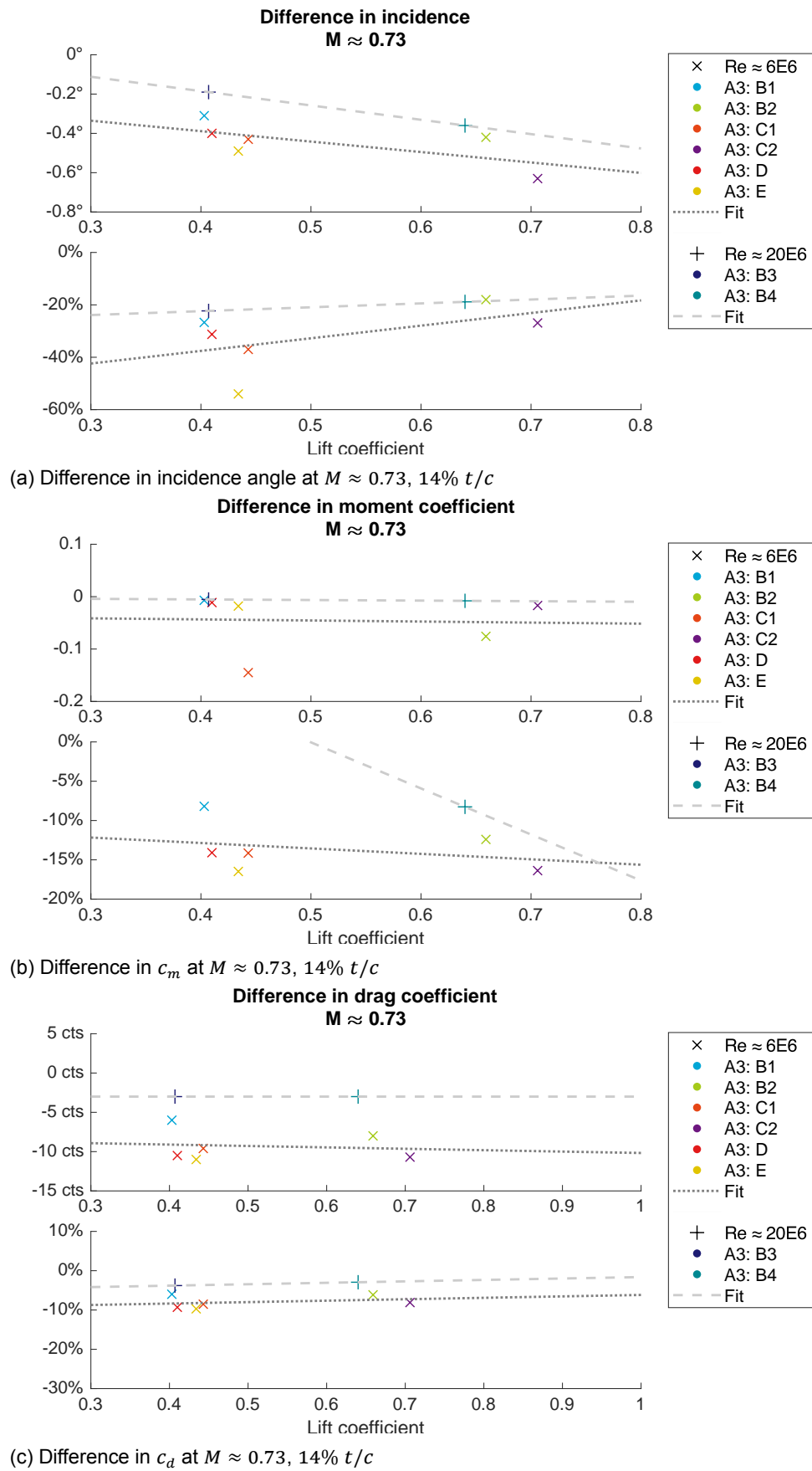
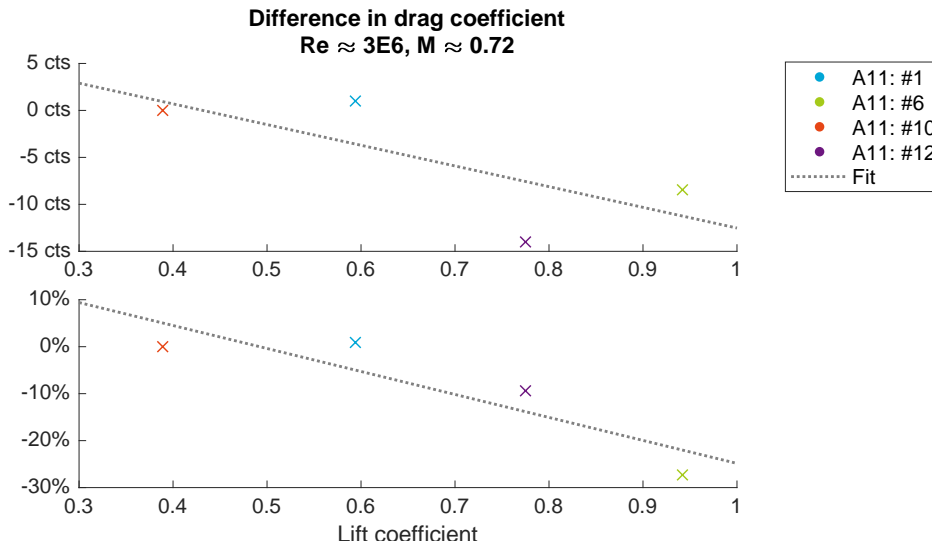
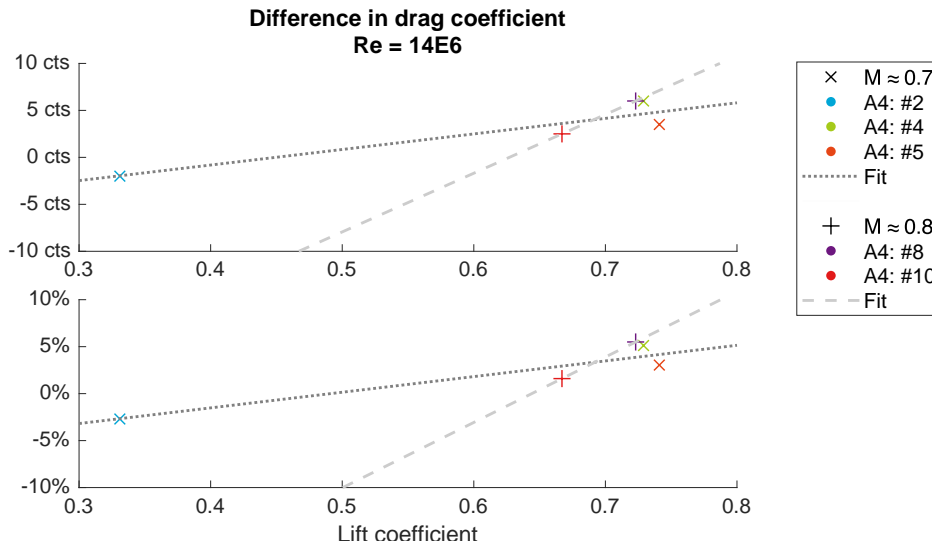


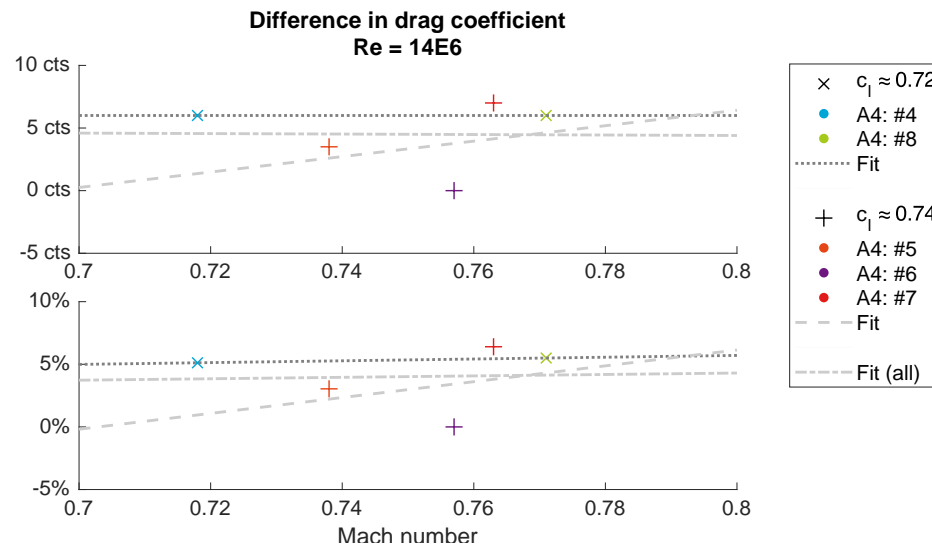
Figure 4.4: Comparison of incidence angle, moment coefficient and drag coefficient as predicted by VGK and found in experiment. Data computed from Freestone (2004, Sec. 6), experiment identifiers unchanged.



(d) Difference in c_d at $Re \approx 3 \cdot 10^6$, $M \approx 0.72$, 12.3% t/c



(e) Difference in c_d with M at $Re = 14 \cdot 10^6$, 10.2% t/c



(f) Difference in c_d with C_L at $Re = 14 \cdot 10^6$, 10.2% t/c

Figure 4.4: Comparison of incidence angle and drag coefficient as predicted by VGK and found in experiment. Data computed from Freestone (2004, Sec. 6), experiment identifiers unchanged. – continued

4.1.3. MSES

MSES ([Analytical Methods, 2018a](#); [MIT Technology Licensing Office, 2018](#); [Drela, 1994, 1990](#)) is a 2D airfoil design and analysis tool, available under a commercial licence and as an open source program for research purposes ([Florjancic, 2015](#)). The program is an updated version of the ISES code ([Greer et al., 2000](#)) and uses an Euler flow model, solved using a finite volume method, allowing it to perform computations at transonic Mach numbers so it can predict “transitional separation bubbles, shock waves, trailing edge and shock-induced separation” ([Drela, 1994, p. 1](#)). The code is built for the design and analysis of multi-element airfoils, but can also be used for single-element profiles. As XFOIL, MSES was developed by Mark Drela and Harold Youngren at MIT and has been around since at least 1994 ([Drela, 1994](#)), with methodological papers going back to 1990 ([Drela, 1990](#)).

A user manual to the current version (3.05) is available ([Drela, 2007](#)). Unless indicated otherwise, the information in the remainder of this section is based on that reference.

Flow model

The flow model closely follows the XFOIL code, described in Section 4.1.1, with the difference that MSES solves the Euler equations (Section 2.3) rather than using a potential method. It supports analysis using a Neumann boundary condition and design efforts using a Dirichlet boundary condition ([Drela, 1994](#); [Giles and Drela, 1987](#)). Far-field boundary conditions follow from the method of characteristics and allow for representing an airfoil in a wind-tunnel (solid wall) or freejet (constant pressure outer surfaces), or in isolation ([Drela, 1990](#); [Giles and Drela, 1987](#)).

Inviscid formulation

The software uses a finite-volume discretisation which is solved on an “intrinsic streamline grid” ([Drela, 1994, p. 1](#)). The conservative formulation makes sure that shocks are treated properly ([Giles and Drela, 1987](#)). The equations solved are the steady forms (i.e., partial derivatives with respect to t are zero) of Equation (2.4) (continuity equation), Equation (2.8) (momentum equation, without body forces, i.e. f_x, f_y and f_z equal to 0) and Equation (2.9) (energy equation) ([van Craenenbroeck, 2016](#)).

Viscous formulation

The model and computations used for describing the boundary layers and wake (two-equation integral formulation, based on dissipation closure) are very similar – if not partially identical – to the viscous formulation in XFOIL and ISES ([Drela and Youngren, 2001](#); [Drela and Giles, 1987a](#)). The flow solution in the viscous domain is obtained by solving Equations (4.2) (von Kármán momentum integral equation), (4.3) (kinetic energy shape parameter equation) and a rate equation depending on the flow domain ([van Craenenbroeck, 2016](#); [Merchant and Drela, 1996](#))⁶.

Laminar flow In laminar flow, the Falkner-Skan one-parameter profile family is used. This is further described in Section 4.1.1 and in even greater detail in [Drela \(1985, Sec. 6.2\)](#).

Turbulent flow In turbulent flow, the shear lag equation shown in Equation (4.10) is used ([van Craenenbroeck, 2016](#)).

$$\frac{\partial}{\partial \xi} \frac{dC_\tau}{d\xi} = 4.2 \left(\sqrt{C_{\tau EQ}} - \sqrt{C_\tau} \right) + \left(\frac{2\delta}{u_e} \frac{du_e}{d\xi} \right)_{eq} - \left(\frac{2\delta}{u_e} \frac{du_e}{d\xi} \right) \quad (4.10)$$

This seems a hybrid of the equations used in [Drela and Giles \(1987b, Eq. \(22\)\)](#) (used in XFOIL, Equation (4.6)) and the lag equation by [Green et al. \(1977, Eq. \(21\)\)](#). It adopts the shear lag constant (4.2) from [Drela and Giles \(1987b\)](#), but replaces the second right-hand term by the term found in [Green et al. \(1977\)](#).

⁶[Merchant and Drela \(1996, Eq. \(3\)\)](#) lack multiplication of $dH^*/d\xi$ with θ . Based on other references (e.g. [van Craenenbroeck \(2016\)](#) and [Drela and Giles \(1987b\)](#)) this is assumed to be a mistake.

Transition MSES uses the same envelope method for transition prediction as XFOIL and ISES (Coder et al., 2014; Drela, 2003; Lasauskas, 2005), described in Section 4.1.1. In version 3.00, the program was extended to include the full e^n -method for transition prediction (Drela, 2003), in contrast to XFOIL. However, as this was not “deemed reliable enough” (Drela, 2013), the solution is still obtained using the envelope method⁷ – with the full e^n method running in the background, so that the program is able to show what the individual frequencies would have been if the full e^n method was used (Lasauskas, 2005).

Viscous / inviscid coupling

The viscous-inviscid interaction is achieved via the displacement thickness (Drela, 1994; van Craenenbroeck, 2016). The wall boundary condition is adjusted to allow for this (Giles and Drela, 1987). The viscous and inviscid flows are solved simultaneously in one set of equations, circumventing the need for back-and-forth iteration (Florjancic, 2015).

Solution procedure

MSES uses a finite volume discretisation on a grid that conforms to the inviscid streamlines of the flow (themselves computed using a 2D panel method) (Florjancic, 2015). Grid spacing can be user-specified, but is smaller in regions of high curvature by default (Drela, 2007). The set of equations describing the flow is solved using the global Newton method, further described in van Craenenbroeck (2016) and Drela (1985).

Coefficients of pressure and friction forces in x and y direction are found using direct integration over the surface. Summation over all the elements then yields lift, skin friction drag and pitching moment. The total viscous drag is subsequently found by looking at the momentum defects in the wake, computed using Equation (4.11).

$$C_{D_v} = \frac{2}{\rho_\infty V_\infty^2} \sum \left[\rho_{e_{exit}} u_{e_{exit}}^2 \theta_{e_{exit}} \left(\frac{p_\infty}{p_{e_{exit}}} \right)^{H_{avg}/\gamma M_\infty^2} \right] \quad (4.11)$$

The elements with subscript $()_{e_{exit}}$ are the wake exit quantities. H_{avg} is the average shape factor, taking the average of the shape factors at the end of the wake ($H_{e_{exit}}$) and at the freestream (H_∞).

The wave drag is found as the momentum defect of the streamtubes in the part of the flow that is inviscid. To this, the static and dynamic pressure at the wake exit are isentropically extrapolated to find their values at free-stream conditions. Integration over all streamtubes (with a massflow $d\dot{m}$), as shown in Equation (4.12), yields the wave drag.

$$C_{D_w} = \frac{2}{\rho_\infty V_\infty^2} \int (V_\infty - q_{+\infty}) d\dot{m} \quad (4.12)$$

The total drag is the sum of the viscous drag given by Equation (4.11) and the wake drag by Equation (4.12). Subtraction of the skin friction drag (obtained from surface integration) then yields the pressure drag. This is deemed more accurate than finding the pressure drag directly from the surface pressures (Drela, 2007).

Output

As MSES was not available in the period this literature study was conducted, no information on the type and format of the output generated by the code is available at this time.

⁷The developer’s documentation, (Drela, 2013) in this case, is regarded as the leading source. Nevertheless, some authors (e.g. Driver and Zingg (2007), Maughmer and Coder (2010) and Coder et al. (2014)) report using MSES with the full e^n method.

Results

Although possibly not as popular and widely used as XFOIL, MSES is a widely accepted (Chaparro et al., 2017) and described as an “excellent tool for the development of single and multi-element airfoil geometries” (Martin and Simpson, 2006, p. 374). Citing Rumsey and Slotnick (2014), Florjancic (2015) reports that higher-fidelity codes do not necessarily yield better $c_{l,max}$ -predictions. Published results show mixed support for this claim. When compared to CFL3D (2D RANS with S-A turbulence model) and OVERFLOW (3D RANS), some note excellent agreement in terms of predicted pressure distributions (Fujiwara et al., 2016) and (the linear part of) the lift slope (Coder et al., 2014). On the other hand, Leifsson et al. (2014) did find differences between MSES and FLUENT (10 drag counts lower in MSES; 5 lift counts higher in MSES). Greer et al. (2000) report a 26% difference in computed lift coefficient between MSES and a time-accurate laminar Navier-Stokes analysis (Tatinen and Zhong, 1998).

Comparing with experimental data, Fujiwara et al. (2016) observed little difference between theory and experiment, with the exception of a slightly underpredicted shock strength and slightly forward expected shock location. Coder et al. (2014) report an overprediction of lift (c_l , α -curve, $c_{l,\alpha=0}$ and $c_{l,max}$), increasing at higher Reynolds numbers, as do Maughmer and Coder (2010). In these and other studies, c_m is often slightly underpredicted (independent of Re), and c_d is mostly underpredicted, too (Florjancic, 2015; Omar et al., 1973; Syms, 2006). Coiro et al. (2009) also note a tendency of MSES to over-estimate lift performance in cases of larger gaps between parts of a multi-element airfoil. The overly optimistic c_l -values might be explained by the simplified e^n -envelope transition model (Syms, 2006; Lasauskas, 2005).

4.1.4. Ames Research Center 2D (ARC2D)

ARC2D (short for *Ames Research Center 2D*) (National Aeronautics and Space Administration) and its 3D counterpart ARC3D are two high-fidelity aerodynamic solvers developed by NASA (Ames Research Center) in the 1980s (Pulliam, 1984, 1986). The software is based on AIR2D, which was developed by Steger in 1976 (Pulliam, 1986). The program is suited for both viscous (using Navier-Stokes) and inviscid (using Euler) as well as steady and unsteady problems (Pulliam, 1986). The flow models are solved with a finite difference method using the implicit approximation algorithm of Beam and Warming (1976). Since its inception, the code has seen various upgrades (Pulliam and Steger, 1985; Pulliam, 1986) and has more recently been used as a basis for the CFD solver OVERFLOW, also developed by NASA (Cummings et al., 2015).

A user manual nor a current version number or program could be obtained, but Pulliam (1986) provides an description of the theoretical foundations of an early version of the software. It is however unknown to what extent this still holds for current versions of the program. Still, lacking any other means, the information in this section is based on the aforementioned reference, unless indicated otherwise.

Flow model

Most literature discussing ARC2D state its basis is formed by a RANS solver (McCroskey et al., 1986; Guzel et al., 2005; Yoo et al., 1990). Pulliam (1986) however does not make this explicit and shows a derivation of the flow model used in ARC2D based on the time-dependent NS equations, without time-averaging these. Similarly, Yoo et al. (1990) and Pulliam and Vastano (1993) discuss using the “full” Navier-Stokes code. Still, as turbulence models are discussed, it will be assumed that ARC2D is RANS-based. Another point of confusion arose where most publications mention the thin-layer approximation made in the code (Pulliam, 1986; McCroskey et al., 1986; Yoo et al., 1990). McCroskey et al. (1986) and Pulliam (1986), however, also mention an Euler implementation (obtained by neglecting viscous terms in the RANS equations, without making the thin-layer approximation), whereas Yoo et al. (1990) and Pulliam (1986) discuss a regular (without thin-layer approximation) Navier-Stokes option as well.

Besides steady problems, time accurate methods can be employed to solve transient problems (Pulliam, 1986, p. 14), not unlike the possibilities offered by URANS (Section 2.1.3). In order to capture shocks accurately, the software uses the strong conservation form of these equations. This is shown in Equation (4.13):

$$\frac{\partial}{\partial t} \mathbf{Q} + \frac{\partial}{\partial x} \mathbf{E} + \frac{\partial}{\partial y} \mathbf{F} = Re^{-1} \left(\frac{\partial}{\partial x} \mathbf{E}_v + \frac{\partial}{\partial y} \mathbf{F}_v \right) \quad (4.13)$$

In this equation, the vectors \mathbf{Q} (state variables), \mathbf{E} , \mathbf{F} , \mathbf{E}_v and \mathbf{F}_v are defined as shown in Equation (4.14):

$$\mathbf{Q} = \begin{pmatrix} \rho \\ \rho u \\ \rho v \\ e \end{pmatrix}, \quad \mathbf{E} = \begin{pmatrix} \rho u \\ \rho u^2 + p \\ \rho uv \\ u(e+p) \end{pmatrix}, \quad \mathbf{F} = \begin{pmatrix} \rho v \\ \rho uv \\ \rho v^2 + p \\ v(e+p) \end{pmatrix}, \quad (4.14)$$

$$\mathbf{E}_v = \begin{pmatrix} \cdot \\ \tau_{xx} \\ \tau_{xy} \\ u\tau_{xx} + v\tau_{xy} + \mu Pr^{-1} (\gamma - 1)^{-1} \frac{\partial a^2}{\partial x} \end{pmatrix}, \quad \mathbf{F}_v = \begin{pmatrix} \cdot \\ \tau_{xy} \\ \tau_{yy} \\ u\tau_{xy} + v\tau_{yy} + \mu Pr^{-1} (\gamma - 1)^{-1} \frac{\partial a^2}{\partial y} \end{pmatrix}$$

The first row forms the continuity equation, the second and the third the momentum equation in x - and y -direction and the last one the energy equation. Besides the regular variables density, pressure, velocities, internal energy, and shear stresses, they include the dynamic viscosity μ (comprised of a constant viscosity and a turbulent eddy viscosity), the Prandtl number Pr , the ratio of specific heats γ and the speed of sound a . The fact that these equations (especially the right-hand side) cannot be readily rewritten to the (two-dimensional versions) of Equations (2.1), (2.4) and (2.5) (neglecting kinetic energy and body forces) presented in Section 2.1 is explained by non-dimensionalisation performed by Pulliam (1986, pp. 6-7) and the equation of state shown in Equation (4.15), relating density and pressure:

$$p = (\gamma - 1) \left(e - \frac{1}{2} \rho (u^2 + v^2) \right) \quad (4.15)$$

As a next step, the above equations in Cartesian coordinates are transformed to a curvilinear coordinate system, with one axis parallel (ξ) and one axis perpendicular (η) to the body surface, as shown in (the left side of) Figure 4.5 (Pulliam and Steger, 1985; Pulliam, 1986, 1993). This makes it very easy to apply the thin-layer approximation, by simply neglecting viscous terms with ξ -derivatives.

Inviscid formulation

The inviscid formulation is obtained by neglecting all viscous terms in the Navier-Stokes equations, yielding the Euler equations. In the set of equations presented earlier, this is achieved by setting $\mathbf{E}_v = \mathbf{F}_v = 0$.

Viscous formulation

The viscous formulation uses the complete set of equations presented in Equations (4.13) and (4.14). It supports both laminar and turbulent flow (McCroskey et al., 1986).

Laminar flow In case of laminar flow, the turbulent eddy viscosity contained in the dynamic viscosity μ (in the energy equation of Equation (4.13)) is set to 0.

Turbulent flow When turbulent flow is modelled, a turbulence model is used to find a value for the turbulent eddy viscosity, that is part of the dynamic viscosity μ contained in the partial differential equation describing the flow.

In Pulliam (1986), the turbulence model by Baldwin and Lomax (1978) gets most attention. It was specifically developed for use with the TLNS equations and has as an advantage that it “eliminates the need for

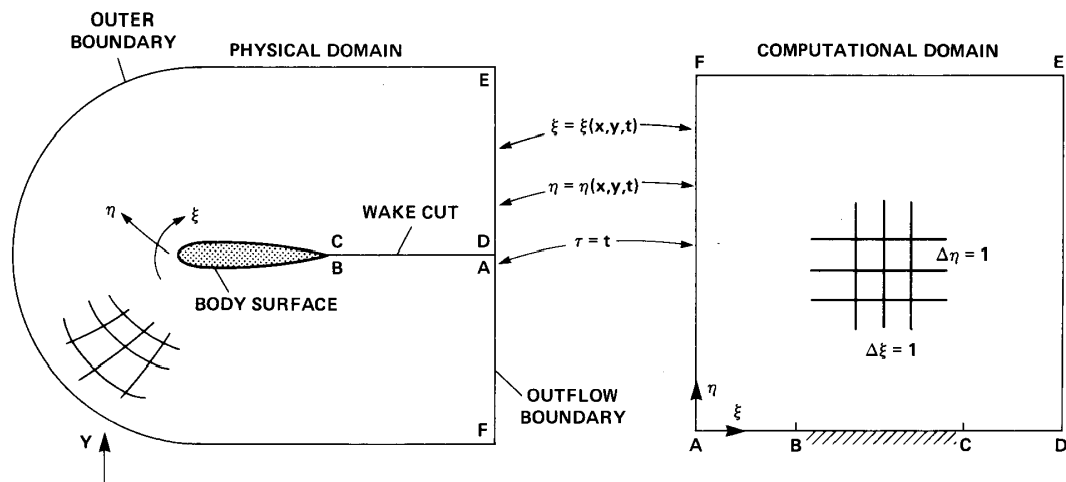


Figure 4.5: Coordinate transformation in ARC2D (Pulliam and Steger, 1985; Pulliam, 1986, 1993, p. 15, 8, 693)

finding the edge of the boundary layer and thus remove one of the sources of arbitrariness and potential error” (Baldwin and Lomax, 1978, p. 7). In addition, the Baldwin-Barth turbulence model (one-equation, based on the $k - \epsilon$ model) (Baldwin and Barth, 1991), several variations of the Spalart-Allmaras (S-A) model (Spalart and Allmaras, 1992) and a wide variety of two-equation models are supported (Pulliam, 1986; Mayda and van Dam, 2005).

Transition Although ARC2D supports both laminar and turbulent flow, transition modelling is not included in the software. Transition locations hence have to be specified by the user (McCroskey et al., 1986).

Viscous / inviscid coupling

No viscous / inviscid coupling seems to be required by ARC2D (Pulliam and Steger, 1978). However, in at least one study, researcher have used the program in conjunction with an inviscid solver (Mouch and Lan, 1993).

Solution procedure

In Pulliam (1986), most attention is paid to the numerical algorithm used by ARC2D. It is an “implicit approximate factorization finite difference scheme” (Pulliam, 1986, p. 15), which can be first or second-order accurate in time, based on the work by Beam and Warming (1976). Central order finite differences are used to find the derivatives in space (Pulliam, 1986; Venkateswaran et al., 2003). Nonlinear stability is obtained using explicit and implicit artificial dissipation terms. In case of steady-state calculations, the algorithm is sped up using a time step that can vary with space. In case time-accurate solutions are required (for unsteady or transient problems), a second-order accurate dual time-stepping algorithm is used (Pulliam, 1993; Mayda and van Dam, 2005). In a later development effort, further detailed and quantified by Pulliam and Steger (1985), a number of improvements to the algorithm originally implemented in ARC2D was made. Changes include incorporating of a mesh refinement sequence (so that an approximate solution can first be obtained on a coarser grid, then interpolated to a finer grid and subsequently refined), a reduction of (computationally expensive) matrix inversion work and improvements to robustness. These all increase convergence rates, reducing computational cost. Mayda and van Dam (2005) note in general the program is optimised for computational efficiency. The structured grids allow the program to make use of parallel processing ability, as is found in CRAY supercomputers.

The flow equations are solved on a structured grid using either a C- or O-topology (Guzel et al., 2005; Mayda and van Dam, 2005). Low Mach-number preconditioning improves the quality of low speed flows solved using the compressible equations incorporated in ARC2D (Mayda and van Dam, 2005), although this also seems to negatively impact robustness of the solver (Venkateswaran et al., 2003).

Output

As ARC2D was not available in the period this literature study was conducted, no information on the type and format of the output generated by the code is available at this time.

Results

Pulliam (1986) himself already summarised a number of validity studies, comprising a number of different types of airfoils as well as inlets (Chaussee and Pulliam, 1980), cascades (Steger and Pulliam, 1980) and cylinders (Pulliam and Steger, 1980). Limiting the present discussion to airfoils, various authors note generally good prediction of pressure coefficient curves (Pulliam, 1986; Lall et al., 1995). Most problems there are found at the leading edge, where the suction peak is sometimes overpredicted (Maksymiuk and Pulliam, 1987; Guzel et al., 2005), and in shock regions. Shock locations are sometimes predicted too far forward or too far back (Maksymiuk and Pulliam, 1987), or overexpansion is expected but not seen in experimental results (Kaul and Nguyen, 2014; Harris, 1981). Separation is a third phenomenon with which ARC2D has some difficulties, most notably (as is often the case) near or at the trailing edge (Steger, 1977; Maksymiuk and Pulliam, 1987).

This obviously also has an impact on lift prediction. Most publications comparing ARC2D to other codes or experimental results describe close to very close agreement in the linear part of the lift curve (Barth et al., 1985; Maksymiuk and Pulliam, 1987; Guzel et al., 2005; Pulliam et al., 1986; Mouch and Lan, 1993; Mayda and van Dam, 2005), sometimes outperforming more recent solvers such as OVERFLOW (Kaul and Nguyen, 2014), as shown in Figure 4.6. If discrepancies arise, they mostly concern an overprediction of lift (Mayda and van Dam, 2005; Yoo et al., 1990; Pulliam, 1986). McCroskey et al. (1986, p. 9), comparing numerical data with a host of experimental results, goes as far as concluding that the “numerical results presented in this paper [obtained using ARC2D] are as accurate as contemporary experimental measurements”. However, predicting stall and post-stall (lift) characteristics is more troublesome (Guzel et al., 2005; Yoo et al., 1990; Mayda and van Dam, 2005). In various experiments by Guzel et al. (2005), maximum lift coefficient predictions are still reasonably accurate, but are predicted at a higher angle of attack than measured. Also, lift is expected to decrease more gradually than seen in experiments. Pulliam et al. (1986), as well as Maksymiuk and Pulliam (1987), Mouch and Lan (1993), Mayda and van Dam (2005), relate this to the turbulence model (often Baldwin-Lomax).

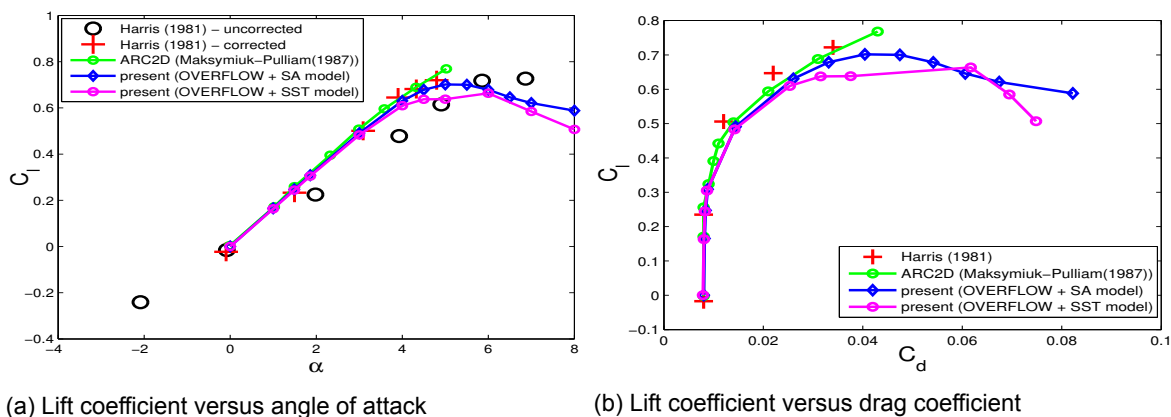


Figure 4.6: Comparison of experimental and numerical results for a NACA0012 airfoil, illustrating ARC2D performance (Kaul and Nguyen, 2014, pp. 10–11). Kaul and Nguyen (2014) state these results are from a NACA0021 airfoil, but as both Harris (1981) and Maksymiuk and Pulliam (1987) have used a NACA0012 airfoil, it is assumed that the 0021-designation in Kaul and Nguyen (2014) is erroneous.

Just as with lift, Kaul and Nguyen (2014) (as well as Potapczuk (1988) in comparison to Bragg et al. (1985)) mostly note good agreement between experimental and simulated drag polars. Most other studies reviewed that compare drag values, however, signify overprediction (Pulliam, 1986; Mouch and Lan, 1993) – sometimes up to an almost constant offset of 20 to 25 counts (Yoo et al., 1990). As with most solvers, accurate moment predictions are most difficult, as there is no ‘easy’ linear range. The trends are mostly captured quite well (Potapczuk, 1988), but offsets are sometimes observed (Mouch and Lan, 1993; Guzel et al., 2005; Yoo et al., 1990).

An interesting study by [Mayda and van Dam \(2005\)](#) has compared performance of the code to a host of experimental results of a SC1095 helicopter blade section ([Bousman, 2003](#)), especially in terms of dependence of Mach number. The large amount of experimental data is scattered and make direct comparisons somewhat more difficult, but the computed relations between Mach number and lift curve slope, zero lift drag coefficient and pitching moment coefficient fit well. A negative spike in the pitching moment curve slope at zero lift is captured by ARC2D, both coupled to the S-A as well as the Baldwin-Barth turbulence models, although the value of the spike is predicted by both models as more dramatic than it was measured. Drag divergence is especially well predicted (within one standard deviation of the experimental mean), as well as the lower part of the drag polar. A study into the behaviour of turbulence models specifically (Cebeci-Smith and Johnson-King) by [Lall et al. \(1995\)](#) showed good agreement in terms of pressure distribution, but noted some discrepancies in predicted skin friction coefficient at the first 30% of the airfoil chord.

4.1.5. Comparative review

Even though the four solvers discussed in this section all are two-dimensional and include viscous effects in their flow predictions, there are some important differences. Most prominent is the Mach regime. Whereas XFOIL is strictly limited to subsonic flows (preferably incompressible, otherwise approximated using a compressibility correction), VGK is able to handle some small shocks (as long as $M < 1.3$ just upstream, using a compressible-to-incompressible transformation) and MSES is specifically designed for transonic flow. ARC2D on the other hand has most problems with low speed ($M < 0.3$) flows, but is not limited on the higher end of the Mach scale. With respect to suitability for analysis of multi-element airfoils, VGK also forms a middle ground between XFOIL (not supported) and MSES (fully supported) in allowing control surface deflection. Although no research publications were found in which ARC2D was used for a multi-element airfoil, the flow model used in the code makes no assumptions invalidating that use. A clear distinction between the two codes by Drela (XFOIL and MSES) and VGK and ARC2D is found in terms of support for inverse design, for which VGK and ARC2D are not equipped. Similarly, XFOIL and MSES are targeted specifically at low Reynolds numbers applications – although in the range between 1 and 5 million, all solvers have been used.

In terms of solution method, the four codes are all different. XFOIL uses a 2D panel method, using flat panels, and hence requires a sufficient amount of panels to properly represent the airfoil shape. VGK takes a finite difference approach on a circular grid. Again, airfoil representation is not absolute, as the program defines grid points based on an interpolation of profile coordinates. MSES, an Euler code, uses a finite volume discretisation on a grid based on the inviscid streamlines. ARC2D solves the flow model using a finite difference method on a structured body-conformal grid.

A more detailed look at the flow model highlights some important differences between the capabilities of XFOIL and MSES on one hand, and VGK and ARC2D on the other. First of all, neither VGK nor ARC2D include a model predicting transition (from laminar to turbulent flow), but rely on the user to specify a transition point. VGK does not officially support separated flow. It is predicted based on a hard-coded value for local skin friction coefficient. When that value is obtained, turbulent flow is assumed from that point onward and the skin friction coefficient for the downstream part of the flow over the airfoil is set to the fixed value. Due to ARC2D using the thin-layer NS rather than the boundary layer equations, separation is supported. XFOIL and MSES employ an envelope version of the well-known e^n method to estimate a transition location, with the difference that MSES also computes the result of the complete e^n method for validation purposes and XFOIL does not. In describing the boundary layer, VGK uses the method of [Thwaites \(1949\)](#) for the laminar part and a lag-entrainment method by [Green et al. \(1973\)](#) for the turbulent flow domain. XFOIL and MSES use very similar methods for both laminar and turbulent flow, using straight-line approximations to the Falkner-Skan one-parameter profile as closure relations in the laminar part of the boundary layer, and two slightly different (Equations (4.6) and (4.10)) shear-lag equations in the turbulent domain. To couple the viscous and inviscid domain, all boundary layer solvers use a viscous-inviscid interaction method. In Euler-mode, ARC2D only performs an inviscid analysis, but if the RANS equations are selected, the domain is simulated as fully viscous – preventing the need for a VII method.

The output presented by XFOIL and VGK solvers is comparable, showing pressure distributions and lift, drag and moment coefficients. XFOIL adds to this transition locations and some plotting capability, VGK boundary layer information (edge Mach number, thicknesses and skin friction coefficients) and coordinates of the physical and computational planes. A comparison with MSES and ARC2D could not be made at this time, due to unavailability of the code.

Compared to higher-order methods and experimental results, none of the programs perform especially poorly, but contrasts can nonetheless be observed. XFOIL generally overpredicts lift coefficient and underpredicts drag coefficient, especially at higher angles of attack where separation occurs. In the linear range of the lift polar, good agreement is observed. That is also the case for ARC2D and VGK. Although that latter program too suffers from overprediction of lift and underprediction of drag (ARC2D generally overpredicts drag), especially the errors in drag prediction are on average lower than the discrepancies between XFOIL and experimental results. MSES is again very comparable to XFOIL, possibly even slightly less accurate in solving problems for which both codes are applicable (i.e., single-element airfoils at low Mach numbers) (Maughmer and Coder, 2010). Lift is over- and drag is underpredicted. For MSES, Syms (2006) argues the overprediction of lift coefficient is related to the simplified e^n model. As that is shared between MSES and XFOIL, this might also explain the deviations observed in that latter code. Ramanujam et al. (2016) explain the too low drag and too high lift coefficients by the viscous / inviscid interaction method, which becomes more problematic with increasing profile thickness. In the analysis of ARC2D, various authors blame the turbulence model for the discrepancies between predicted and measured aerodynamic coefficients. An interesting contrast is observed in the fact that larger Reynolds numbers decrease the error in case of VGK, but yield larger differences in case of XFOIL and MSES. It is hypothesised that the explicit focus of these latter methods on lower Reynolds number flows might come at the cost of somewhat reduced performance at higher Reynolds numbers. ARC2D was not analysed in this regard. VGK and MSES share the fact that shocks strengths are computed to be slightly lower than measured in experiments. VGK predicts the shock location a bit aft, and in contradiction, MSES predicts it slightly in front of the true location. ARC2D holds the middle ground, with some reports of shocks estimated too far aft, and other cases in which they are computed too far forward.

XFOIL, VGK and MSES are all command-line tools (FORTRAN or MS-DOS) and are equally easy (or difficult) to use. Between XFOIL and MSES, there is a lot of overlap and similarity, owing to the shared developer. The precise workings of either code are scattered over a host of publications (not all of them formatted very well) and information is sometimes contradictory⁷. This can also be said for ARC2D. In contrast, documentation for VGK is an extensive set of well-referenced reports, often including numerous validation cases. By this, it seems that XFOIL and MSES have seen longer periods of intermittent and not overly coordinated development, whereas VGK feels more complete.

4.2. Three-dimensional solvers

This section discusses three-dimensional solvers. They model a complete wing and/or aircraft body and as such address topics as lift distribution, tip vortices and stability and control derivatives. Compared to two-dimensional solvers, effects such as spanwise flow and various three-dimensional transition triggers (cross-flow, attachment-line and centrifugal instability) further complicate the flow models (Vos and Farokhi, 2015). Contrary to the two-dimensional codes treated in Section 4.1, all but one of the 3D solvers discussed here serve a pure analytical purpose and do not offer design capabilities.

In the next few sections, the programs AVL (Section 4.2.1), Tornado (Section 4.2.2), VSAERO (Section 4.2.3), MATRICS and MATRICS-V (Section 4.2.4) and SU2 (Section 4.2.5) are treated in further detail. Section 4.2.6 provides a comparative review of these solvers.

4.2.1. Athena Vortex Lattice (AVL)

The Athena Vortex Lattice method (AVL⁸) is a VLM originally developed in 1988 by MIT's Mark Drela and Harold Youngren (Drela and Youngren, 2017), based on codes developed for NASA (e.g. Lamar (1976) and Miranda et al. (1977)) (Drela and Youngren, 2010). The current major release (v3) stems from 2002 and can be considered a completely new version with little traces to aforementioned classic codes (Drela and Youngren, 2017, 2010). Literature describes AVL as an "extended" vortex lattice method (Jagdale et al., 2009; Raghunath et al., 2014), designed for low Reynolds number flows (Thomas and Richardson, 2012). Indeed, the program goes beyond the classical VLM realm in providing the capability of modelling slender bodies using a combination of a source and a doublet filament – the *slender-body* method (Rose et al., 2012; Katz and Plotkin, 1991) – although experience with this is limited and users should proceed with caution (Drela and Youngren, 2010). Also, AVL supports control surfaces and deflections, including the option of having more than one at a particular wing section (e.g. a combination of a flap and an aileron). Flexible surface control surfaces can be implemented too, with the deflection being linearly interpolated between two points where it is specified.

A user manual to the current version (3.30) is available (Drela and Youngren, 2010). Unless indicated otherwise, the information in the remainder of this section is based on that reference.

Flow model

As any VLM, AVL is an inviscid method. It assumes quasi-steady flow, therefore neglecting unsteady vorticity shedding. Also, small angles of attack and sideslip (roughly 15° (Thomas and Richardson, 2012)) are assumed (Dantsker and Vahora, 2018). Compressibility is taken into account using the Prandtl-Glauert correction ($\sqrt{1 - M_\infty^2}$), deemed valid up to a wing-perpendicular Mach number of 0.6. Furthermore, AVL assumes thin airfoils and an associated lift slope of 2π – unless specified otherwise by the user, e.g. using values obtained from wind tunnel test or viscous foil calculations. Similarly, each section can be assigned a c_l/c_d -polar, by defining the lift and drag coefficients at the point just before the drag rise due to negative or positive stall, and at minimum drag (Drela and Youngren, 2017, `cdc1.f`). AVL then connects these points with two parabolic curves (Drela and Youngren, 2010). The downstream legs of the horseshoe vortices extend parallel to the x -axis, regardless of possible sideslip. Drag can be predicted using surface force integration or a far-field Trefftz-plane analysis. In terms of boundary conditions, flow tangency is enforced on the airfoil camber line (Drela and Youngren, 2010) and zero mass flux through both the airfoil, wake and possible body surface (Miranda et al., 1977).

Solution procedure

As with other discretised methods, the panelling has a substantial influence on the quality of the computational result. AVL allows for defining the number of panels in spanwise, chordwise and lengthwise (along the body-axis) direction, in a equidistant or (co)sine-spacing. Combinations thereof are also possible,

⁸Not to be confused with CFD and other simulation tools developed by the Austrian company of the same name (AVL LIST GmbH, 2018).

but by default, cosine spacings are used for spanwise and chordwise panel distributions. This results in tighter spacing at the leading and trailing edges of a wing and at the wing tips.

Output

Output control for AVL is very similar to XFOIL. Output can be shown on screen or written to file or, in some cases, shown in graphical format. It first of all consists of forces acting on the individual surfaces, strips or vortex panels. Each panel is specified in terms of its index and location in the x, y, z -plane and a number of geometric parameters (such as average chord) are given. Additionally, the output file contains the contributions to aerodynamic coefficients by the considered panel. Moving to the strips (a set of panels between the leading and trailing edge), AVL saves chord length, surface area, local incidence angle, local lift ($c \cdot c_l$), location of the centre of pressure and the well-known aerodynamic characteristics. Another command sums these forces for an entire surface (such as a half-wing or vertical stabiliser) and their contributions to aerodynamic quantities of interest: lift, drag (user-specified viscous, induced, and total), side-force and moment (roll, pitch and yaw) coefficients. A total force output file yields these quantities for the full aircraft. Two more output files show the stability derivatives and body-axis derivatives, including those corresponding to surface deflections.

Results

Although its not as popular as XFOIL, AVL too is a widely used program (Lee et al., 2017). Owing to its ability to compute stability derivatives, the program is often used to investigate flight dynamics (Rose et al., 2012; Lykins et al., 2011; Thomas and Richardson, 2012). Publications focus largely on smaller air vehicles, being either scale models (Thomas and Richardson, 2012) or UAVs or MAVs (Guo et al., 2011; Boschetti et al., 2010; Salichon and Tumer, 2013).

Abundant validation data, however, is unfortunately not easily found. This might be – at least to some extent – be explained by the fact that AVL is an inviscid method, whereas viscosity cannot be removed from (wind tunnel) experiments and these comparisons would therefore be unfair. Despite this difficulty, some experiments provide some details on the performance of AVL. Lykins et al. (2011, p. 6) compared eigenmode responses for a 1/3 scale acrobatic aircraft and noted the program provides “reasonable estimates” for parameters of interest. For the short period and Dutch roll AVL generally underpredicts the natural frequency (with error margins ranging from less than 1% to 32%) and underpredicts⁹ damping ratio (errors between 5% and 37%). The roll mode time constant is accurately predicted. Relatively good agreement was found in terms of lift and drag predictions, especially at smaller angles of attack (the design range of the program (Dantsker and Vahora, 2018)) and positive lift coefficients, but somewhat less so for pitching moment (Boschetti et al., 2010; Lee et al., 2017). Results are shown in Figure 4.7 (Boschetti et al., 2010). This might be explained by a lack of viscous effects in the AVL program (Dantsker and Vahora, 2018). Genco and Altman (2009, p. 11) concluded “good agreement” between theoretical computations and experimentally obtained induced drag coefficients for a boxwing plane at $Re = 1 \cdot 10^5$, Dantsker and Vahora (2018) have observed an underprediction of C_D . Finally, a comparison of AVL and Cart3D shows the aerodynamic influence matrices¹⁰ obtained by the two programs to be very similar (Gary and McDonald, 2014).

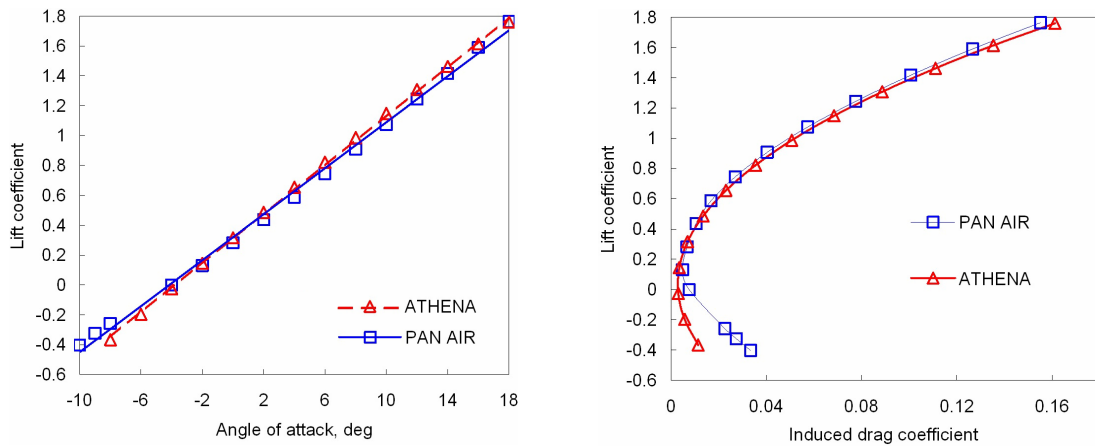
4.2.2. Tornado

Tornado (Melin and Berard) is a vortex lattice method built in MATLAB (The MathWorks, 2017), first presented in 2000 and released in 2001 (Melin, 2000, 2015a). The code was developed in a study investigating whether “it would be possible to code a vortex lattice method fast enough for real time application”¹¹ (Melin, 2000, p. 2), but has seen further development since with the current version released in 2010 (Melin, 2015a). The implementation is largely based on Moran (1984).

⁹Although the text describes overprediction, the values computed by AVL are in all cases lower than the ones obtained from flight tests.

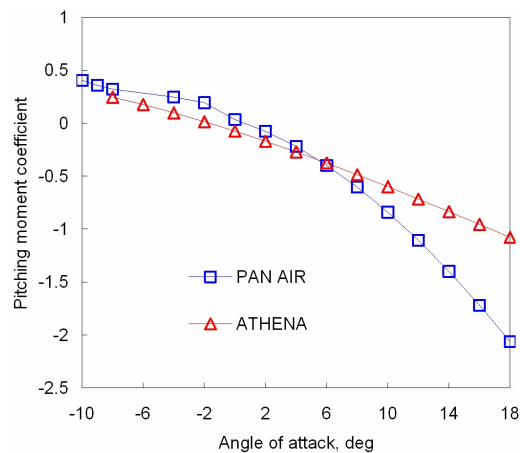
¹⁰“The AIC contains the partial derivatives of local sectional lift at M sections with respect to N basis function weights.” (Gary and McDonald, 2014, p. 2)

¹¹With “real time application”, the author meant application in an aircraft or flight simulator (Melin, 2000, pp. 2, 7).



(a) Lift coefficient versus angle of attack

(b) Lift coefficient versus induced drag coefficient



(c) Pitching moment versus angle of attack

Figure 4.7: Comparison of aerodynamic coefficients as predicted by AVL (labelled ATHENA) and PAN AIR (Boschetti et al., 2010, p. 7)

A user manual to the current version (135) is not available. A manual corresponding to the version of Tornado release in 2001, is currently labelled as “obsolete” (Melin, 2015b). As such, the remainder of this section is based on the original publication (Melin, 2000), unless indicated otherwise. It is however uncertain to what extent this information is still applicable to the current version of the program.

Flow model

Being a VLM, Tornado does not take viscous effects into account and is hence limited to the linear part of the lift curve. The code includes some experimental functions to generate a Trefftz-plane analysis and perform some viscous corrections. According to Ajaj et al. (2014, p. 1001), this includes a “semi-empirical component build-up method” by Cavallo (1966) used to estimate parasitic drag. A Prandtl-Glauert compressibility correction can be used to improve results at higher Mach numbers (Martindale et al., 2010).

Tornado furthermore assumes zero thickness of wings, although sweep, taper, dihedral and twist angles are supported (on each wing section, with the amount of sections being user-defined), as are control surface deflections and multiple wings (e.g. a main wing and an empennage). Although camber is supported, the boundary condition that allows for determining vortex strength is applied at the chord line. No flow perpendicular to the panel is allowed. Tornado deviates from Moran (1984) in modelling the wake such that it is aligned with the free-stream, rather than having it continue in chordwise direction, similar to Eppler (1997). This is allowed by using a system of vortex slings instead of horseshoe vortices

(Yerly, 2016; González R. et al., 2010; Cárdenas et al., 2009; Melin, 2000). These slings are made up of not one but three chordwise components (per side, yielding a total of seven instead of three vortex components), one for the main element, one for a possible control surface and one for the wake. A comparison is shown in Figure 4.8. The code uses a linear distribution of vortex strengths on each panel (Lee and Visser, 2016).

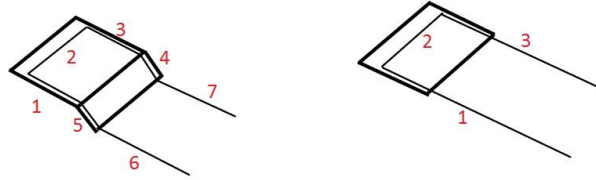


Figure 4.8: Comparison between a vortex sling as applied in Tornado (left) and a horseshoe vortex as applied in most other VLMs (right) (Yerly, 2016)

Improved codes exist that make it possible to model non-slender bodies and include viscous effects (Da Ronch et al., 2011, 2010).

Solution procedure

The solution procedure employed by Tornado is quite straightforward. During geometry input, one of various mesh options (linear, spanwise half-cosine, spanwise half-cosine and chordwise cosine, spanwise cosine, chordwise cosine, 3rd order centerpacking) can be selected. Following this, the influence of every vortex at every control point is computed, after which the flow tangency boundary condition is applied. Using Gaussian elimination, the vortex strengths are subsequently found. This is then used to calculate the vortex flow at each vortex' spanwise midpoint. Summing the vortex flow and the uniform free-stream flow yields the complete flow field. Forces are then found using the Kutta-Joukowski theorem.

Stability derivatives are computed using a central-difference approximation at the flight condition of interest. This is more accurate than the more common way, based on a parameter sweep.

Output

Tornado generates extensive graphical output, plotting local lift coefficient, span load, shear force, wing bending moment, local pressure difference and flow speeds, besides various geometry plots. In case of a parameter sweep analysis, the code outputs various polars (lift coefficient versus drag coefficient, angle of attack and moment coefficient) as well as the stability derivatives with respect to the chosen parameter.

The results of analyses of a single flight condition can also be exported to a text-file, showing force (lift, drag and normal, as well as x , y and z), and moment (pitch, yaw and roll) coefficients, and derivatives with respect to the angles of attack and sideslip, and pitch, roll and yaw rate. Control surface deflections and their effect on force and moment coefficients are also included. For all span stations, y -location, force per meter and local lift coefficient are saved to file, too. Results from a parameter sweep cannot be written to file, although computations can of course be saved to MATLAB-files.

Results

Similar to AVL, publications reporting on research conducted using Tornado often deal with smaller scale aircraft (González R. et al., 2010; Cárdenas et al., 2009). Many publications furthermore concern morphing structures or flexible aircraft, ideas gaining more and more attention (Yaman et al., 2015), such as span morphing (Ajaj et al., 2012, 2014; Xia et al., 2014) and active camber control (Yerly, 2016; Yerly et al., 2016; Martindale et al., 2010).

Only a few authors compare the results obtained with Tornado to higher-fidelity CFD computations or experimental data, although Melin (2000) included some validation results in the thesis describing the development of the VLM solver. This shows that, compared to Prandtl's lifting line theory, Tornado un-

derpredicts (5% to 10%) lift slope for flat plates with varying aspect ratios. Compared to AVL and CMARC (a panel method), computations for a Cessna 172 yield comparable results (Manzi, 1998), although differences (such as steeper lift and pitching moment slopes) are visible.

Errors in lift slope estimation are confirmed by Martindale et al. (2010) (1% error) and Yerly (2016), most notably at higher angles of attack. Due to the limitations of the Prandtl-Glauert compressibility correction, lift estimation accuracy also worsens in the transonic regime (Da Ronch et al., 2010). In the linear region, the lift slope matches well with higher fidelity codes (Da Ronch et al., 2010, 2011). Due to the lack of viscous effects, the stall angle cannot be accurately predicted. For this same reason, drag is underpredicted (Yerly, 2016; Martindale et al., 2010). (Yerly (2016) therefore also notes limited applicability of Tornado for low Reynolds numbers.) Including 2D viscous data notably improves these results (Yerly et al., 2016), as illustrated in Figure 4.9.

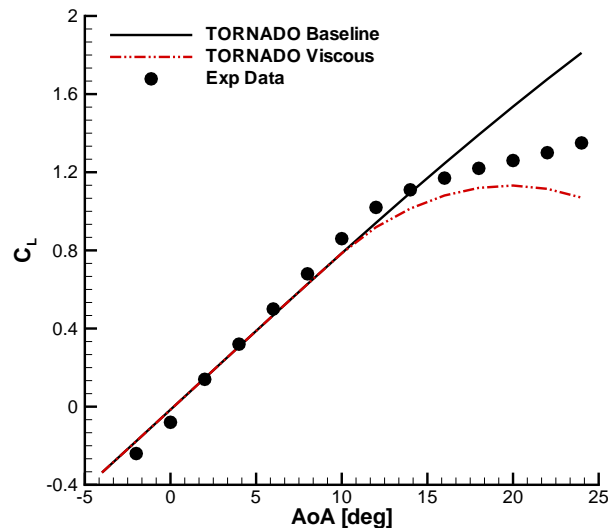


Figure 4.9: Comparison of lift coefficient variation with angle of attack as predicted (inviscid and viscous) by Tornado and found in experiment (Da Ronch et al., 2010, p. 10)

The accuracy of various stability and control derivatives or control surface effectiveness is of course also affected by inaccuracies in the estimation of the primary forces. Although the differences between various publications are too large to draw well-supported conclusions, authors report differences ranging from only a few percent to a few dozen (Martindale et al., 2010; Yerly, 2016; Da Ronch et al., 2010). The trends computed by the VLM are however generally accurate, such that various authors at least find Tornado suitable for trend analysis (Yerly, 2016; Yerly et al., 2016; Martindale et al., 2010) or accept the predictions made by the program “within certain error bounds” (Lee and Visser, 2016, p. 1).

4.2.3. Vortex Separation Aerodynamics (VSAERO)

VSAERO (Analytical Methods, 2018b; Analytical Methods), or *Vortex Separation Aerodynamics Program* in full (Ghaffari, 1988; Margason et al., 1985; Lednicer and Gilchrist, 1991) is a linear potential flow aerodynamic solver (Mariens, 2012; Strang et al., 1985; Nathman and McComas, 2008) that can be used to calculate “nonlinear aerodynamic characteristics of arbitrary configurations” (Maskew, 1987, p. 0). It combines an inviscid potential flow and a boundary layer model using a Morino-type panel method (Maskew, 1982b; Letcher Jr., 1989; Morino et al., 1975). It was originally developed in the 1980s for NASA by Analytical Methods, Inc., focusing on the analysis of high-lift configurations, but has since then been commercialised and seen wider applications (Lord and Zysman, 1986). Within NASA, VSAERO has been succeeded by PMARC (*Panel Method Ames Research Center*) (National Aeronautics and Space Administration, 1994).

A user manual to the current version is not available, but its original setup is relatively well documented in a user manual (Maskew, 1982b) and theory document (Maskew, 1987). It is unknown as to what

extent these documents still hold for newer versions of the program. Still, lacking any other means, the information in the remainder of this section is based on these references, unless indicated otherwise.

Flow model

The program uses quadrilateral panels and places doublet (representing changes in potential) and source (representing changes in normal velocity-component) singularities on these panels, with strengths constant on each panel. As such, it is a so-called *low order* method (Maskew, 1987; Lednicer and Gilchrist, 1991) in which the potential is piecewise smooth. (VSAERO v7.0 is a *multi-order* method (Nathman, 2005).) Various external Neumann boundary conditions, describing a solid boundary without wall transpiration ($V_N = 0$), a boundary layer using the transpiration technique (Dvorak et al., 1977b) or a steady surface (velocity along the surface $V_S = 0$), can be used to directly solve for the unknown source strengths; an internal Dirichlet boundary condition yields the doublet strengths. Planes of symmetry can be used to lower computational cost, as well as to analyse ground effect influences (Maskew, 1987; Ghaffari, 1988).

Using the Prandtl-Glauert transformation, VSAERO can be used for analysis of higher subsonic flows (Strang et al., 1985; Margason et al., 1985), suggesting using the critical Mach number as an upper limit (Lord and Zysman, 1986). Other sources mention a selection of compressibility corrections, of which the Karman-Tsien is the default (Lord and Zysman, 1986).

Inviscid formulation

In the code, it is assumed that viscous and rotational effects are solely present in the boundary layer, with the area outside that being modelled as inviscid as well as incompressible flow. The velocity potential is assumed to satisfy Laplace's equation (Maskew, 1987, p. 3)¹². Inside the cross-section being analysed, it is assumed that the potential (and velocity) are equal to the free-stream potential and velocity. This minimises the jumps from the inner to the outer flow, yielding lower singularity strengths, which makes the success and accuracy of a solution less dependent on large numbers of panels. Coming from Laplace's equation shown in Equation (2.19), the doublet density is solved by Equation (4.16):

$$4\pi\mu = \phi = \phi - \phi_\infty \quad (4.16)$$

The source distribution, then, is given by Equation (4.17):

$$4\pi\sigma = V_N - \mathbf{n} \cdot \mathbf{V}_\infty = \frac{\partial}{\partial S} (V_e \delta^*) + V_n - \mathbf{n} \cdot \mathbf{V}_\infty \quad (4.17)$$

The potential field is then described by Equation (4.18), yielding the description show in Equation (4.19) for the velocity field (obtained by taking the gradient from the potential field).

$$\phi_P = \iint_S \mu \mathbf{n} \cdot \nabla \left(\frac{1}{r} \right) dS + K\mu_P + \iint_S \frac{\sigma}{r} dS + \iint_W \mu_W \mathbf{n} \cdot \nabla \left(\frac{1}{r} \right) dW + \phi_{\infty P} \quad (4.18)$$

$$\mathbf{V}_P = - \iint_S \mu \nabla \left[\mathbf{n} \cdot \nabla \left(\frac{1}{r} \right) \right] dS - \iint_S \sigma \nabla \left(\frac{1}{r} \right) dS - \iint_W \mu_W \nabla \left[\mathbf{n} \cdot \nabla \left(\frac{1}{r} \right) \right] dW + \mathbf{V}_\infty \quad (4.19)$$

In these equations, the integrals over S are over the body surface; the integrals over W correspond to the wake. P indicates an arbitrary position in the flow field, dS the area of a panel and r the distance between these. \mathbf{n} is the normal vector (to dS) and K , finally, is a factor depending on the location of point P .

¹²Khalid et al. (1997) and Ghaffari (1988) also explicitly name Laplace's equation, the topic of Section 2.6, as the inviscid flow model. Strang et al. (1985, p. 2), on the other hand, discusses "the assumptions of small velocity perturbations", which corresponds to the linearised potential equation, discussed in Section 2.5.

For thin ($t/c < 0.01$) or “wing-like” surfaces that are “remote from the area of interest” (Maskew, 1987, p. 13), additional simplifications are made. These parts are represented as open surfaces, such that the source term σ disappears from Equation (4.18) to yield Equation (4.20), with $\mu = 1/(4\pi) (\phi_U - \phi_L)$ (i.e., the total jump in potential across the sheet):

$$\phi_P = \iint_S \mu \mathbf{n} \cdot \nabla \left(\frac{1}{r} \right) dS + \iint_W \mu_W \mathbf{n} \cdot \nabla \left(\frac{1}{r} \right) dW + \phi_{\infty P} \quad (4.20)$$

Similarly, Equation (4.19) reduces to Equation (4.21):

$$\mathbf{V}_P = - \iint_S \mu \nabla \left[\mathbf{n} \cdot \nabla \left(\frac{1}{r} \right) \right] dS - \iint_W \mu_W \nabla \left[\mathbf{n} \cdot \nabla \left(\frac{1}{r} \right) \right] dW + \mathbf{V}_\infty \quad (4.21)$$

Viscous formulation

For the boundary layer analysis, two methods are included. One gives characteristics of the boundary layer along computed surface streamlines (Dvorak et al., 1977a). This method can be applied to bodies and wings and covers surface curvature effects as well as convergence and divergence of streamlines, under the assumption of flow that is locally axisymmetric.

In case of large cross flow, however, this method can be expected to break down, leading to another method (Dvorak et al., 1977b) which is mainly applied on wings. This second method does include a cross-flow model. It divides the span into a strips, each modelled as a separate infinite wing. The boundary layer development on each strip is computed using Dvorak and Woodward (1974), along streamlines from the stagnation point to the trailing edge. These calculations are based on the correlations between boundary layer parameters at the stagnation line (shape factor, momentum thickness and skin friction coefficient) and states (laminar or turbulent) on one hand, and a Reynolds-number like parameter C^* , shown in Equation (4.22), on the other (Cumpsty and Head, 1967; Bradshaw, 1971; Cumpsty and Head, 1969).

$$C^* = V^2 / \left(\nu \frac{dU}{ds} \right) \quad (4.22)$$

For values of C^* lower than $0.135 \cdot 10^5$, the flow is found laminar; otherwise it is turbulent. For unswept wings, two-dimensional correlations – rather than the one presented in Equation (4.22) – are used as input for the boundary layer calculation process. Both boundary layer codes output separation locations.

Laminar flow Both Dvorak et al. (1977a) and Dvorak et al. (1977b) (the ‘cross flow method’) use the same set of laminar equations, based on Curle (1967) and Thwaites (1949), with only momentum thicknesses at the stagnation point slightly varying. Dvorak et al. (1977a) use $\theta_0 = \sqrt{0.0604/dU/dx}$, based on a bluff body, Dvorak et al. (1977b) include the kinematic viscosity ν and use $\theta_0 = \sqrt{0.0855\nu/dU/dx}$. Given the regularly low value of ν , the momentum thickness at the stagnation point predicted by Dvorak et al. (1977b) will be much smaller than the one computed using Dvorak et al. (1977a).

Turbulent flow Whereas the laminar boundary layer equations are largely identical, the computation methods used for analysis of turbulent boundary layers differ substantially. Dvorak et al. (1977a) use a two-dimensional method by Nash and Hicks (1968) based on momentum equations and a skin friction relation by Coles (1956). Dvorak et al. (1977b) and Dvorak and Woodward (1974), instead, use a method by Cumpsty and Head (1967) that is suitable for infinite swept wing three dimensional boundary layers. This difference results in the (in)ability of analysing cross flow, discussed previously.

Transition Just as the laminar flow computations are identical, the transition location is predicted using the same approach. Instability curves are used to find the neutral stability point (Smith, 1957; Smith and Gamberoni, 1956), which is the point from which small disturbances in the boundary layer are

amplified. Transition curves then predict the transition location (Granville, 1953). The initial transition shape factor is given by Coles (1953), laminar separation and reattachment relations follow from Gaster (1967). Especially these last relations are not exact, having been determined based on empirical data.

Wake VSAERO uses a thin wake model and neglects entrainment in the wake. This explains why no source term for the wake is present in Equation (4.18). A boundary condition ensures the wake is aligned with the local flow and “the wake doublet distribution is constant along mean streamlines in the wake surface” (Maskew, 1987, p. 7).

Viscous / inviscid coupling

Both viscous models used in VSAERO feed transpiration source values back to the inviscid potential flow calculation in order to model the displacement effect of the boundary layer. This is computationally more efficient than updating the geometry with the displacement thickness (Dvorak and Woodward, 1974).

Solution procedure

The flow equations described in the previous section are solved on quadrilateral panels, with their control points at the centre of the corner points of the panel. On these panels, the flow model is discretised, yielding a set of linear equations that is subsequently solved. This solution gives the doublet distribution, from which the streamlines can then be determined. Given the fact that VSAERO uses a Morino-type panel method, the doublet distribution is found from the value of potential influence coefficients, whereas other panel methods often use velocities (Margason et al., 1985; Johnson and Rubbert, 1975; Morino et al., 1975). Also, the surface singularity distributions are an input to the wake-shape calculation. This is an iterative process, where the wake is re-panelled in each run.

The viscous part starts with the surface flow solution, from which a boundary layer displacement thickness at each panel is found. This is fed into another iterative loop. Too large differences from the values obtained in a previous iteration result in an update to the wake, as discussed in the previous paragraph. Separation is determined based on “a vanishingly small skin friction coefficient (in the direction of the external streamline)” (Maskew, 1987, p. 58). Induced drag was originally found using pressure integration, but as of version 7 of VSAERO, a Trefftz-plane analysis has been implemented (Nathman, 2005). This was already suggested some 15 years earlier by Letcher Jr. (1989).

When both iterative loops (the potential flow and the boundary layer) have converged, an optional off-body analysis is performed. Ultimately, the output results are determined and shown to the user.

Output

As VSAERO was not available in the period this literature study was conducted, no information on the type and format of the output generated by the code is available at this time.

Results

In the 1980s, VSAERO was one of the most widely used panel codes in US industry (Lord and Zysman, 1986), with Troeger and Selby (1998, p. 184) citing Henne (1990) stating the program has seen such extensive use, the “designation of well-proven design tool” is warranted. Authors stipulate the low computational cost (Strang et al., 1985; Straathof et al., 2010; Straathof and van Tooren, 2011) (also in comparison to other panel methods), making it suitable for use during preliminary design, providing quick performance estimates and assisting in screening efforts (Lord and Zysman, 1986; Khalid et al., 1997). Straathof and van Tooren (2011) have used a more recent version (v7.1, 2005) in an optimisation framework. Nathman (2006) has coupled VSAERO (v7.0, May 2003) to a structural analysis program, using it to investigate oscillatory motion.

Given the wide use, it is unsurprising that various in-depth comparisons and validation studies are reported in literature. The aforementioned theory document also includes a validation section and concludes that computational results closely resemble experimental values, in case of isolated wings or bodies, wing-body combinations and nacelles. Most literature notes good agreement between theoretic-

cal and experimental results (Troeger and Selby, 1998; Khalid et al., 1997; Ghaffari, 1988; Filippone and Selig, 1998; Lednicer and Gilchrist, 1991), in terms of pressure distributions and lift, drag and pitching moment coefficients. In Nathman and McComas (2008), lift is slightly underpredicted; Margason et al. (1985) note overprediction, either by a constant offset or increasing with α . The fact that VSAERO is essentially an incompressible method is clearly observed in studies investigating performance at higher subsonic Mach numbers. Lord and Zysman (1986) noted poorer performance at $M_\infty = 0.8$. From a Mach number of 0.6, the increase in lift due to Mach number is underpredicted (Margason et al., 1985). Predicting separation is challenging at times, resulting in discrepancies between predicted and measured trailing edge pressure distributions, especially outboard (Margason et al., 1985)¹³ and computed and measured high- α lift coefficients (Filippone and Selig, 1998). Estimations of spanwise load distributions are better towards the root than the tip (Margason et al., 1985) and tip separation was determined difficult to predict (Filippone and Selig, 1998; Strang et al., 1985; Troeger and Selby, 1998).

Whereas Troeger and Selby (1998) argue the observed discrepancies in pressure distribution can be attributed to the inviscid simulation environment (in this research, the boundary layer module was not used), in which separation is not predicted but instead fixed at the trailing edge, the more complex geometry caused by trailing edge movables, might have also complicated matters¹⁴. Strang et al. (1985) assign blame to the discontinuities in potential between the panels – a direct result of the low-order method. Increasing the number of panels can circumvent these discontinuities and make the lower-order methods perform as well as higher-order codes, but comes at additional cost. The importance of proper panelling is stressed by others, too (Maskew, 1987; Lord and Zysman, 1986). Despite this, Letcher Jr. (1989) obtained reasonably accurate predictions of lift and pitching moment coefficients, even at lower panel densities.

Another problem that can be solved by increasing the amount of panels is inaccurate drag predictions seen in earlier versions of VSAERO (Letcher Jr., 1989; Nathman, 2005; Troeger and Selby, 1998; Lednicer and Gilchrist, 1991). Before v7.0, the induced drag was computed based on pressure integration. A substantial improvement was made when a Trefftz-plane analysis (a *far-field* approach) was added to the software (in v7.0), yielding much improved estimations for induced drag (Nathman, 2005)¹⁵.

4.2.4. MATRICES / -V

MATRICES (an acronym for *Multi-component Aircraft TRansonic Inviscid Computation System*) and MATRICES-V (sometimes also stylised as MATRICESV) are inviscid and viscous flow solvers developed by the Dutch National Aerospace Laboratory (NLR) (van der Vooren et al., 1986; van der Vooren and van der Wees, 1991; van der Wees and van Muijden, 1992; van der Wees et al., 1993). MATRICES uses a full potential flow model, which MATRICES-V extends with a viscous unsteady integral boundary layer formulation. Both tools are intended for analysis of the transonic flow about wing/body configurations and (inverse) wing design purposes (van der Wees et al., 1993) and utilise a finite volume method. Computational effort is reduced by only modelling a semi-configuration, which is mirrored in the xz -plane. As such, it cannot handle non-zero sideslip values (Elham, 2013).

A user manual to the current version is not available, but the four previously cited publications document the original setup of the programs. It is unknown as to what extent these documents still hold for current versions of the program. Especially since all publications speak of the software being in development, this is an important concern. Still, lacking any other means, the information in the remainder of this section is based on these references, unless indicated otherwise.

¹³Most likely due to low quality printing and/or digitising, the different series in the graphs presenting measurement data are virtually indiscernible. The remarks based on this paper are based on the accompanying text. It has to be noted, though, that the conclusion drawn is substantially milder, noting that “[i]n general, the total lift, pressures, and spanwise loads predicted by the five methods agree well with experiment.” (Margason et al., 1985, p. 6).

¹⁴On the other hand, if VSAERO was indeed originally developed for analysis of high-lift configurations, as Lord and Zysman (1986) note, it seems unlikely the program should struggle with this geometry.

¹⁵Nathman is the director of software development of Analytical Methods, Inc., the company developing VSAERO.

Flow model

Whereas MATRICS only includes an inviscid solver, MATRICS-V adds to this an integral boundary layer model (Mariens et al., 2014; Elham and van Tooren, 2014; Elham et al., 2014). In that case, the boundary layer is only modelled on the wing and wake and not on the body.

Inviscid formulation

The inviscid formulation found in MATRICS is “based on a fully conservative finite-volume scheme for the full-potential equation in strong conservation form” (van der Vooren and van der Wees, 1991, p. 869). Including artificial viscosity through the fluxes P , Q and R (functions of density, Mach number, velocity, strain and mesh size in x , y and z -direction, as documented in van der Vooren and van der Wees (1991, Eq. (5))) to smear out discontinuities (in the form of shock waves) in the flow yields Equation (4.23), with the velocity components defined by Equation (2.11):

$$(\rho u + P)_x + (\rho v + Q)_y + (\rho w + R)_z = 0 \quad (4.23)$$

In this equation, the density ρ is given by Equation (4.24), in which V is the norm of the velocity vector:

$$\rho = \left(1 + \frac{\gamma - 1}{2} M_\infty^2 [1 - V^2]\right)^{\frac{1}{\gamma - 1}} \quad (4.24)$$

As the artificial viscosity is unequal to zero in subsonic parts of the flow, only supersonic/supersonic shock waves are smeared out completely. In case of supersonics/subsonic shocks, a “true discontinuity with sonic conditions on its upstream side” is formed, labelled a ‘shock reminder’ (van der Vooren, 1989).

The total inviscid pressure drag is found from summing the induced drag, wave drag and spurious drag, and is second-order accurate with respect to mesh size and fourth-order with respect to the magnitude of disturbance velocities (van der Vooren and van der Wees, 1991). The first drag contribution is computed using a Trefftz-plane (assuming small disturbances therein) and performing the integration shown in Equation (4.25):

$$D_i = \frac{1}{2} \rho_\infty \int_{S_T} (v^2 + w^2) dS \quad (4.25)$$

The second contribution (wave drag) is the sum of the Garabedian wave drag (Garabedian, 1976; Garabedian and McFadden, 1982) and the ‘shock remainder’ (i.e., the remaining flow disturbance left after a shock wave has been smoothed out by artificial viscosity, as described earlier) wave drag, listed in Equation (4.26).

$$D_{wG} = \int_{V_{M>1, q_s<0}} (\bar{P}u_x + \bar{Q}u_y + \bar{R}u_z) dV \quad (4.26a)$$

$$D_{w_{sr}} = \int_{S_S} [(p_d + p_u^*)n_x + \rho_d q_{nd} (u_d - u_u^*)] dS \quad (4.26b)$$

The spurious drag contribution, then, is formed by Equation (4.27). This is identical to Equation (4.26a), with the exception that q_s (the local acceleration) is now larger than 0. This spurious drag component is an artificial one that is created by the artificial viscosity discussed previously.

$$D_s = \int_{V_{M>1, q_s>0}} (\bar{P}u_x + \bar{Q}u_y + \bar{R}u_z) dV \quad (4.27)$$

Whether an additional term representing the excess mass drag should be included in the equation for spurious drag depends on whether a fully conservative scheme is used¹⁶. If there is, Equation (4.27) stands as is. If not, Equation (4.28) should be added to Equation (4.27). This represents excess mass created in the non-conservative case. In the fully conservative case, the mass that is created as a result of the artificial viscosity is negated by the removal of this mass in the shock remainders, leading the term to equate to 0 (Elham, 2013; van der Vooren, 1989; Ross, 1987; Garabedian, 1976).

$$D_{s,m} = \int_{S_S} \Delta \bar{M} (u_u^* - u_{\infty}) dS \quad (4.28)$$

In a completely inviscid analysis without boundary layer model, a zero normal velocity (flow tangency condition) is enforced on the wing surface and in the symmetry plane (van der Wees, 1985). If a boundary layer is present, the wall boundary condition is such that mass flux through the wing surfaces is allowed. Continuing the boundary layer downstream to form the wake, the displacement effect is realised using jumps in normal flux. In the far-field, the perturbation potential is set to 0. An exception to this forms the downstream far-field (the Trefftz-plane) in which “the curvature of the perturbation potential is set to zero in the direction of the streamwise grid lines” (van der Wees et al., 1993, p. 3).

Viscous formulation

The steady boundary layer equations, obtained from integration of the unsteady formulation, used in MATRICS-V are based on Myring (1970) (quoted in Smith (1972) and Chow (1985)). With the addition of time-dependent terms (first line in each of the subsequent momentum equations) and the use of first order integral thicknesses, the boundary layer equations from Myring can be integrated in z -direction (i.e., normal to the wing surface or wake centreline). The pressure is eliminated from the equation using the momentum equation in z -direction. This can be done as the three-dimensional problem is formulated as two-dimensional (van der Wees et al., 1993), leaving only momentum equations in x - and y -directions as shown in Equation (4.29) (van der Wees and van Muijden, 1992)¹⁷:

$$\begin{aligned} & \frac{1}{q_e} \frac{\partial \delta_1}{\partial t} - \frac{u_e}{q_e^2} \frac{\partial \delta_\rho}{\partial t} + \left(\frac{1}{q_e^2} [1 - M_e^2] \delta_1 + \frac{u_e}{q_e^3} M_e^2 \delta_\rho \right) \frac{\partial q_e}{\partial t} \\ & + \frac{1}{h_1} \frac{\partial \theta_{11}}{\partial x} + \theta_{11} \left(\frac{2 - M_e^2}{h_1} \frac{1}{q_e} \frac{\partial q_e}{\partial x} + \frac{1}{J} \frac{\partial}{\partial x} \left[\frac{J}{h_1} \right] + k_1 \right) \\ & + \frac{1}{h_2} \frac{\partial \theta_{12}}{\partial x} + \theta_{12} \left(\frac{2 - M_e^2}{h_2} \frac{1}{q_e} \frac{\partial q_e}{\partial y} + \frac{1}{J} \frac{\partial}{\partial y} \left[\frac{J}{h_2} \right] + k_3 \right) \\ & + \delta_1 \left(\frac{1}{h_1} \frac{1}{q_e} \frac{\partial u_e}{\partial x} + k_1 \frac{u_e}{q_e} \right) + \delta_2 \left(\frac{1}{h_2} \frac{1}{q_e} \frac{\partial u_e}{\partial y} + k_2 \frac{v_e}{q_e} + k_3 \frac{u_e}{q_e} \right) \\ & + \theta_{22} k_2 = \frac{1}{2} C_{f1} \end{aligned} \quad (4.29a)$$

¹⁶This is not immediately clear from the cited references. Van der Vooren and van der Wees (1991) discuss this term in one breakdown (Fig. 1), but later on define the D_s as shown in Equation (4.27) without any explanatory remarks. It also is not part of van der Vooren and van der Wees (1991, Eq. (9)), in which the right-hand terms describe induced drag, the drag associated to the shock remainder shown in Equation (4.26b), and the summation of Equations (4.26a) and (4.27).

¹⁷Van der Wees and van Muijden (1992) use overbars to indicate values at the edge of the boundary layer, whereas in this text, the subscript $(\cdot)_e$ is used, consistent with earlier notations. Furthermore, the term $\partial \delta_\rho$ (density) in Equation (4.29a) originally read $\partial \delta_p$ (pressure) in van der Wees and van Muijden (1992, Eq. 11). As this is not defined, and as the same time-dependent term appears in Equation (4.29b), this is assumed erroneous and corrected in the current text.

$$\begin{aligned}
& \frac{1}{q_e} \frac{\partial \delta_2}{\partial t} - \frac{v_e}{q_e^2} \frac{\partial \delta_\rho}{\partial t} + \left(\frac{1}{q_e^2} [1 - M_e^2] \delta_2 + \frac{v_e}{q_e^3} M_e^2 \delta_\rho \right) \frac{\partial q_e}{\partial t} \\
& + \frac{1}{h_1} \frac{\partial \theta_{21}}{\partial x} + \theta_{21} \left(\frac{2 - M_e^2}{h_1} \frac{1}{q_e} \frac{\partial q_e}{\partial x} + \frac{1}{J} \frac{\partial}{\partial x} \left[\frac{J}{h_1} \right] + l_3 \right) \\
& + \frac{1}{h_2} \frac{\partial \theta_{22}}{\partial x} + \theta_{22} \left(\frac{2 - M_e^2}{h_2} \frac{1}{q_e} \frac{\partial q_e}{\partial y} + \frac{1}{J} \frac{\partial}{\partial y} \left[\frac{J}{h_2} \right] + l_2 \right) \\
& + \delta_2 \left(\frac{1}{h_2} \frac{1}{q_e} \frac{\partial v_e}{\partial y} + l_2 \frac{v_e}{q_e} \right) + \delta_1 \left(\frac{1}{h_1} \frac{1}{q_e} \frac{\partial v_e}{\partial x} + l_1 \frac{u_e}{q_e} + l_3 \frac{v_e}{q_e} \right) \\
& + \theta_{11} l_1 = \frac{1}{2} C_{f2}
\end{aligned} \tag{4.29b}$$

In these equations, u and v are velocities in x - and y -direction (chordwise and spanwise, respectively), with q indicating the total velocity (as in Equation (4.24)). M_e is the Mach number at the edge of the boundary layer. C_{f1} and C_{f2} are skin friction coefficients in x - and y -directions. J is the Jacobian of the transformation from the physical domain to the computational domain, h_1 and h_2 are metric coefficients of the (x, y) coordinate system, k_i and l_i (with $i \in 1, 2, 3$) are functions thereof as defined in Smith (1972, App. A). δ without subscript indicates the boundary layer thickness, δ with subscript represents the mass integral thickness and θ with subscript is the momentum integral thickness (Chow, 1985). In the latter two cases, subscripts determine the direction in the (x, y) axis system. δ_ρ , finally, is the density thickness, defined as the integral $\int (\rho_e - \rho) / \rho_e$ over the boundary layer (van der Wees and van Muijden, 1992).

The system is completed by the entrainment equation shown in Equation (4.30), an extension of the equation put forward by Houwink and Veldman (1984), based on Green et al. (1977). C_E is the entrainment coefficient, representing the non-dimensional rate of mass flow change in the boundary layer.

$$\begin{aligned}
& \frac{1}{\rho_e q_e J} \left(\rho_e J \frac{\partial}{\partial t} (\delta - \delta_\rho) - J \frac{\rho_e}{q_e} M_e^2 (\delta - \delta_\rho) \frac{\partial q_e}{\partial t} + \frac{\partial}{\partial x} \left[\frac{\rho J}{h_1} (u_e \delta - u_e \delta_1) \right] + \frac{\partial}{\partial y} \left[\frac{\rho J}{h_2} (v_e \delta - q_e \delta_2) \right] \right) \\
& = \frac{1}{q_e} \left(\frac{u_e}{h_1} \frac{\partial \delta}{\partial x} + \frac{v_e}{h_2} \frac{\partial \delta}{\partial y} - w_e + \frac{\partial \delta}{\partial t} \right) = C_E
\end{aligned} \tag{4.30}$$

The non-dimensional mass flux through the wing and wake surfaces, then, is given by Equation (4.31), based on Chow (1985). This represents the displacement effect the boundary layer has on the inviscid flow.

$$S = \frac{1}{\rho_e q_e J} \left(\rho_e J \frac{\partial \delta_\rho}{\partial \delta} - J \frac{\rho_e}{q_e} M_e^2 \delta_\rho \frac{\partial q_e}{\partial t} + \frac{\partial}{\partial x} \left[\frac{\rho_e J}{h_1} q_e \delta_1 \right] + \frac{\partial}{\partial y} \left[\frac{\rho_e J}{h_2} q_e \delta_2 \right] \right) \tag{4.31}$$

The density is eliminated from these equation using the Crocco relation (Cebeci and Smith, 1974) and with a set of empirical two-dimensional closure relations for attached and separated flow (Cousteix, 1987; Cousteix and Houdeville, 1981; Green et al., 1977; Houwink and Veldman, 1984). Van der Wees and van Muijden (1992, p. 3) note that these relations are supposed to be replaced by “more physical closure relations and velocity profile families”, but it is unknown if, when and how this change was implemented. These relations are used to reduce the number of unknowns to four: the streamwise momentum integral thickness θ_{11} , the transformed boundary layer shape factor H_e , the total velocity q_e and the crossflow factor C , given by Equation (4.32):

$$C = \frac{\text{sgn}(\beta_w) \sqrt{-\theta_{22}}}{\delta_1} \tag{4.32}$$

Elham (2013) indeed describes that the laminar closure relations used in MATRICS-V are the Falkner-Skan relations, as given by Cousteix (1987). In the turbulent case, the shape-factor relation is changed

based on the lift-off formulation by [le Balleur \(1981\)](#), the results by [Melnik and Brook \(1985\)](#) regarding separated flow, the skin friction relation by [Swafford \(1980, 1983\)](#) (also used by XFOIL) and corrections for low-Reynolds number applications by [Bandyopadhyay \(1992\)](#). As not all of these references appear in any of the four primary publications cited at the beginning of this sub-section, it is unclear when and in what final form these relations were implemented in MATRICS-V.

Boundary conditions are applied to set all derivatives in the local sweep direction at the wing root to zero. [Van der Wees et al. \(1993\)](#) furthermore note that no downstream boundary conditions are applied, as to not influence the upstream dependency of the flow characteristics, although [van der Wees and van Muijden \(1992\)](#) describe that for all quantities a zero gradient condition is enforced in chordwise direction. Both sources also mention “zero derivatives in the local sweep direction” at the wing tip ([van der Wees et al., 1993](#), p. 3), referring to [Cross \(1979\)](#), but as that reference could not be accessed, it could not be confirmed whether the derivatives are enforced at a zero value, or that no derivatives are prescribed and all are left free.

Transition Neither [van der Wees and van Muijden \(1992\)](#) nor [van der Wees et al. \(1993\)](#) explicitly discern between a laminar and a turbulent flow model ([Elham \(2013\)](#) does), but note that the initial conditions of the turbulent boundary layer (which are governed by the laminar boundary layer) are given by the BOLA-2D solver (used in *direct mode*), another boundary layer model developed by NLR ([de Bruin and de Boer, 1982](#)). This is used to generate the laminar quasi-two-dimensional flow present at the leading edge of the wing, leading to the hypothesis that BOLA-2D solves the laminar problem and the aforementioned equations are solely used for turbulent computations. [Mariens et al. \(2014\)](#) state MATRICS-V includes two transition options, but [van der Wees et al. \(1993, p. 3\)](#) and [Elham \(2013\)](#) only discuss that “an extended Granville criterion [...] has been implemented to test on possible transition”, referring to [Cousteix \(1987\)](#).

Mild separation of the turbulent boundary layer (BOLA-2D assumes attached flow) is allowed (although [Mariens et al. \(2014\)](#) talk of the “capability to model considerable boundary layer separation”), in which a so-called interaction law prevents breakdown of the boundary layer formulation. This interaction law, which adjusts the edge velocity of the inviscid part of the flow in order to obtain a convergent numerical solution, is slightly modified from [Williams \(1989\)](#) and shown in Equation (4.33). According to [van der Wees and van Muijden \(1992\)](#), it has no effect on the final solution, as it is in correction form.

$$\frac{\partial q_e}{\partial s} - \frac{q_e \pi}{\beta \Delta x} S = \left(\frac{\partial q_e}{\partial s} \right)^k - \frac{q_e^k \pi}{\beta^k \Delta x} S^k \quad (4.33)$$

Viscous / inviscid coupling

MATRICES-V uses a viscous-inviscid interaction method. In the laminar flow region, the inviscid flow properties are computed by specifying a source of strength S on the wing. Sources are also located on the wake and a velocity jump across the wake is prescribed.

The viscous computation is obtained quasi-simultaneously ([Lock and Williams, 1987](#)), in which the inviscid wall velocity is prescribed ([Elham, 2013](#)). A correction for curvature effects of the boundary layer is included. In the iterative process, boundary layer computations yield an updated source strength and velocity jump, which is then fed back to the inviscid calculations until convergence is obtained.

Solution procedure

The computational domain in MATRICS / -V is composed of a main grid and several smaller sub grids of C-O topology ([Elham, 2013](#)). The coarser main grid takes care “of the efficient gross interaction between the various aircraft components” ([van der Vooren et al., 1986](#), p. 4); the subgrids yield detailed solutions for the different components of interest (e.g., wing, nacelle, body, pylon). Conformity of the component boundary on the sub grid is stringent, whereas this requirement is somewhat more relaxed on the main grid. The main grid is generated using MATGRID ([Tysell and Hedman, 1988](#)). Over the cut in the C-O topology that extends from the wing tip, normal and potential flux are prescribed using a boundary

condition (van der Wees et al., 1993).

The potential equation is discretised on a curvilinear coordinate system. This is second-order accurate almost everywhere, except in supersonic regions, where first-order accuracy is obtained (van der Wees et al., 1993). The grids are made up of cubical cells defined by their corner-point coordinates, and for each of which, the velocity disturbance potential is computed in the corner points. Trilinear interpolation is used to determine intermediate values.

A so-called non-linear FAS (full approximation storage) multigrid method is selected to solve the flow model, with the ILU/SIP (incomplete lower upper decomposition / strongly implicit procedure) smoothing algorithm (Meijerink and van der Vorst, 1977; Stone, 1968). The idea behind the multigrid method is to reduce computational effort by solving the flow model on successively finer grids, using the information obtained on coarser grids. In the MATRICS / -V code, these coarser grids are obtained by removing every other grid point on the finer grid. FAS, specifically, is suited for non-linear problems as this scheme is able to transfer the nonlinearities to the coarser grids through re-discretization (Blazek, 2007). Further details of the ILU/SIP smoothing algorithm, which go beyond the scope of the current text, are available in van der Wees (1985), Stone (1968) and Meijerink and van der Vorst (1977); its implementation is most extensively discussed in van der Vooren et al. (1986).

A dummy gridpoint approach (described in (van der Wees et al., 1983)) is used to implement the boundary conditions that are not of the Dirichlet-type. This makes the application of the boundary conditions not completely exact (van der Wees et al., 1983).

Output

As neither MATRICS nor MATRICS-V was available in the period this literature study was conducted, no information on the type and format of the output generated by the codes is available at this time.

Results

Only very little publications using MATRICS or MATRICS-V could be found. Elham and van Tooren (2016) use it to validate another aerodynamic solver (Q3D, treated in Section 4.3.2), but do not discuss the accuracy or performance of MATRICS-V itself. These validation results are scarce, but not entirely absent. Van der Vooren et al. (1986) compare the inviscid solver MATRICS to a higher order panel method by Roberts (documented in Sytsma et al. (1979)) and observe excellent agreement in the prediction of pressure distribution, which only show small differences near the tip and the trailing edge. These deviations are caused by (unspecified) discrepancies in the implementation of the Kutta condition, dissimilar spanwise grid distributions and a contrasting treatment of the wing tip.

Elham (2013), citing van Muijden et al. (1996), compares pressure distributions obtained by MATRICS-V for a DLR-F4 wing-body combination to these obtained in wind tunnel experiments (shown in Figure 4.10) and wind tunnel and flight test results of a Fokker 100 wing-body combination (these latter two also documented in van der Wees et al. (1993)). The smallest errors are found in the F4 case, with only some minor discrepancies in terms of predicted shock location at the outboard wing sections. In the Fokker tests, some inequality in shock location is predicted for the wind tunnel experiments, whereas the flight test comparison shows more notable differences in upper surface pressure distribution upstream of the shock wave. The sensitivity of the computations with respect to shock wave strength and location is also noted in van der Vooren et al. (1986), showing that the amount of artificial viscosity, the use of a freestream-consistent computational scheme and the size of the computational domain also notably impact their accurate prediction. R. Vos (personal communication, July 13th, 2018) has noted that MATRICS-V produces best results when Fokker 100-like wing-body configurations are analysed.

Validation of derivative results (such as lift, drag and pitching moment estimations) could not be found, but the generally accurate estimations of pressure distributions discussed before instil trust. This especially holds for lower subsonic speeds, where shock waves do not yet play an important role – and possible errors in their estimation have a less severe impact on the results.

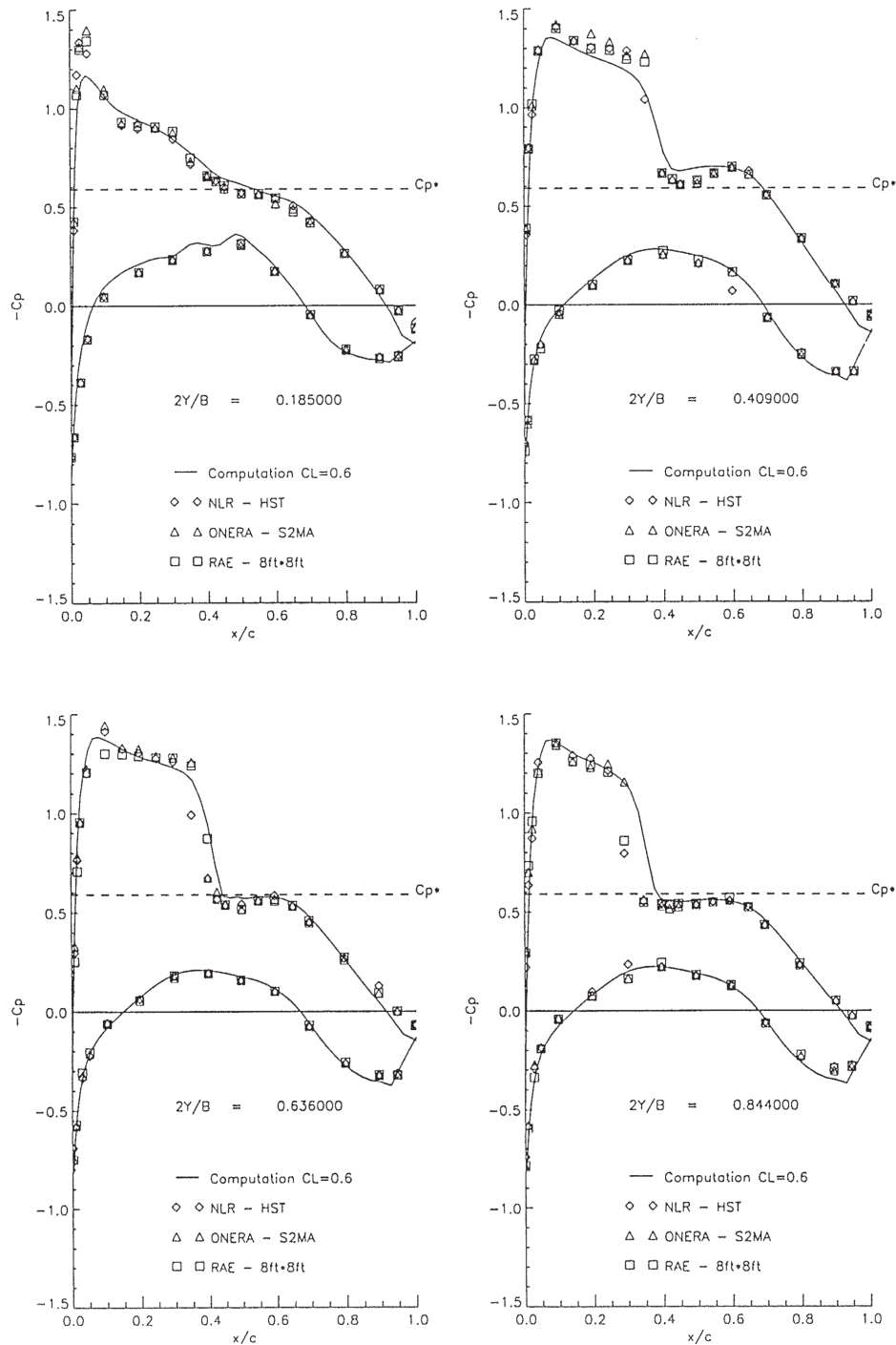


Figure 4.10: Comparison of pressure coefficients of a DLR-F4 wing-body configuration as predicted by MATRICS-V and found in experiment, illustrating MATRICS-V performance (Elham, 2013, p. 253)

4.2.5. Stanford University Unstructured (SU2)

Rather than a program intended solely for CFD purposes, SU2 (also stylised as SU², short for *Stanford University Unstructured*) is a “computational analysis and design package that has been developed to solve multiphysics analysis and optimization tasks using unstructured mesh topologies” (Economou et al., 2016b, p. 828). It was launched in 2012 (Myers, 2012) and has reached version 6.0.0 in early 2018 (su2code, 2018). The program is modular in set-up and applicable to various partial differential science

and engineering problems. At the core is a Reynolds-averaged Navier-Stokes solver.

Corresponding to this modular set-up, SU2 can solve the full (laminar) and Reynolds-averaged (turbulent) Navier-Stokes equations as well as the Euler equations using FVM and FEM solvers, or a combination thereof (in case of multiphysics problems). Included tools for adjoint-based sensitivity analysis and uncertainty quantification make the suite suitable for design optimisation problems (Kiyici and Aradag, 2015; Munguía et al., 2017; Kusch et al., 2018; Yang and da Ronch, 2018), in addition to the analysis capabilities offered. SU2 is an open-source program that originated at the Aerospace Design Laboratory at Stanford University and to which various institutions around the world currently contribute, amongst of which Delft University of Technology (Economon et al., 2016b; Palacios et al., 2013; Vitale et al., 2015; Pini et al., 2017). Focus in this section is on the workings and capabilities of SU2 as a CFD analysis tool.

Online documentation is available through the website of the project, but is mostly geared towards users and developers of the program (SU2, 2018). Palacios et al. (2013), Palacios et al. (2014) and Economon et al. (2016b) provide details on the code philosophy, as well as the underlying physical and mathematical models contained in it. Unless indicated otherwise, the information in the remainder of this section is based on these three academic references.

Flow model

The basis of SU2 is formed by a RANS solver. By default, this models viscous, compressible turbulent flow. Using artificial compressibility, the equations can be modified to be applicable to incompressible flow. The compressible RANS equations can also be simplified by disabling turbulence modelling (yielding laminar Navier-Stokes equations) or neglecting viscosity altogether (resulting in an Euler model). These four implementations are further detailed below. In all cases, the problem under consideration is expressed as a partial differential equation of the form shown in Equation (4.34):

$$\frac{\partial}{\partial t} \mathbf{U} + \nabla \cdot \mathbf{F}^c - \nabla \cdot \mathbf{F}^v = \mathbf{Q} \quad \text{in } \Omega, t > 0 \quad (4.34)$$

In this equation, \mathbf{U} is the state vector and \mathbf{F}^c and \mathbf{F}^v represent the convective and viscous fluxes, respectively.

Table 4.3 shows which boundary conditions are supported in the RANS solver – in compressible and incompressible flows. In the Euler solver, a flow tangency boundary condition is also available.

Inviscid formulation

In case of the fully inviscid formulation, Equation (4.34) is used with \mathbf{F}^c as given in Equation (4.35) and $\mathbf{F}^v = \mathbf{0}$.

Viscous formulation

Viscous and compressible flow is modelled using Equation (4.34). The state vector is given as $\mathbf{U} = (\rho, \rho u, \rho v, \rho w, \rho E)^T$ ¹⁸ and \mathbf{F}_i^c and \mathbf{F}_i^v as shown in Equation (4.35):

$$\mathbf{F}_i^c = \begin{pmatrix} \rho u \\ \rho u V_i + p \delta_{ix} \\ \rho v V_i + p \delta_{iy} \\ \rho w V_i + p \delta_{iz} \\ \rho V_i H \end{pmatrix}, \quad \mathbf{F}_i^v = \begin{pmatrix} \cdot \\ \tau_{ix} \\ \tau_{iy} \\ \tau_{iz} \\ v_j \tau_{ij} + \mu_{tot}^* C_p \frac{\partial}{\partial i} T \end{pmatrix} \quad (4.35)$$

¹⁸Palacios et al. (2013) uses v_1 , v_2 and v_3 for the velocity components here indicated u , v and w . V is used to represent the total flow velocity, designated v in the original source.

Table 4.3: Boundary conditions supported by the compressible and incompressible RANS solver in SU2 (Palacios et al., 2013; Economon et al., 2016b)

Boundary condition	Compressible solver	Incompressible solver
Wall symmetry	✓	✓
No-slip wall (adiabatic)	✓	✓
No-slip wall (isothermal)	✓	
Far-field boundaries	✓	
Near-field boundaries	✓	
Inlet boundaries (stagnation prescribed)	✓	✓
Inlet boundaries (mass flow prescribed)	✓	✓
Inlet boundaries (supersonic conditions prescribed)	✓	
Outlet boundaries (back pressure prescribed)	✓	✓
Periodic boundaries	✓	
Nacelle inflow boundaries (fan face Mach number prescribed)	✓	
Nacelle exhaust boundaries (total nozzle temperature and pressure prescribed)	✓	

Upon substitution into Equation (4.34), the first row forms the continuity equation, the second, third and fourth rows together represent the conservation of momentum (in the three Cartesian components) and the fifth row is the energy equation.

In the incompressible formulation, these definitions change to the ones shown in Equation (4.36), corresponding to a state vector $\mathbf{U} = (p, \rho u, \rho v, \rho w)^T$. With the assumption of constant density, the system has one less unknown and therefore one less equation. Although the model still includes (turbulent) viscosity, the artificial compressibility (Chorin, 1997) with parameter β limits the use of the model to steady-state flow.

$$\mathbf{F}_i^c = \begin{pmatrix} \beta^2 V_i \\ \rho u V_i + p \delta_{ix} \\ \rho v V_i + p \delta_{iy} \\ \rho w V_i + p \delta_{iz} \end{pmatrix}, \quad \mathbf{F}_i^v = \begin{pmatrix} \cdot \\ \frac{\partial}{\partial i} u \\ \frac{\partial}{\partial i} v \\ \frac{\partial}{\partial i} w \end{pmatrix}, \quad \mathbf{Q} = \begin{pmatrix} \cdot \\ \cdot \\ \cdot \\ -\frac{\rho}{Fr^2} \end{pmatrix} \quad (4.36)$$

In these vector definitions, δ_{ij} is the Kronecker delta function (equal to 1 if $i = j$, 0 otherwise), H the enthalpy, C_p the specific heat at constant temperature and T the temperature itself. τ_{ij} are the viscous stresses, computed using Equation (4.37):

$$\tau_{ij} = \mu_{tot} \left(\partial_j V_i + \partial_i V_j - \frac{2}{3} \delta_{ij} \nabla \cdot \mathbf{V} \right) \quad (4.37)$$

The two forms of μ_{tot} , representing the viscosity, are defined in Equation (4.38) and follow the Boussinesq hypothesis introduced in Section 2.1.4 (Wilcox, 2006; Blazek, 2007; Palacios et al., 2013).

$$\mu_{tot} = \mu_{dyn} + \mu_{turb} \quad (4.38a)$$

$$\mu_{tot}^* = \frac{\mu_{dyn}}{Pr_{dyn}} + \frac{\mu_{turb}}{Pr_{turb}} \quad (4.38b)$$

Laminar flow If turbulence modelling is disabled, a laminar (full) Navier-Stokes solution is obtained. In this case, the relations in Equation (4.35) still hold, with the difference that the last term in F_i^v only depends on laminar stresses, as μ_{turb} tends to 0 and μ_{tot} thereby reduces to μ_{dyn} . This dynamic viscosity follows from Sutherland's law (assuming an ideal gas, μ_{dyn} can be written as a function of temperature, a reference viscosity and a constant (White, 1991)).

Turbulent flow If a turbulent solution is sought, μ_{turb} is given by a turbulence model. The SU2 code includes two of these: the one-equation Spalart-Allmaras (S-A) model (Spalart and Allmaras, 1992) and the Menter shear stress transport (SST) model (Menter, 1993). The latter is a two-equation model that combines the $k - \omega$ - and the $k - \epsilon$ -models mentioned in Section 2.1.6. The $k - \omega$ model is used for the inner 50% of the boundary layer and (a $k - \omega$ representation of) the $k - \epsilon$ -model is gradually blended in towards the boundary layer edge, combining the advantages (near-wall accuracy of $k - \omega$, independence of free-stream of $k - \epsilon$) of both (Menter, 1993).

Transition Transition is predicted by the $\gamma - \overline{Re_{\theta t}}$ -S-A-model (Medida and Baeder, 2011b,a). It is an application of the previously developed $\gamma - \overline{Re_{\theta t}}$ -model by Langtry and Menter (2009), which was developed for the SST model by Menter (1993), to the Spalart-Allmaras turbulence model. Both are correlation-based models that use the intermittency γ (0 for laminar, 1 for turbulent) to control the 'production' of turbulent kinetic energy in the turbulence model. Intermittency starts to grow from the critical Reynolds number $Re_{\theta c}$, which thereby determines the transition (onset) location (Medida and Baeder, 2011a).

Viscous / inviscid coupling

No inviscid / viscous coupling is incorporated in SU2, as the flow models are inherently viscous (NS and RANS) or inviscid (Euler).

Solution procedure

Just as SU2 includes various options of representing the flow, the suite offers a number of solution procedures. First of all, the models can be solved using either finite volume or finite element methods. Unstructured two- as well as three-dimensional meshes are supported, meaning elements can take the shape of triangles or rectangles, or tetrahedrons, hexahedrons, and so on. For dynamic problems, such as flow simulations about an extending or retracting high-lift system, the governing equations can be expressed in a special Arbitrary-Lagrangian-Eulerian form and mesh nodes can rotate and translate in time.

Space integration is performed using either of a number of centred or upwind methods in case of the convective fluxes, such as JST (Jameson et al., 1981) and Roe (Roe, 1981). Both convective as well as viscous fluxes are computed at the edge midpoints. Possible source terms are assumed piecewise constant. Time integration can be implicit (using an implicit Euler scheme) or explicit (using a Runge-Kutta method). Local time stepping is used in steady simulations to speed up convergence. In unsteady simulations, a dual time-stepping method is used to improve high-order accuracy in time.

A number of other convergence acceleration strategies is implemented, among which a nonlinear multi-grid method (introduced at the end of Section 4.2.4), so-called linelet preconditioning (transforming a system to make it more suitable for numerical simulation) and Roe-Turkel low Mach number preconditioning. This last strategy makes it possible to solve (nearly) incompressible problems using solution methods that were developed for compressible flows, something that is not automatically the case because standard discretisation methods incorrectly scale the artificial viscosity with Mach numbers reducing to 0, resulting in excess artificial viscosity in the lower Mach number regime.

The ability to solve multi-physics problems in SU2 is also directly employed by the RANS solver. The mean flow properties are computed separately from the turbulence model and coupled afterwards.

Output

Because of time constraints, no simulations were performed using SU2, such that the type and format of the output generated by the code could not be inspected. Based on literature, it is however noted that a separate software program (such as Tecplot) is required to display the (numerical) data output by SU2.

Results

Even though the software has only been around for a few years, the number of citations of the first publication (Palacios et al., 2013), displayed in Table 4.1, provides an indication of the use. With respect to the other methods presented in the current section, the citation amount might be increased because of the wide area of problems SU2 is applicable too. Indeed, Palacios et al. (2013) present validation results ranging from analysis of wings to plasma streams, and from optimisation studies of airfoils to rotor geometries. SU2 is also recognised by parties researching organic Rankine cycles for power generation (Keep et al., 2017). This section is limited to a discussion of results of aerodynamic airfoil, wing and aircraft analyses.

There are multiple validation efforts found in literature in that subset of possibilities. Palacios et al. (2014, p. 33) themselves have published a wealth of verification and validation results, some of them also found in Palacios et al. (2013) and Economon et al. (2016a), concluding “excellent agreement with both the available experimental data and numerical simulations results from well-established computational tools developed at NASA”. In three unit tests (a flat plate, a bump in a channel and a square cylinder), good results were obtained. Using the SST turbulence model, the numerical scheme (1st order Roe or 2nd order Roe with Venkatakrishnan-limiter (Palacios et al., 2014)) was of larger influence than when using the S-A model, with the first-order scheme performing best.

Moving to airfoils, Palacios et al. (2014) shows more accurate results for a symmetrical than for a cambered airfoil, both tested at $Re \approx 1 \cdot 10^6$ and low speeds. Pressure coefficient predictions are slightly off at higher angles of attack, yielding errors in the estimation of aerodynamic performance. The authors note the convective numerical method and turbulence model do influence the prediction of skin friction. In a comparison with experimental data of a multi-element (slat, main element and flap) airfoil (Chin et al., 1993) at a higher Reynolds number, good agreement was observed, but some larger discrepancies in the flow over the slat were found: the pressure drop over the top surface is overpredicted. Lift coefficients match experimental results very well in the linear region ($\alpha \leq 15^\circ$), but also quite good agreement (8% underprediction at most) is observed at and slightly beyond stall. Good stall predictions are also observed by Velázquez et al. (2017), although the lift coefficient is underestimated. Vaithyanathasamy et al. (2018) noted an overprediction of c_p in high- α inviscid simulations at lower Reynolds numbers, but otherwise good results. SU2 is able to generally predict transition accurately, but somewhat too early at angles of attack above 5° (Shengjun et al. (2016), comparing with experimental data from Klausmeyer and Lin (1997)). Performance in the transonic domain was validated by comparison with experimental results of a RAE 2822 supercritical airfoil (Palacios et al., 2014). This found good agreement in all cases and showed S-A predicting the shock location better than SST (estimating it some $0.05c$ more forward). In one case, small discrepancies near the leading edge suction peak were found, as well as a slight overprediction of pressure over the top surface. The numerical scheme (Roe versus JST) improved the accuracy of the shock location estimation. In the second case, the shock location was predicted perfectly, but in the third, a larger difference was observed. Also, massive detachment resulted in an inaccurate upper surface pressure prediction.

Three-dimensional wings were also tested in SU2 by Palacios et al. (2014). It shows very good agreement between SU2 results and a simulation in DLR’s Tau-code on a DLR-F6. Little (if any) differences were found between SU2 using SST or S-A turbulence models. The SU2 overpredicted C_L in comparison to the experiment by about 5% and at more outboard wing stations, the code had difficulty predicting the correct shock location (again, predicting it too much forward) and (to a lesser extent) shock strength. The close match between the S-A- and SST-models was also found in case of an ONERA M6. In that case, substantially bigger errors were found, showing SU2 struggling with accurately predicting a double shock on the upper surface. Contrary to the F6-case, estimations at inboard stations were now better than at outboard stations. Economon et al. (2016b, p. 841) noted “excellent agreement for the first two-thirds of the pressure signature, but some small discrepancies [...] at the end of the signature” of a Lockheed

Martin 1021 supersonic concept, tested at $M_\infty = 1.6$. Little difference was found between simulations in SU2 and OVERFLOW and wind tunnel experiments conducted on the NASA Common Research Model (Palacios et al., 2015). The discrepancies that were found, mostly concern estimating the shock locations. Compared to experiment, both codes reported higher pressure coefficients on the upper surface. The errors were again largest at outboard sections.

Testing complete UAV-configurations, Vogeltanz (2015) found the numerical scheme to be of important influence. In one test, JST outperformed Roe. Although both schemes overpredicted the lift slope, Roe consistently overpredicted drag and underpredicted lift-to-drag ratios over $\alpha = 3^\circ$. In another test, the results were however reversed. There, JST structurally underpredicted the drag coefficient by some 50%, whereas Roe matched it closely up to $\alpha = 3^\circ$, before deviating to an underprediction of 10%. In predicting lift coefficients, there is no method that clearly outperforms the other – each were found to have their sweet spots in the α -range. The authors hypothesize the Reynolds numbers (first test at $Re = 1.7 \cdot 10^6$; second at $Re = 2.82 \cdot 10^5$) are the main reason for the different accuracy by the two schemes and note testing imperfections (such as wind tunnel asymmetries and small differences in model geometry) might have caused some of the errors between simulated and experimental results.

4.2.6. Comparative review

Similar to the four two-dimensional solvers compared in Section 4.1.5, all but one of the four fidelity levels (discussed in the introduction of Chapter 4) are presented, ranging from simple vortex lattice methods to a panel method and more advanced full potential and RANS solvers. Unsurprisingly, the largest differences are found between these fidelity levels – with commonalities found in different programs of the same level.

Starting with the VLMs (AVL and Tornado), it can be noted that their use cases and applicability are similar. Both are limited to thin wings (or, put differently: neglect thickness) and support modelling bodies (yielding much improved derivatives with respect to the sideslip angle (Martindale et al., 2010)), limited to slender bodies in AVL. Multiple control surfaces can be modelled on each half-wing, just as models can include more than one lifting surface (e.g. a wing and a horizontal tailplane). Both codes include extensive panelling or meshing options. The vortices and wake show some differences. Whereas AVL uses traditional three-part horseshoe vortices and models the wake extending in chordwise direction, Tornado uses vortex slings consisting of seven filaments, allowing the wake to continue in freestream direction. The codes furthermore distinguish themselves in drag estimation, by including user-input viscous polar data (AVL) or estimating parasitic drag based on a semi-empirical method (Tornado). A Trefftz-plane analysis to find induced drag is included in both, but AVL also offers a (often less accurate) computation based on surface forces. Their ability to estimate stability and control derivatives – Tornado using central-differencing, AVL using a parameter sweep – results in extensive use of both programs in control and stability design and analysis, especially of UAVs. Tornado furthermore sees much use in the analysis of morphing structures. In the linear range of the lift curve, predictions of both codes are generally good, but substantial errors can be seen at higher angles of attack. The moment coefficient prediction is further off, possibly due to the fact that viscous effects are not included (Dantsker and Vahora, 2018). Especially in case of Tornado, the results obtained in literature differ a lot, making it hard to validate these beyond the (overall well-predicted) trends. For that reason, AVL seems the more accurate and trustworthy program. Being built in FORTRAN, it is also quicker than Tornado (in MATLAB), although the latter program might be considered more user-friendly.

Compared to the two VLMs, the 3D panel method VSAERO is still linear, but allows for modelling arbitrary bodies (such as wing-body combinations or complete aircraft). This comparison can be seen in Figure 4.11. VSAERO includes two boundary layer methods, one that follows the computed surface streamlines, another which also supports crossflow. Transition is based on empirical methods (instability and transition curves). Despite the relatively small increase in computational cost from the VLM programs, results are more accurate. Earlier versions suffered from inaccurate drag predictions, but with the recent introduction of the Trefftz-plane analysis (also seen in AVL and Tornado), this shortcoming has been resolved. Lift, however, is mostly overpredicted – sometimes by a constant offset, sometimes due to a slightly different lift slope than observed in results from higher-order codes or wind

tunnel experiments. The largest errors are at higher angles of attack, but in the linear range of the lift curve, results are generally good. Especially noteworthy is the improvement of moment coefficient prediction compared to the previous VLM codes. Most problems that are noted in validation or verification results in literature concern the trailing edge region and outboard stations, where separation plays a more dominant role. According to [Strang et al. \(1985\)](#), this is a direct result of the piecewise constant potential and can be solved by increasing the number of panels (increasing computational cost). The linear potential flow model is limited to bounds given by compressibility corrections (Prandtl-Glauert, possibly also Karman-Tsien – different sources provide different accounts) and indeed performs poorer at higher subsonic Mach numbers ($M = 0.8$).

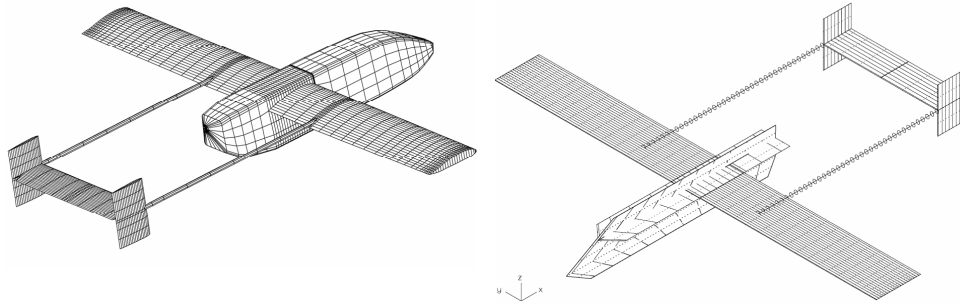


Figure 4.11: Comparison between geometric representations using a 3D panel method (PAN AIR; left) and a vortex lattice method (AVL; right) ([Boschetti et al., 2010](#), p. 5)

Whereas VSAERO has grown popular and widely used, MATRICS-V as well as its inviscid counterpart MATRICS only appear in a few publications. Documentation is also limited. The most important difference compared to VSAERO is the fact that not Laplace's equation, but the full (non-linear) potential equation is used, solved using a finite volume method. This makes the software suitable for analysis of transonic flows. The model is however limited to steady boundary layers and uses empirical (Falkner-Skan) closure relations to solve these equations, hinting that these might be replaced with more physics-based relations in the future. It is unknown whether this change has been made. Similarly, it is unknown if and to what extent transition is predicted. Various sources contradict each other on this topic. The code uses subgrids coupled via a coarser main grid to reduce required computation time. Unfortunately, a direct result of the low number of publications using MATRICS / -V, validation is difficult. The results that are reported (pressure distributions) show generally good agreement and point to the program having some difficulty with accurately predicting the shock location.

Generally most accurate results are obtained with SU2, a combined (Reynolds-averaged or laminar time-dependent) Navier-Stokes and Euler solver, employing finite volume or finite element methods to obtain a solution. Given this choice of flow model, no viscous-inviscid interaction methods are required, yielding a much more integrally physics-based (as well as elegant) calculation. Both the Spalart-Alarmanas as well as the Menter SST turbulence model are included. Despite its novelty, the program has been used extensively for a wide range of analysis and design (which is also supported by the suite) problems in and out of the aerospace community. Generally good results are obtained, with an important advantage of SU2 being its ability to model stall and separation much better than any of the other codes treated in this section. Still, the best agreement is obtained at low to moderate angles of attack. The problems that are observed in literature often concern the prediction of the shock location (SU2 regularly estimates it somewhat more forward) and the pressure distribution over the upper surface, which is overpredicted on more than one occasion. Like VSAERO, accuracy is in most cases lower at sections further outboard than inboard. Results at lower Reynolds numbers are of poorer quality.

Unsurprising, the results show that higher-order CFD tools provide better results than do lower-fidelity codes, or are applicable to a wider range of flow types. In some cases, the geometry or flight conditions under consideration might limit the options to choose from. However, this analysis also shows that higher fidelity comes at a price. First, there is a direct penalty, as most advanced solvers come at an increased computational cost. An inconvenience for a one-time analysis, but an important problem in case of an optimisation study or an analysis over a wide range of conditions. (Given this, it is unsurprising that much

more studies into stability and control characteristics can be found that use a VLM or panel method, than one of the higher-order codes.) Second, there is an indirect price, in terms of requirements on the user and the geometry under analysis. In some SU2 validation studies, the choice of turbulence model or numerical scheme was shown to impact the result. Often only a little, but sometimes substantially. For cases where reference data is not available, the knowledge of CFD-experts is required to properly set up and execute a simulation, making it much more difficult for (conceptual) aircraft designers to perform an analysis themselves.

4.3. Hybrid two-/three-dimensional solvers

This section treats hybrid solvers. This term is used to indicate a combination of a two- and a three-dimensional solver. Oftentimes, the 2D code is used for viscous analysis of the airfoil(s) – something considerably easier than viscous analysis of a 3D object – which is then included in the 3D analysis of the wing or aircraft body. Some hybrid solvers truly combine two (or more) existing codes (such as Q3D, the subject of Section 4.3.2, which adds XFOIL, VGK or MSES to AVL), whereas others (such as XFLR5, treated in Section 4.3.1) have some components developed independently. Any of these ‘base codes’ used in the programs discussed in this section have been treated in full in one of the preceding parts of this chapter. A comparative review of the hybrid solvers treated in this section is provided in Section 4.3.3.

Although both XFLR5 and Q3D are (relatively) recent developments, the technique of combining 2D and 3D models has been used for much longer (e.g. Mouch and Lan (1993), combining ARC2D with a panel code PMARC).

4.3.1. XFLR5

XFLR5 (Deperrois, 2018) is a more recent program than most others treated in this review, having been under continuous development since 2003 (Deperrois, 2003). It adds to the exact codebase of XFOIL a graphical user interface and full wing and aircraft design and analysis tools, based on lifting line theory, vortex lattice method or a 3D panel method. The code assumes linear independence between the viscous and inviscid analyses, such that viscous 2D data can be added to inviscid 3D results to get more realistic results (Meschia, 2008; Dantsker and Vahora, 2018). This assumption especially holds for non-planar geometries, wings with low aspect ratio and wings with high sweep angles (or combinations thereof) (Deperrois, 2011b) and although not theoretically established, this approach has been validated using other CFD codes and wind tunnel experiments (Deperrois, 2011b).

A user manual to the current version is not available, but Deperrois (2011b) provides some documentation for version 6.03 over the program. Based on the release notes (Deperrois, 2003) of the current version (6.42), most of that document pertaining to modelling and solution methods still seems to be valid. Hence, unless indicated otherwise, the information in the remainder of this section is based on that reference.

Two-dimensional solution

As the 2D methods and outputs are identical to those found in XFOIL (but only have been translated from FORTRAN to C++ (Deperrois, 2011b; Rajagopal and Ganguli, 2011)), the governing equations and solution methods for that code, described in Section 4.1.1, also hold for XFLR5.

Three-dimensional solution

XFLR5 encompasses a lifting line method, a vortex lattice method and a 3D panel method. These are treated in this section.

Lifting line method

The lifting line theory incorporated in XFLR5 is a non-linear lifting line method and a strict implementation of Sivellis and Neely (1947) (Deperrois, 2011b; Dantsker and Vahora, 2018). Compared to the linear lifting line theory presented in Section 3.2.1, it works from the notion that the trailing vortices shed from the lifting line generate a velocity component perpendicular to the free-stream direction. This yields an induced angle of attack, which in turn makes the effective angle of attack different from the geometric angle of attack. That same effective angle of attack also depends on the 2D section lift coefficient, resulting in two equations that need to be solved simultaneously. Given the fact that (section) lift curves are non-linear (especially at higher angles of attack), finding a solution becomes an iterative process. Despite this improvement (or rather: extension) compared to the linear LLT, the limitations of the LLT discussed in Section 3.2.1 (e.g., limited to straight wings with $AR > 4$) still hold. XFLR5 however does

take a possible dihedral angle into account when computing the pitching moment coefficient. Wing twist or washout is modelled by adjusting the local angle of attack (Deperrois, 2011b).

Vortex lattice method

The vortex lattice method is a straightforward implementation of the theory presented in Section 3.2.2, with the exception of the option of using ring (or *quad*) vortices rather than horseshoe vortices. In that case, only the vortices located behind the trailing edge extend downwards to infinity, with the vortices on the surface area forming a closed loop, as shown in Figure 4.12a. The (normal) horseshoe implementation is shown for comparison in Figure 4.12b. According to Katz and Plotkin (1991), the ring vortex method is somewhat simpler from a programming point of view. Deperrois (2011b, p. 30) notes that the results of the two methods are “close if not identical in most cases”.

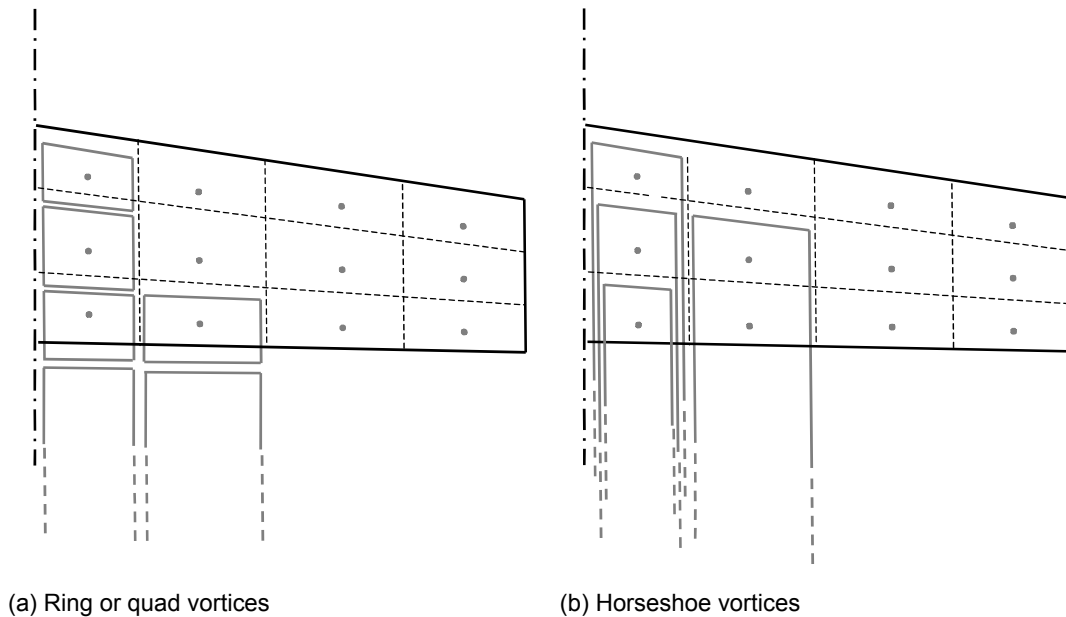


Figure 4.12: Vortex lattice method implementations, adapted from Deperrois (2011b)

As a VLM does not take thickness into account, the vortices are located on the mean camber line at 25% of the panel chord. A control point at which a flow tangency is applied is located at 75% of the panel chord (Deperrois, 2011b). In order to combine the inviscid VLM with viscous 2D airfoil data, the VLM routine first computes the relevant aerodynamic coefficients by integrating the surface forces (at 75% of the panel chord (Rajagopal and Ganguli, 2009)) and then uses the calculated lift coefficient to find a corresponding (possibly interpolated) viscous drag coefficient. Contrary to in the LLT case, twist or washout is modelled as a modification to the wing section, applied at the quarter-chord point. Furthermore, whereas the non-linear LLT allowed for capturing stall, this is not possible in VLM, limiting its results to the (relatively) linear range of the lift slope (Dantsker and Vahora, 2018).

Panel method

As explained in Section 3.2.3, and as is the case in XFLR5, the panel method makes it possible to model the wing as a thick surface. In XFLR5, the 3D panel method is based on the method presented in Maskew and Katz (1987), the VSAERO theory document.

Panels are flat, meaning that all four corners are in the same plane. Singularities (doublets and sources) are positioned on the wing upper and lower surfaces. The wake is also panelled (up to a length 100 times the mean aerodynamic chord), with doublets applied to these panels. The doublet strength is set equal to the difference between the strengths of the upper and lower doublets of the corresponding wing strip, as the wake cannot sustain load. A Dirichlet boundary condition is used (as of version 6.39 (Deperrois, 2003)), as it outperformed the Neumann boundary condition. This sets the velocity potential on the inside

of the surface to 0, equating the internal and (external) freestream potential.

The way the wing is modelled in the current version of XFLR5 depends on whether a single wing or a complete aircraft is analysed. In the former case, the wing is modelled as a thick surface, in the latter case, the fuselage is modelled as a thick surface and the wings are assumed to be thin surfaces. In that case, a vortex lattice method is used to find the aerodynamic properties of the wing, rather than the doublet model proposed in [Maskew and Katz \(1987\)](#).

Output

The 2D output is exactly similar to XFOIL, discussed in Section 4.1.1. Output of the three-dimensional analysis consists of polars (on screen, as well as in the form of data exports), showing combinations of angle of attack or sideslip, force (lift, induced drag, viscous drag, total drag, normal force) and moment (pitch, roll, induced yaw, viscous yaw and total yaw) coefficients. The dynamic pressure and transition location is also available. Stability derivatives are not automatically computed, but can be generated if the wing mass and inertia are specified.

Results

As the 2D analysis uses XFOIL, critiques shared on the viscous results by that program, discussed at the end of Section 4.1.1, of course also hold for XFLR5. These concern problems with predicting separation and under-prediction of the drag coefficient of thicker airfoils. Some studies only use the 2D capabilities of the program ([Müller et al., 2012](#)), possibly because the graphical user interface that XFOIL itself is lacking. Many of the use cases include UAVs or MAVs ([Hassanalian and Abdelkefi, 2017](#)), enthusiast projects (especially sailplanes, ([Meschia, 2008](#))) and stability analyses ([Kurukularachchi et al., 2016](#)).

Looking at the complete program, numerous publications comparing XFLR5 results with data from higher-fidelity methods or wind tunnel campaigns show experimental trends are generally matched ([Deperrois, 2011b](#)). Drag is underestimated in multiple cases ([Deperrois, 2011b, 2009; Deepa et al., 2016](#))¹⁹, possibly due to the 2D-to-3D extrapolation. Lift predictions were found to be similar to experimental and other computational results ([Dantsker and Vahora, 2018](#)), with [Deperrois \(2009\)](#) having obtained the best estimates with the LLT-model. [Council and Goni Boulama \(2008\)](#), having compared XFLR5 to DNS-results, furthermore observe overpredictions of lift values, especially at higher angles of attack ($\alpha \geq 4^\circ$). The panel method is best in predicting moment trends. From these results, it was concluded that the LLT-method is best for lift prediction and the VLM for all other predictions, showing at least as good results as the panel method ([Deperrois, 2009, 2011b](#)). Especially at higher angles of attack, the panel method loses accuracy ([Deperrois, 2009](#)). Another publication compared phugoid and Dutch roll characteristics to AVL and experimental data (again from a sailplane model), noting inconclusive results ([Deperrois, 2011a](#)). All in all, XFLR5 gives a “fairly accurate idea on the aerodynamic characteristics of the configuration” ([Deepa et al., 2016, p. 9](#)), furthermore noting that its accuracy “coupled with its ease of use and speed” make it an “effective tool for preliminary analysis of any design”.

4.3.2. Quasi-three-dimensional aerodynamic solver (Q3D)

Q3D, short for *quasi-three-dimensional aerodynamic solver*, was born out of the need for an accurate as well as fast method for conceptual wing design and evaluation and developed at Delft University of Technology ([Mariens, 2012; Mariens et al., 2014](#)). It combines two-dimensional viscous airfoil data (from a 2D solver) with an inviscid three-dimensional method (AVL) in order to evaluate full wing aerodynamic forces, similar to [Cosyn and Vierendeels \(2006\)](#).

A user manual is not available. As such, the remainder of this section is based on the original publications ([Mariens, 2012; Mariens et al., 2014](#)).

¹⁹[Deperrois \(2009\)](#) used XFLR5 v4.09, which employs a near-field drag estimation method. From v4.13, a far-field analysis is done ([Deperrois, 2011b](#)). As such, the it is unsure to what extent these results reflect the performance of current versions of the program.

Two-dimensional solution

What tool is used for the two-dimensional analysis depends on the flow regime. In subsonic flow, XFOIL (version 6.97) is used, whereas in transonic flow, use is made of either VGK or MSES. As the latter is based on the Euler equations it is more accurate in case of shocks, but this capability comes at an increased computational cost.

In any case, the 2D analysis is performed on a wing section normal to the sweep line (Mariens, 2012, pp. 44-45).

Three-dimensional solution

AVL is used for the three-dimensional analysis. As the details of that program are treated in Section 4.2.1, they are not repeated here.

Solution procedure

As Q3D combines various other programs, it does not add any new flow modelling equations, instead, it solely adds a way to combine the 2D and 3D information (Mariens, 2012; Mariens et al., 2014).

1. The spanwise lift distribution (for a particular angle of attack α and 3D lift coefficient C_L) is computed using AVL. Induced drag is calculated using a Trefftz plane analysis.
2. Aerodynamic characteristics of various 2D wing sections are computed using an extended form of strip theory (also known as the blade element method (Mariens, 2012)) in the following manner:
 - (a) The lift distribution obtained in step 1 is interpolated to find the local lift coefficient (c_{l_∞}) at a specific section. This will be used for subsonic wing analysis.
 - (b) The chord-wise geometry and aerodynamic characteristics per section (“freestream”) are translated to geometry and aerodynamic characteristics normal to the sweep line (or shock line) (“normal”). In this transformation, taper is also taken into account. The resulting parameters are used for transonic wing analysis.
 - (c) The induced angle of attack is determined. Based on an initial assumption for α_i , the effective C_L , Mach and Reynolds number values are computed from the values normal to the sweep or shock line. These are subsequently fed to an airfoil analysis tool (depending on flow regime), which outputs values for effective angle of attack and drag coefficient. From geometry, an updated induced angle of attack can be computed. This process is iterated until the value found for induced angle of attack has converged.
 - (d) With the induced angle of attack obtained in step 2c, the effective drag coefficient can be translated into a normal drag coefficient, consisting of a profile (friction and pressure drag, including wave drag) and induced drag component. The latter is neglected (as this will more accurately – far-field rather than near-field analysis – follow from the VLM), the first (viscous) component is taken on to the next step.
 - (e) The friction and pressure drag coefficients are translated back into a freestream drag coefficients.

The profile drag coefficients are integrated over the span to yield a 3D profile drag coefficient.

3. The 3D profile drag coefficient in step 2 and the induced drag coefficient computed in step 1 are then summed to find the total wing drag coefficient. The lift coefficient from step 1 is accepted as the wing lift coefficient.

As the authors also note, the panelling (for the VLM) and sectioning (for the blade element method) have an impact on the situation. Based on multiple analyses with varying grid sizes, Mariens (2012) concluded 24 spanwise and 13 chordwise panels are sufficient for the VLM calculations, and 8 wing sections are sufficient for the strip theory (Mariens et al., 2014). It is unclear whether these values are optimal irrespective of geometry size.

Output

As Q3D was not available in the period this literature study was conducted, no information on the type and format of the output generated by the code is available at this time. It is however deemed likely that the 3D information largely follows the AVL output format, with 2D data output closely resembling information content and formatting by the viscous analysis code utilised.

Results

Results obtained with the program described here²⁰ at both low and higher speeds, comparing the performance of Q3D to VSAERO and (in the transonic case) MATRICS-V, are described by [Mariens \(2012\)](#) and [Mariens et al. \(2014\)](#). At lower speeds, lift was found to be slightly overpredicted compared to experiment (caused by AVL, according to [Mariens \(2012\)](#)) in a consistent fashion, leading to the hypothesis that a fixed-value correction might be used to improve the accuracy. In contrast, drag was under-estimated. The error was largest at lower or negative angles of attack and a more detailed comparison with MATRICS-V showed Q3D predicting profile drag too high and induced drag too low – the latter increasingly so at higher angles of attack. This is shown in Figure 4.13. [Mariens et al. \(2014\)](#) found no consistent under- or overprediction of drag, with average errors limited to 1%. In that study, the induced drag was found to be predicted very well, with profile drag being overpredicted (as in [Mariens \(2012\)](#)) and skin friction drag underpredicted. This might be explained by the fact that Q3D estimates transition to take place a little more downstream than MATRICS-V, resulting in a larger part of the boundary layer being laminar, associated to lower drag.

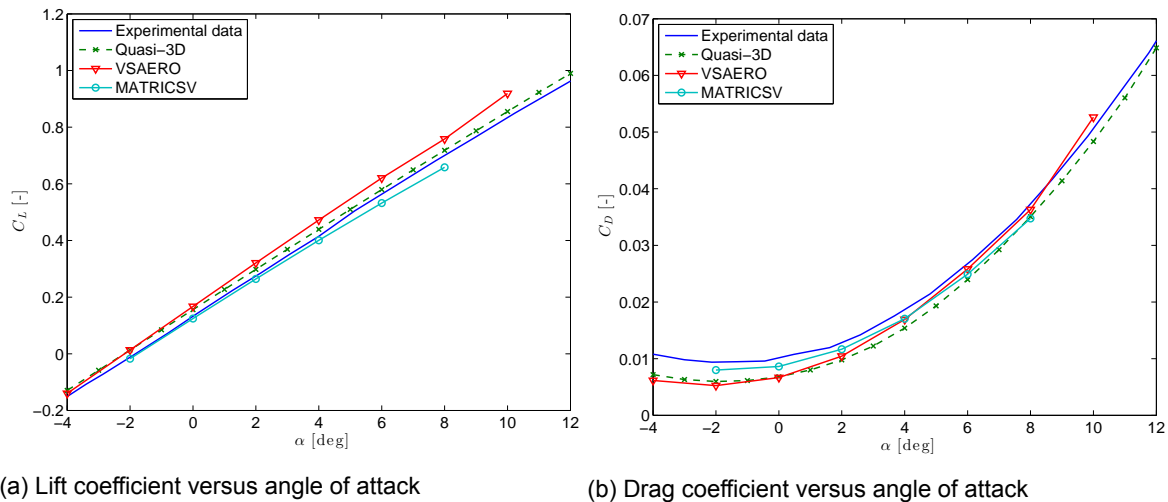


Figure 4.13: Comparison of aerodynamic coefficients for a NACA 24-30-0 wing at subsonic speed as predicted by Q3D, VSAERO and MATRICS-V and found in experiment, illustrating Q3D performance ([Mariens, 2012](#))

Transonic performance was validated as well, with fixed transition at $0.05c$. Q3D using MSES found a slight overprediction of drag coefficient up to $M \approx 0.75$, turning to a substantial underprediction in the transonic regime (further increasing with growing Mach number). This last observation is consistent with data presented in Section 4.1.3. The behaviour is more clearly visible at higher C_L -values. The results obtained using Q3D with VGK are largely consistent with the data from Q3D-MSES at subsonic speeds, but VGK performs better at higher Mach numbers. Shock locations are predicted best at mid-span sections of the half-wing by both 2D codes. The shock location is estimated too much forward near the root and too far rearward near the tip when compared to MATRICS-V, most likely due to the inability of Q3D to model 3D root and tip effects. Similar to in the lower Mach regime, Q3D (regardless of the 2D solver) overpredicts C_L at a given α in transonic flow. Overall, the error is limited to 2% compared to MATRICS-V, as long as the freestream flow velocity does not surpass the drag divergence Mach number ([Mariens et al., 2014](#)).

²⁰Another Q3D-method, proposed by [Elham \(2015\)](#), is discussed in e.g. [Elham and van Tooren \(2016\)](#) and [van den Kieboom and Elham \(2018\)](#). This extends the current tool using MATRICS-V to further improve the drag estimation.

4.3.3. Comparative review

Despite the fact that XFLR5 and Q3D are both codes in a relatively small niche of aerodynamic solvers and the accuracy of their results does not seem vastly different, there are a number of important distinctions. Most prominent is the fact that Q3D, owing to its inclusion of 2D viscous solvers VGK (Section 4.1.2) and MSES (Section 4.1.3), is able to generate a reasonable estimate of aerodynamic quantities of interest at higher subsonic Mach numbers. Accuracy is substantially worse when compared to speeds below $M \approx 0.75$, but XFOIL – on which XFLR5 is based – is overall limited to Mach numbers lower than 0.7. Interestingly, Q3D coupled to VGK provides more accurate results than when paired to MSES at higher speeds, even though MSES was designed for a wider Mach range. Consistent with the individual reviews of these latter two solvers, Q3D has difficulties with accurately predicting the shock location. This is most notable at the root and tip, where 3D effects not modelled by Q3D, play a role.

Another contrast is the fact that Q3D performs all three-dimensional calculations using AVL (a VLM), whereas XFLR5 provides users the additional option of choosing a lifting line theory or panel method computation. This difference is less relevant in practice than it might seem in theory, as the overall best results in XFLR5 are obtained when the VLM is used. An exception to this is the notion that [Deperrois \(2011b\)](#) documented slightly more accurate lift predictions were obtained using LLT. The panel method adds little value.

As stated previously, reasonable to good accuracy is obtained using both programs, although much less validation cases were available for Q3D than for XFLR5. From the results, it shows XFLR5 underpredicts drag and slightly overpredicts lift and Q3D follows these trends, with somewhat larger errors in lift prediction. [Mariens et al. \(2014\)](#) hypothesise the discrepancy in drag coefficient is caused by a slight error in the prediction of transition location. This might also play a role with XFLR5, as many of the 2D analysis tools share the same methods for estimating transition. Q3D performs better at lower speeds than at higher speeds, with the overall error (in comparison to MATRICS-V) reducing from 2% to 1%.

5

Applicability to conceptual design

The previous three chapters presented various (types of) flow models, solution methods and aerodynamic solvers – at varying levels of fidelity. It will come as no surprise that each flow model and associated solution method has its own place during the aircraft design process. Some lower-fidelity models might not provide the answers aerodynamicists are looking for in more detailed design phases, whereas computationally expensive RANS simulations might be too slow and costly for use in conceptual design (Mariens et al., 2014). Thanks to the advances made in computer technology and processor speed, however, computational limitations are not as limiting as they once were. Especially with respect to the conceptual design phase, this results in heated discussion: does the fact that we *can* also mean we *should* use higher fidelity models in early design?

This chapter aims to answer that question – or at least present arguments from different sides of the debate. As conferences and publications show, it has not yet been settled. First, arguments in favour of early use of higher fidelity models are treated; followed by arguments against. Then, some barriers are discussed that stand in the way of successful implementation of these more advanced methods. Last, the debate is summarised and a conclusion is drawn, providing a solid foundation for selecting which solvers will be subject of the thesis work succeeding this present report.

Higher fidelity models are a key design technology

Proponents of using higher fidelity models in early design phases name three arguments. First of all, researchers feel that it is a “key design technology” (Sinsay and Nuñez, 2010, p. 1) for preventing cost and schedule overruns, by reducing risk and uncertainty early on (Kroo, 2004; Carty, 2002). Second, Ciampa et al. (2013) note that empirical or lower-order models might not be suited for analysis of new technologies and novel configurations, that have to be evaluated using physics-based models. Third, scholars see it as a necessity for making early multidisciplinary design optimisation (MDO) possible (Suwarantana and Rodriguez, 2011; McMasters and Cummings, 2004; Carty, 2002; Jameson, 1999). Performing MDO-studies before major decisions are made provides more design freedom to the optimiser and might allow exploiting synergies that would have otherwise been left unused. Also, Gu et al. (2018, p. 12) expect this to “minimize the redesign activities” later on.

Higher fidelity models transform conceptual design into detailed design

This expectation is exactly opposite of Raymer’s outlook (Raymer, 2002). He argues that if, for example, not all regulations and requirements are properly implemented in the computer system, its proposed configuration might need substantial manual adjustments that result in a design “different from and probably worse than” what the optimiser proposed (Raymer, 2002, p. 35). Including all these details in the optimiser takes additional time and furthermore makes the software less generically applicable, such that development costs (time and money) can no longer be spread over an entire aircraft portfolio.

In his doctoral dissertation (Raymer, 2002), he further raises some more fundamental critiques, articulating that some detailed information (e.g. airfoil shapes) required for proper high-fidelity (CFD) analysis simply has no place in conceptual design, which focuses on determining parameters like the twist and camber distribution. Including these additional parameters would essentially transform the conceptual design process towards a preliminary or even detailed design effort. He argues that optimisation efforts in this first design phase should focus on higher-level parameters, such as wing loading and major plan form parameters (fuselage fineness and wing aspect ratio, for example). In later stages, when the design becomes more detailed (including thickness distributions of structural members, for example), optimisation can also focus on more detailed aspects of the design (such as the aforementioned airfoil shapes). In the opinion of Raymer (2002, p. 17), “everything-optimization” is not only infeasible, but also undesirable, as it takes up a lot of time (setting up and executing an optimiser and understanding its results) that is much better spent on exploring other or additional design alternatives. Fitting with that the remark “[i]t may be hard [...] for engineers to interpret the huge volumes of data generated by these methods in a way that will provide them with the insights needed to enable better designs” Jameson (2003, pp. 6-7). Although this concern was voiced about anticipated increased use of LES and DNS in aircraft design in general, the principle can be easily translated to conceptual design.

An argument that was not uncovered in the (aeronautical) literature reviewed but that the present author feels important to mention is the possibly false sense of security or accuracy provided by more detailed output of higher-fidelity analysis models. This can be likened to information bias, in which it is felt that more information is better. Pro-innovation bias (newer is better, overvaluing of the usefulness of something, while under-appreciating its costs) and zero-risk bias (aiming to prevent uncertainty at all cost) also come to mind as possible risks or downsides.

Barriers for higher fidelity models in conceptual design

The barrier of lengthy set-up processes and computationally expensive runs is also voiced in a group of publications that seem not yet determined on an answer to the question raised in the introduction of this chapter. Sinsay and Nuñez (2010), for example, signify that only very few conceptual designs ever see the light of day and pose the question whether it is cost efficient to invest so much computational effort in high risk design attempts. Cummings et al. (2015, p. 265) state that lower-fidelity, linear methods “can be invaluable in conducting conceptual design trade studies to begin the process of identifying feasible aircraft configurations”.

Sinsay and Nuñez, as well as Ghosh et al. (2014), Gu et al. (2018), Suwarantana and Rodriguez (2011) and Haines and Drela (2012), however observe a more fundamental barrier for implementation of higher fidelity models in conceptual design, noting that higher fidelity analysis tools require higher fidelity design input, such as a precise definition of the aircraft wetted area. Without these, quality of the analysis will be severely compromised. (As the saying goes: garbage in, garbage out.) As discussed, however, this detailed geometric information is not always available during conceptual design (Raymer, 2002; Jameson, 1999), nor is it easy to generate in that phase. Conceptual designers are often not well-enough equipped to handle the CAD-software to produce these detailed geometries. One might solve this problem by including specialists to make the CAD-models, but this potentially slows down the conceptual design process and introduces the risk of miscommunication (between designer and CAD-specialist), resulting in models that do not represent what the designer (or design team) had in mind (Suwarantana and Rodriguez, 2011). Even if CAD-proficiency grows and specialists might no longer be required, current drafting-based methods make it difficult to make even simple adjustments – of which there will be many during conceptual design – to a model. This is wonderfully illustrated in the top half of Figure 5.1. This difficulty results in high cost or a premature design freeze to prevent these costs, but putting an immediate halt to all design work (Suwarantana and Rodriguez, 2011). Regeneration of grids further adds to the cost (Raymer, 2002).

These problems might be (partially) solved with parametric design methods and tooling, which allow geometries to be adapted more easily (as shown in the lower half of Figure 5.1) and might require less operator skill (Belie, 1993; Haines and Drela, 2012; Carty, 2002; Koning, 2010; Suwarantana and Rodriguez, 2011; Giesing and Barthelemy, 1998; Jameson, 1999). However, even then the process should be able to keep up with the pace of conceptual design (Suwarantana and Rodriguez, 2011). Parametric

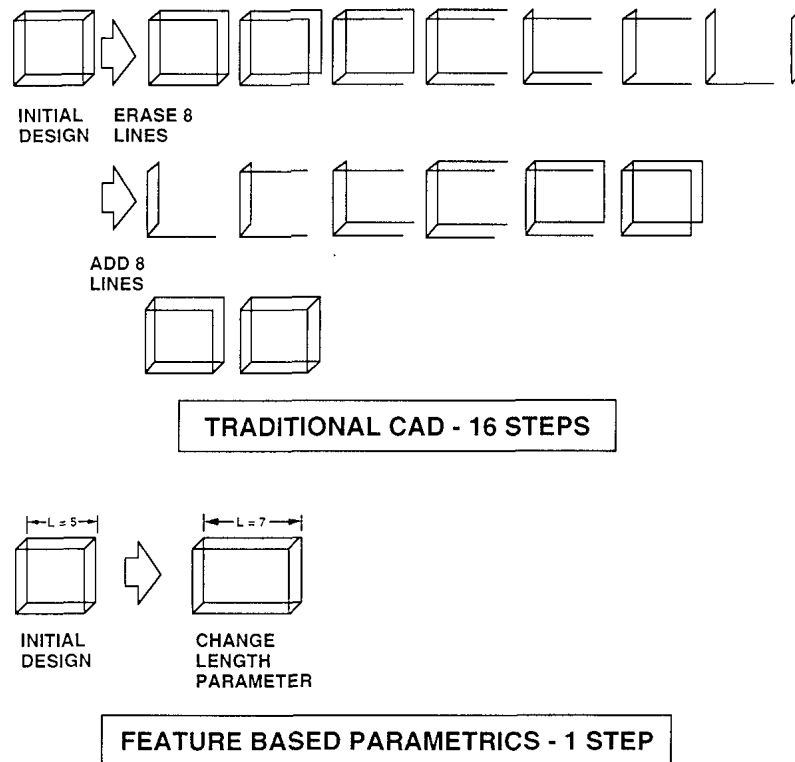


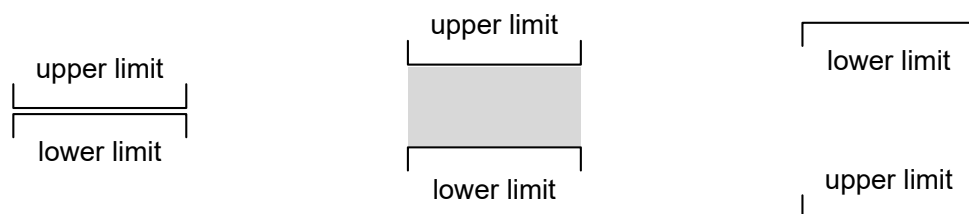
Figure 5.1: Traditional (drafting) versus parametric design, illustrating the incompatibility of drafting with automated design (Belle, 1993, p. 5)

design tooling could even fully close the loop, such that automated design, analysis, (multidisciplinary) optimisation, re-design and iteration can be achieved. Although various authors have proposed such tooling, industry application is still low (Haines and Drela, 2012).

Right fidelity

Sinsay and Nuñez (2010) make that the present author feels is one of the most compelling arguments in this discussion by introducing the term *right-fidelity*, making the question of “what is the right tool for the job?” explicit. Sinsay and Nuñez (2010, p. 4) define right-fidelity as “where the band of uncertainty is small enough to definitively distinguish between concepts” and note that it is impossible to universally define what ‘right’ is.

Given the arguments presented earlier in this chapter, it is proposed to see right-fidelity as a lower limit to guide the selection of minimum fidelity level. Time and cost available can be used as upper limits. This yields three possibilities, as visualised in Figure 5.2 and discussed below.



(a) Lower limit equal to upper limit (b) Lower limit above upper limit (c) Lower limit below upper limit

Figure 5.2: Possible combinations of lower and upper fidelity limits

- **Lower limit is equal to upper limit** (Figure 5.2a)
If the lower and upper limits are equal, the limits readily give the fidelity level.
- **Lower limit is above upper limit** (Figure 5.2b)
If the lower limit is above the upper limit, the problem is 'underconstrained'. In this case, it is proposed to set the fidelity level at the lower limit, saving cost.
- **Lower limit is below upper limit** (Figure 5.2c)
If the lower limit is below the upper limit, no applicable fidelity limit can be found. Here, it is proposed to either postpone the analysis or selection to a later design stage, or to separate the analysis from the main design process. In both cases, the upper limit (dictated by time and cost constraints) can be set higher.

Especially given the high model requirements made by more advanced analysis, the upper limits will often be fairly stringent. This even more so holds for conceptual design.

The different combinations displayed in Figure 5.2 indeed make it impossible to universally select what (kind of) solvers are and what (kind of) solvers are not suitable for application in conceptual aircraft design. However, if the lower limit dictates the use of solvers using flow models from fidelity level L3 (time-dependent and Reynolds-averaged Navier-Stokes equations, as shown in Figure 2.1), a postponed or separated analysis is likely most applicable. This also goes in case three-dimensional solvers using flow models from level L2 (Euler equations) or the intermediate level L2.5 (thin-layer Navier-Stokes and boundary layer equations) are required. The rationale of limiting this restriction to three-dimensional solvers is the higher computational cost and the difficulties in modelling various three-dimensional effects in boundary layer models. Hybrid methods are viewed as an excellent way of including relevant (two-dimensional) viscous effects in three-dimensional analyses.

6

Conclusions

This literature review set out to provide an overview of aerodynamic flow models, mathematical solution methods and aerodynamic solvers, and discuss the applicability of these to aircraft conceptual design. The insights obtained are to serve as foundation for a subsequent graduation research project into uncertainty quantification of aerodynamic models used in conceptual design.

Starting with the aerodynamic models that describe the flow and its characteristics, it was established that the insurmountable computational cost of the most advanced models (the time-dependent Navier-Stokes equations) makes these inappropriate for application during any stage of (industrial) aircraft design. Aiming to reduce the computational cost to manageable proportions, it was found that either assumptions can be made to simplify the flow model, or physical models can be (partially) traded for empirical relations. The former track yields (in order of decreasing accuracy or *fidelity level*) the inviscid Euler equations and the irrotational (full) potential equation, followed by either the linearised potential equation (assuming small disturbances) or Laplace's equation, which is inherently linear and assumes incompressible flow. The latter and increasingly empirical track includes various ways of resolving or modelling the Navier-Stokes equations (direct numerical simulation, large eddy simulation and unsteady and steady RANS), the thin-layer Navier-Stokes equations and the classical boundary layer equations. The latter can be coupled to an inviscid solution using viscous-inviscid interaction methods, allowing an analysis that describes the flow domain inside as well as outside the boundary layer.

In case of a linear flow model, a complete solution can be found by finding a (linear) combination of various elementary solutions, 'fixed' by the boundary conditions that are applied to it (such as the flow tangency condition). Multiple methods exist, that mostly differ by the extent to which they can model geometric features. Lifting line and lifting surface theory, as well as vortex lattice methods, are limited to thin wings. Panel methods, on the other hand, are able to represent thickness. Non-linear methods, being finite difference, finite element or finite volume methods, solve the flow model on a particular type of grid. FDM are oldest and most traditional, and are limited to structured grids. FEM and FVM grids do not need to be structured, but are more complex and (especially in case of FEM) are deemed more difficult to understand. Again, (far-field and surface) boundary conditions are used to find the solution applicable to the particular situation under investigation.

Combining flow models and solution methods yields solvers, of which 11 have been analysed. Suitable for two-dimensional airfoil analysis are XFOIL, VGK (viscous Garabedian and Korn), MSES and ARC2D (Ames Research Center 2D); aimed at three-dimensional analysis are AVL (Athena Vortex Lattice), Tornado, VSAERO (Vortex Separation Aerodynamics), MATRICS / -V and SU2 (Stanford University Unstructured) and a combination of two- and three-dimensional 'hybrid' solvers is found in XFLR5 and Q3D (quasi-three-dimensional aerodynamic solver). They are visualised in Figure 6.1. Besides showing what flow model(s) and solution method(s) are incorporated in each of these solvers, the figure shows the fidelity level of the flow models and some characteristics of the codes.

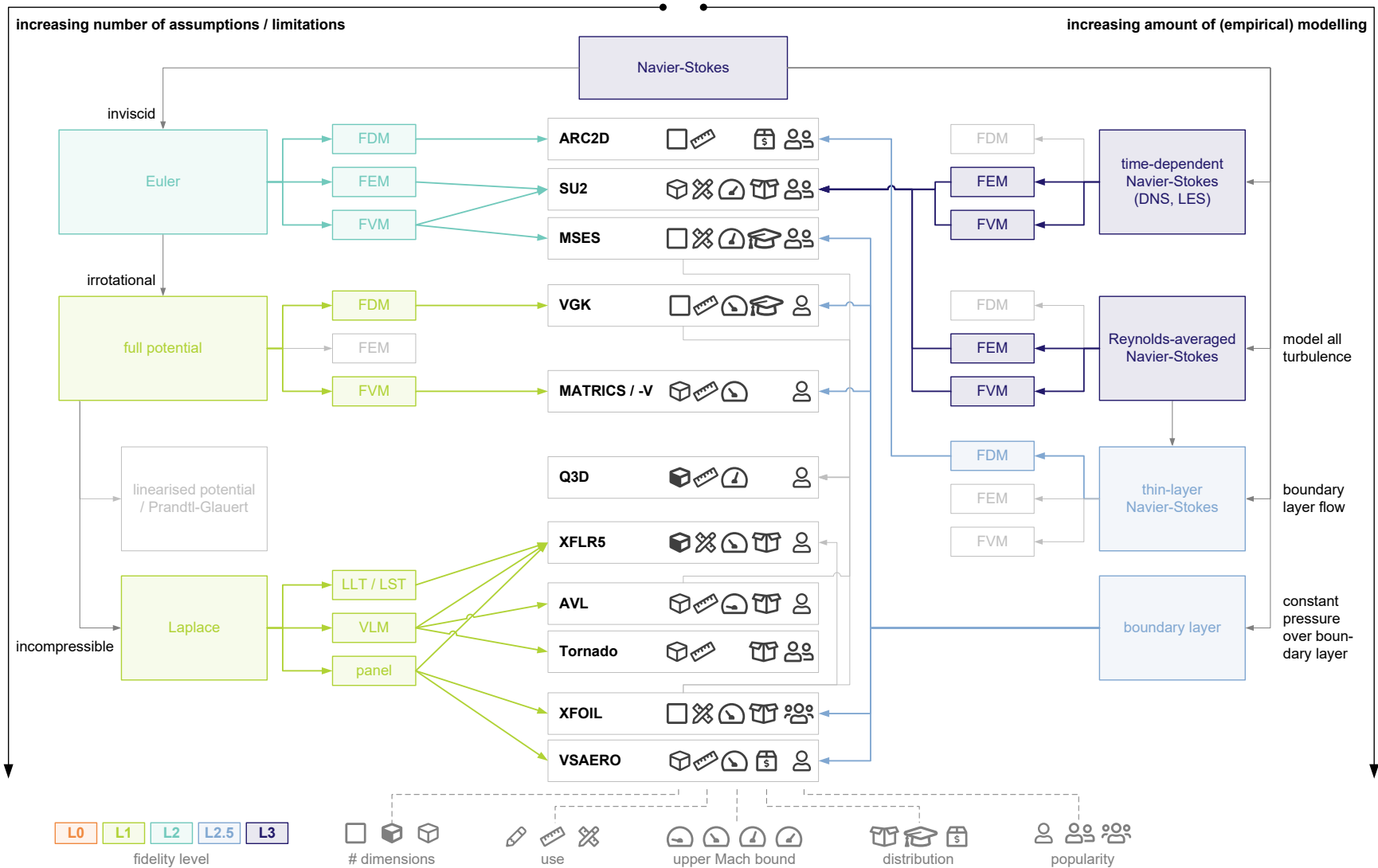


Figure 6.1: Hierarchical overview of aerodynamic solvers. Larger-size versions available through bram.peelings.me/en/literature-study/ using password "AE4020-2018"

Based on the reviewed literature comparing computational and experimental results, it can be concluded that higher-fidelity codes yield most accurate flow predictions. Despite this fact, it is too easy to always argue the “bigger is better” case. Of the 2D codes, for example, only XFOIL and MSES are able to predict transition, and MSES was sometimes found less accurate in parts of the Mach regime where other solvers (XFOIL and VGK) are also applicable. Furthermore, VGK accuracy improves with increasing Reynolds number, whereas the opposite was found to be true for XFOIL and MSES. Errors are attributed to the transition model (e^n envelope method) in case of XFOIL and MSES and to the turbulence model in case of ARC2D. All solvers struggle with accurately predicting the location and strength of shock waves. Largely because of the differences in geometry modelling features of the 3D codes, performance and quality in this case is more closely correlated with fidelity level. AVL was found to be more accurate and trustworthy than Tornado, but (also because of the possibility of modelling viscous flows) VSAERO, MATRICS-V and SU2 outperform these VLM codes. All programs however struggle with accurately predicting separation to a greater or lesser extent, which especially influences accuracy at higher angles of attack. In a comparison of the hybrid solvers, it was found that both yield results having reasonable to good accuracy.

Especially in a time- and resource-constrained process as aircraft conceptual design, there are more requirements than performance and possibility. It was found that whereas some solvers are very well documented and often used (yielding a lot of validation results and reference applications), others are only seldom employed and have their inner workings spread out over a multitude of publications. More importantly to the decision maker in industry is the fact that higher-fidelity codes always come at an increased computational cost, in terms of computer time as well as due to higher input-quality requirements. Besides this objective difference, it was concluded that scholars also disagree philosophically. Whereas some see early application of higher-fidelity model as enabler for technologies (such as early MDO) that will cut cost and reduce risk, others feel that conceptual design should be that: conceptual, explorative and iterative, and dealing with high-level parameters. In conclusion, it is proposed to use the lowest-fidelity model that is able to definitively distinguish between two designs. If the cost of using a model of that fidelity level is too high, it is felt the decision can better be postponed to a later design stage (in which more resources are available) or be separated from the primary design process.

7

Discussion

Even though all research questions and goals set forward in the introduction have been answered and achieved, it is relevant to reflect on these results. That is done in this chapter – divided into two sections. Section 7.1 discusses limitations of this review; Section 7.2 lists a number of recommendations for the future. These recommendations are on a fairly high level and are aimed at further improving the field of computational aerodynamics, both with regard to research efforts and to industrial application. An outlook to the proposed graduation research project following this literature study is not included in this chapter, but given its own and follows as Chapter 8.

7.1. Limitations of current research

Besides the fact that some flow models, solution methods or solvers are not treated (or only shortly mentioned) in this literature review, there are a number of limitations to this research.

First of all, and unsurprising for a literature study, all information presented here is based on published literature. This means that all source material is at best ‘second hand’, possibly third or fourth. The academic peer review process of course is a guarantee for the quality of the referenced works, but this can hardly be absolute. Point in case are a few instances where conflicting information was found, for example on the workings of a solver code. In situations as these, the most reputable source (determined based on e.g. best-known author, most closely affiliated to the program being discussed or most citations) was used and footnotes that show (and possibly explain) the conflict were included. Also related to this is the fact that only public or academic resources were used, as possibly more recent user manuals to commercial software were unavailable during this project. Still, it is possible this causes some information in this report to be (partially) out of date. All these cases have been indicated in the text.

Second, the current author feels the need to mention he is mostly self-taught in the topics treated in this literature review (such as computational fluid dynamics, viscous flow modelling and numerical schemes) – largely so as a result of writing this very text. Still, it is possible that some nuances might have been deemed less relevant than they truly are and therefore left out of this report, or vice versa.

7.2. Recommendations for future research and development

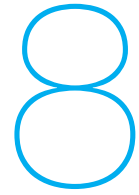
Having completed this literature review, the present author feels there are three important ways in which the field of computational aerodynamics can be further improved.

A first opportunity for improvement is to tackle the problem of inaccessible, unstructured and inconsistent documentation of some aerodynamic solvers. Students, researchers and industry professionals use

these tools and should be able to easily identify the inner workings of a black box. Only that understanding can guarantee that tools are only used in a situation where they are applicable and valid and that tools are used in the right way. This can be as simple as a clear definition on what a “low” Reynolds number exactly is, or as complicated as what compressibility correction or closure relation is incorporated in a particular piece of software. It was found that these aforementioned issues are mostly observed in open-source software, such as with XFOIL, MSES and AVL. In contrast, VGK and to a lesser extent also VSAERO, come with a wealth of reports extensively documenting not only its use, but also the underlying theory. The structured development of SU2 – to which a large amount of researchers around the world contribute, but which is still organised and documented well – nonetheless shows this goal can be achieved.

Related to the previous recommendation is the second one: to stimulate structured analyses and reviews of results obtained using particular aerodynamic codes. Cited in this report are a host of publications comparing solvers, but meta-reviews bundling a number of these publications have not been found. In contrast, the Cochrane library provides professionals in health care with systematic reviews aimed to “identify, appraise and synthesize all the empirical evidence that meets pre-specified eligibility criteria to answer a specific research question” ([Cochrane Library, 2018](#)), promoting evidence-based practice. It is felt that both end users as well as developers of aerodynamic codes could benefit from such practise, since it can both identify the most suitable tool for the job and highlight differences that might inspire further development.

The third and final recommendation is to maintain and further stimulate the development and use of standard validation cases, as are for example established in AIAA workshops (e.g. [Maksymiuk and Pulliam \(1987\)](#)). This decreases the effort with which various codes can be compared – with each other and with experimental results. This recommendation is consistent with [Pulliam et al. \(1983\)](#) proposing using a number of airfoils as standard test cases.



Research outlook

This chapter looks ahead to the graduation research project for which this literature study forms a basis. The research will address the challenge of making better decisions in aircraft conceptual design. As the project integrates Aerospace Engineering and Science Communication, the topic will have two focus points. One perspective is mostly technological and sets out to develop a methodology for uncertainty quantification in (aerodynamic) models used in conceptual design. Another is largely socio-psychological, investigating ways how to properly assess the uncertainty, how to make better decisions using that information and how to better support that decision making process. The entire research project will be focused on technology assessment in the context of Project MANTA using the Aircraft Design Initiator – a conceptual aircraft design tool developed at Delft University of Technology.

Given the topic of this literature review, this chapter is concentrated on the technological perspective. Section 8.1 presents the proposed research goal and research question, followed by Section 8.2 discussing the methodology. Section 8.3 shows a planning of the research to be carried out.

8.1. Research goal and questions

The goal of the research project is to make a contribution towards providing decision makers with a usable assessment of epistemic model uncertainty of the Aircraft Design Initiator and the impact thereof on its output, by developing a bottom-up methodology to quantify model uncertainty in aircraft conceptual design, by studying the effects of different assumptions on relevant model output of various aerodynamic analysis methods relevant in the conceptual design phase.

The proposed research question and sub-questions are defined as follows.

How can model uncertainty be quantified, assessed and propagated bottom-up, i.e., starting from model(ling) assumptions, simplifications and limitations?

- a. Which (kind of) flow models, solution methods and combinations thereof (i.e. solvers) are suitable for aerodynamic analysis in a conceptual design process
- b. Which criteria are relevant for the comparison of different (aerodynamic) analysis models in a conceptual design process?
- c. What assumptions, simplifications and limitations are associated to these models, solution methods and solvers and what (predictable and unpredictable) uncertainties in the model output do these introduce?
- d. How do different (types of) model uncertainties propagate through the Aircraft Design Initiator, thereby (possibly) influencing the output uncertainty?

Research question *a* has been answered by this literature review, as well as the first part of research question *c*.

8.2. Methodology

In order to answer the research questions and achieve the research goal, the following methodology is proposed. This heavily builds upon the information presented in the current report and contains three major steps, dealing with uncertainty quantification, uncertainty propagation and methodology validation.

Uncertainty quantification

The influence of particular assumptions and simplifications will be investigated by comparing the results of a number of aerodynamic analyses by four two-dimensional solvers: XFOIL, VGK, MSES and ARC2D. Depending on research progress, 2D Euler-simulations using SU2 (using a FEM and/or FVM) can be added, in order to try to isolate the influence of non-linear solution method. The choice to start with two-dimensional solvers is based on their easier flow models, given that 3D-effects are not included. Also, the current selection of codes is felt to be better available as well as better documented than an equivalent set of 3D solvers. This experiment aims to answer the second part of research question *c*. Relevant criteria for comparison (research question *b*) will be established prior to starting the experiments. Based on the publications reviewed in the current report, most attention will most likely go to pressure distributions and polars of lift, drag and pitching moment coefficients.

Which assumptions or modelling differences can be investigated using which comparison of codes is shown in Table 8.1. The numbering indicates prioritisation, concentrating on establishing the influence of differences between flow models rather than solution methods. The suffixes *i* or *v* that are added to the case number indicate whether the comparison will be viscous, inviscid or both.

Table 8.1: Prioritised testing matrix, showing which insights about assumptions or modelling differences are gained from comparisons

	VGK	MSES	ARC2D	Euler-SU2
XFOIL	1-i: incompressible flow 5-i/v: panel vs. FDM	4-i: incompressible, irrotational flow		
VGK		2-i: irrotational flow		
MSES			3-v: BL vs. TLNS 6-v: FVM vs. FDM	
ARC2D				
Euler-SU2				7-i: FVM vs. FEM

The desire to also compare computational results with experimental data drives the choice for geometries and flow conditions, for which the viscous transonic airfoil (VTA) workshop, associated to the AIAA 25th Aerospace Sciences Meeting, will serve as a basis (Holst, 1988; Maksymiuk and Pulliam, 1987). Two well-known reference airfoils will be investigated: the symmetrical NACA 0012 profile and the supercritical RAE 2822 airfoil. A third airfoil will be selected later on, depending on a research focus into either wingtip devices or morphing trailing edges (two research interests in Project MANTA). Corresponding to the VTA results, the airfoils will be tested at freestream Mach numbers of 0.55 and 0.799. Added to that is a test case at a lower speed, $M_\infty \approx 0.3$ – the limit of the incompressible flow assumption. As not all solvers support transition modelling, this will be forced at a given chordwise position. A benefit of partially replicating the VTA results is the availability of a substantial amount of reference information that can be used to solve possible problems in the proposed research.

Depending on research progress, additional Mach numbers (intermediate as well as higher transonic)

3. *No equivalent comparison possible*
4. VSAERO vs. Euler-SU2
5. *No equivalent comparison possible*
6. *No equivalent comparison possible*
7. Euler-SU2 vs. Euler-SU2

Additionally, it is interesting to test the developed methodology on its ability to quantify the additional uncertainty introduced when replacing a panel method (e.g. VSAERO or XFLR5) by a vortex lattice method (e.g. XFLR5 or AVL) or a code using lifting line theory (XFLR5). Given the larger differences between geometry modelling abilities between the 3D-solvers (compared to 2D-codes) and the associated increases in computational cost, especially this factor is very relevant in conceptual design.

8.3. Planning

Figure 8.2 shows a preliminary timeline of the proposed graduation research project. It includes both the technological (Aerospace Engineering) perspective and the socio-psychological (Science Communication) perspective. In total, 57 ECs (equivalent to approximately 1600 hours or 200 days) is available for this project. 20 ECs (70 days) are shared between Aerospace Engineering and Science Communication; with 15 ECs (52 days) specifically dedicated to Science Communication and 22ECs (78 days) to Aerospace Engineering. Report writing is not included as separate task, but will be done throughout the project.

As can be seen in the figure, the work is planned to be completed in 163 days, of which $(33 + 25 + 15 + 5 =) 78$ are assigned to Aerospace Engineering (AE), $(20 + 15 =) 35$ to Science Communication (SC) and $(20 + 35 - 5 =) 50$ to the combination of the two. The fact that these numbers do not add up to the 'budgets' presented in the previous paragraph can be explained by earlier completion of an extensive literature study into decision quality and factors influencing that (15 days; SC) and substantial research into and reporting on items (such as research set-up, context and background) not covered in any of the other tasks (22 days, AE + SC).

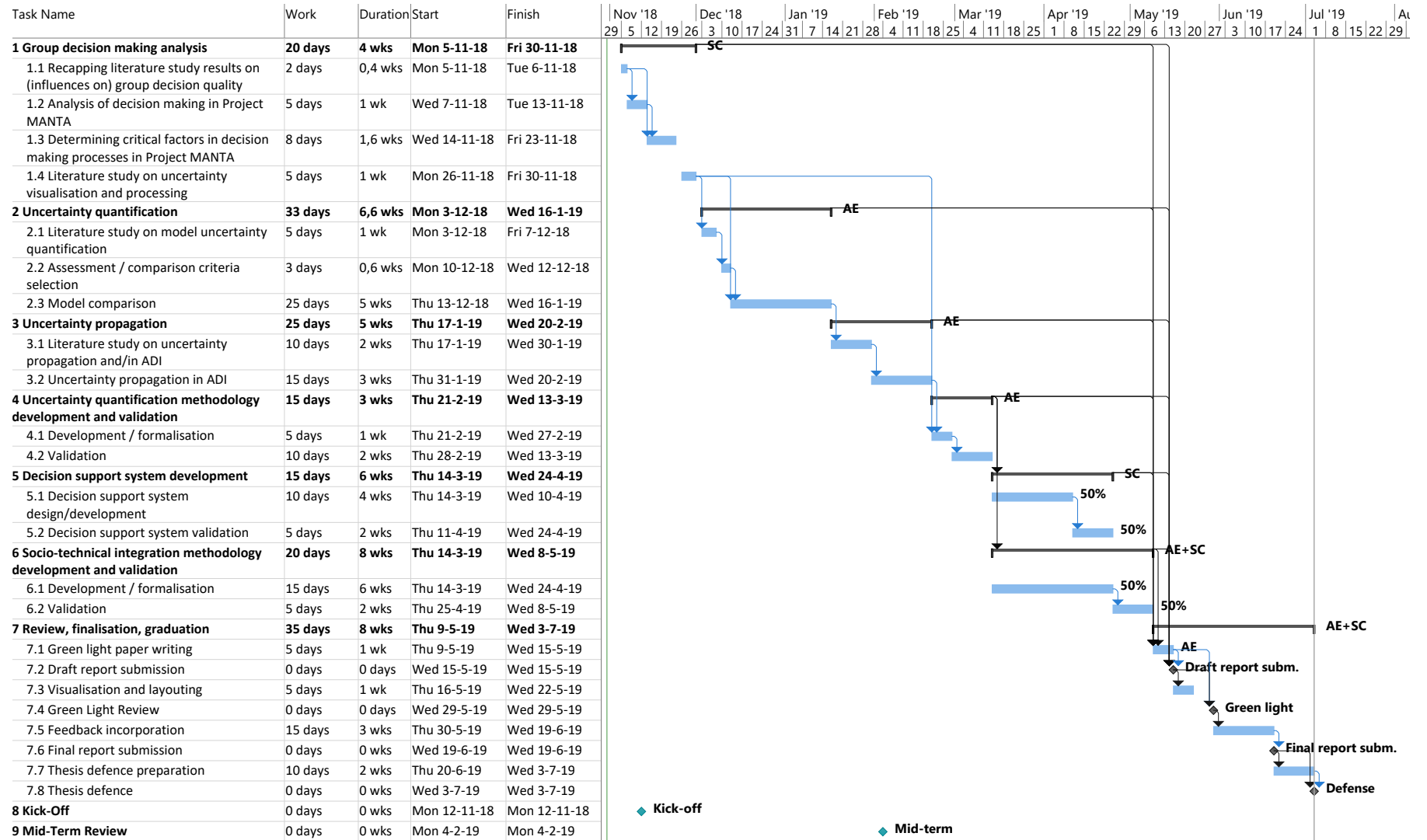


Figure 8.2: Graduation research project planning

Bibliography

- Ahn, J. and Lee, D. (2012). Airfoil Designs and Free-Flight Tests of a Fixed Wing MAV Design. In *30th AIAA Applied Aerodynamics Conference*, pages 1–8, New Orleans, United States of America. American Institute of Aeronautics and Astronautics.
- Ajaj, R. M., Friswell, M. I., Saavedra Flores, E. I., Little, O., and Isikveren, A. T. (2012). Span Morphing: A Conceptual Design Study. In *53rd AIAA/ASME/ASCE/AHS/ASC Structures, Structural Dynamics and Materials Conference*, pages 1–12, Honolulu, United States of America. American Institute of Aeronautics and Astronautics.
- Ajaj, R. M., Friswell, M. I., Saavedra Florse, E. I., Keane, A., Isikveren, A. T., Allegri, G., and Adhikari, S. (2014). Morphing aircraft: The need for a new design philosophy. *Journal of Intelligent Material Systems and Structures*, 25(8):989–1008.
- Analytical Methods. VSAERO - Nonlinear Aerodynamic Software.
- Analytical Methods (2018a). MSES/MISES. <https://www.ami.aero/software-computing/amis-computational-fluid-dynamics-tools/mseismises/>. Accessed June 29th, 2018.
- Analytical Methods (2018b). VSAERO. <https://www.ami.aero/software-computing/amis-computational-fluid-dynamics-tools/vsaero/>. Accessed June 29th, 2018.
- Anderson, J. D. (1995). *Computational Fluid Dynamics - The Basics with Applications*. McGraw-Hill.
- Anderson, J. D. (2001). *Fundamentals of Aerodynamics*. McGraw-Hill, New York, United States of America, 3rd edition.
- Anderson, J. D. (2002). *Modern Compressible Flow*. McGraw-Hill, New York, United States of America, 3rd edition.
- Anderson, J. D., Degroote, J., Degrez, G., Dick, E., Grundmann, R., and Vierendeels, J. (2009). *Computational Fluid Dynamics: An Introduction*. Springer-Verlag Berlin Heidelberg, 3rd edition.
- Argyropoulos, C. D. and Markatos, N. C. (2015). Recent advances on the numerical modelling of turbulent flows. *Applied Mathematical Modelling*, 39(2):693–732.
- Ashill, P. R. and Weeks, D. J. (1978). An experimental investigation of the drag of thick supercritical aerofoils – a progress report. Technical Report 1765, Royal Aircraft Establishment, United Kingdom.
- Atkin, C. J. and Gowree, E. R. (2012). Recent Developments to the viscous Garabedian and Korn method. In *28th International Congress of the Aeronautical Sciences*, pages 1–9, Brisbane, Australia.
- AVL LIST GmbH (2018). AVL - Development, testing & simulation of powertrain systems. <https://www.avl.com/>. Accessed August 17th, 2018.
- Bakker, A. (2006). Applied computational fluid dynamics (lecture 5 - solution methods). <http://www.bakker.org/dartmouth06/engs150/05-solv.pdf>. Downloaded June 5th, 2018.
- Baldwin, B. S. and Barth, T. J. (1991). A One-Equation Turbulence Transport Model for High Reynolds Number Wall-Bounded Flows. In *29th Aerospace Sciences Meeting*, pages 1–24, Reno, United States of America. American Institute of Aeronautics and Astronautics.

- Baldwin, B. S. and Lomax, H. (1978). Thin Layer Approximation and Algebraic Model for Separated Turbulent Flows. In *AIAA 16th Aerospace Sciences Meeting*, pages 1–8, Huntsville, United States of America. American Institute of Aeronautics and Astronautics.
- Bandyopadhyay, P. R. (1992). Reynolds Number Dependence of the Freestream Turbulence Effects on Turbulent Boundary Layers. *AIAA Journal*, 30(7):6–8.
- Barth, T. J., Pulliam, T. H., and Buning, P. G. (1985). Navier-Stokes Computations for Exotic Airfoils. In *23rd Aerospace Sciences Meeting*, pages 1–16, Reno, United States of America. American Institute of Aeronautics and Astronautics.
- Beam, R. M. and Warming, R. F. (1976). An Implicit Finite-Difference Algorithm for Hyperbolic Systems in Conservation-Law Form. *Journal of Computational Physics*, 22(1):87–110.
- Belie, R. G. (1993). Three Enabling Technologies for Integrated Product Development. In *31st Aerospace Science Meeting & Exhibit*, Reno, United States of America. American Institute of Aeronautics and Astronautics.
- Ben Mosbah, A., Botez, R. M., and Dao, T.-M. (2016). New methodology combining neural network and extended great deluge algorithms for the ATR-42 wing aerodynamics analysis. *Aeronautical Journal*, 120(1229):1049–1080.
- Bertin, J. J. and Cummings, R. M. (2009). *Aerodynamics for Engineers*. Pearson Prentice-Hall, New Jersey, United States of America, 5th edition.
- Blazek, J. (2007). *Computational Fluid Dynamics - Principles and Applications*. Butterworth-Heinemann / Elsevier, Oxford, United Kingdom, 3rd edition.
- Blockley, R. H. and Hodges, M. D. (1982). Methods for Estimating the Pressure Distribution on a Two-Dimensional Aerofoil in Viscous Transonic Flow. Technical Report ESDU 81019, Royal Aeronautical Society, United Kingdom.
- Bodling, A., Agrawal, B. R., Sharma, A., Clark, I., Alexander, W. N., and Devenport, W. J. (2017). Numerical Investigation of Bio-Inspired Blade Designs at High Reynolds Numbers for Ultra-Quiet Aircraft and Wind Turbines. In *23rd AIAA/CEAS Aeroacoustics Conference*, pages 1–18, Reston, United States of America. American Institute of Aeronautics and Astronautics.
- Boschetti, P. J., Cárdenas, E. M., Amerio, A., and Arévalo, Á. (2010). Stability and Performance of a Light Unmanned Airplane in Ground Effect. In *48th AIAA Aerospace Sciences Meeting Including the New Horizons Forum and Aerospace Exposition*, pages 1–17, Orlando, United States of America. American Institute of Aeronautics and Astronautics.
- Bousman, W. G. (2003). Aerodynamic Characteristics of SC1095 and SC1094 R8 Airfoils. Technical Report TP-2003-212265, National Aeronautics and Space Administration, Moffett Field, United States of America.
- Bradshaw, P. (1971). Calculation of three-dimensional turbulent boundary layers. *Journal of Fluid Mechanics*, 46(3):417–445.
- Bragg, M. B., Gregorek, G. M., and Lee, J. D. (1985). Airfoil Aerodynamics in Icing Conditions. *Journal of Aircraft*, 23(1):76–81.
- Cárdenas, E. M., Boschetti, P. J., and Amerio, A. (2009). Stability and Flying Qualities of an Unmanned Airplane using Vortex Lattice Method. *Journal of Aircraft*, 46(4):1–9.
- Carty, A. (2002). An Approach to Multidisciplinary Design, Analysis & Optimization For Rapid Conceptual Design. In *9th AIAA/ISSMO Symposium on Multidisciplinary Analysis and Optimization*, Atlanta, United States of America. American Institute of Aeronautics and Astronautics.

- Castegnaro, S. (2017). A Critical Analysis of the Differences Among Design Methods for Low-Speed Axial Fans. In *Proceedings of ASME Turbo Expo 2017: Turbomachinery Technical Conference and Exhibition*, pages 1–11, Charlotte, United States of America.
- Catherall, D., Foster, D. N., and Sells, C. C. L. (1969). Two-dimensional incompressible flow past a lifting aerofoil. Technical Report 69118, Royal Aircraft Establishment, United Kingdom.
- Cavallo, B. (1966). Subsonic drag estimation methods. Technical Report NADC-AW-6604, US Naval Air Development Center. Based on Ajaj et al. (2014). In other sources, the author's name is spelled B. Cavallok.
- Cebeci, T. and Smith, A. M. O. (1974). *Analysis of Turbulent Boundary Layers*. Academic Press, New York, United States of America.
- CFD Online (2013). Large eddy simulation (LES). <https://www.cfd-online.com/Wiki/Les>. Accessed August 14th, 2018.
- Chaparro, D., Fujiwara, G. E. C., Ting, E., and Nguyen, N. (2017). Transonic and Viscous Potential Flow Method Applied to Flexible Wing Transport Aircraft. In *35th AIAA Applied Aerodynamics Conference*, pages 1–16, Denver, United States of America. American Institute of Aeronautics and Astronautics.
- Chaussee, D. S. and Pulliam, T. H. (1980). A Diagonal Form of an Implicit Approximate-Factorization Algorithm with Application to a Two Dimensional Inlet. In *AIAA 18th Aerospace Sciences Meeting*, pages 1–8, Pasadena, United States of America. American Institute of Aeronautics and Astronautics.
- Chin, V. D., Peters, D. W., Spaid, F. W., and McGhee, R. J. (1993). Flowfield Measurements about a Multi-Element Airfoil at High Reynolds Numbers. In *AIAA 24th Fluid Dynamics Conference*, pages 1–15, Orlando, United States of America. American Institute of Aeronautics and Astronautics.
- Chorin, A. J. (1997). A numerical method for solving incompressible viscous flow problems. *Journal of Computational Physics*, 135(2):118–125.
- Chow, R. R. (1985). Solution of Viscous Transonic Flow over Wings. *Computers & Fluids*, 13(3):285–317.
- Ciampa, P.-D., Nagel, B., and La Rocca, G. (2013). Preliminary Design for Flexible Aircraft in a Collaborative Environment. In *The International Conference of the European Aerospace Societies (CEAS)*, pages 270–281.
- Cochrane Library (2018). About cochrane reviews. <https://www.cochrane.org/news/cochrane-priority-reviews-list-update>. Accessed October 30th, 2018.
- Coder, J. G. and Maughmer, M. D. (2014). Comparisons of Theoretical Methods for Predicting Airfoil Aerodynamic Characteristics. *Journal of Aircraft*, 51(1):183–191.
- Coder, J. G., Maughmer, M. D., and Somers, D. M. (2014). Theoretical and Experimental Results for the S414, Slotted, Natural-Laminar-Flow Airfoil. *Journal of Aircraft*, 51(6):1883–1890.
- Coiro, D. P., Nicolosi, F., and Grasso, F. (2009). Design and Testing of Multi-Element Airfoil for Short-Takeoff-and-Landing Ultralight Aircraft. *Journal of Aircraft*, 46(5):1795–1807.
- Coles, D. (1956). The law of the wake in the turbulent boundary layer. *Journal of Fluid Mechanics*, 1(2):191–226.
- Coles, D. E. (1953). *Measurements in the boundary layer on a smooth flat plate in supersonic flow*. Doctoral dissertation, California Institute of Technology.
- Collyer, M. and Lock, R. (1978). Improvements to the viscous carabedian and korn method for calculating transonic flow past an airfoil. *RAE Technical Report*, 78039.

- Cosyn, P. and Vierendeels, J. (2006). Numerical Investigation of Low-Aspect-Ratio Wings at Low Reynolds Numbers. *Journal of Aircraft*, 43(3).
- Counsil, J. N. N. and Goni Boulama, K. (2008). Validating the URANS shear stress transport $\gamma - Re_{\theta}$ model for low-Reynolds-number external aerodynamics. *International Journal for Numerical Methods in Fluids*, 69:1411–1432.
- Cousteix, J. (1987). Three-dimensional boundary layers: Introduction to calculation methods. In *In AGARD Computation of Three-Dimensional Boundary Layers Including Separation 49 p (SEE N87-22145 15-34)*.
- Cousteix, J. and Houdeville, R. (1981). Singularities in Three-Dimensional Turbulent Boundary-Layer Calculations and Separation Phenomena. *AIAA Journal*, 19(8):976–985.
- Coutu, D., Brailovski, V., and Terriault, P. (2010). Optimized design of an active extradors structure for an experimental morphing laminar wing. *Aerospace Science and Technology*, 14(7):451–458.
- Cross, A. G. T. (1979). Calculation of compressible three-dimensional turbulent boundary layers with particular reference to wings and bodies. *British Aerospace Brough YAD*, 3379.
- Cummings, R. M., Mason, W. H., Morton, S. A., and McDaniel, D. R. (2015). *Applied Computational Aerodynamics*. Cambridge University Press, New York, United States of America, 1 edition.
- Cumpsty, N. A. and Head, M. R. (1967). The Calculation of Three-Dimensional Turbulent Boundary Layers: Part I: Flow over the Rear of an Infinite Swept Wing. *Aeronautical Quarterly*, 18(1):55–84.
- Cumpsty, N. A. and Head, M. R. (1969). The Calculation of the Three-Dimensional Turbulent Boundary Layer - Part III. Comparison of Attachment-Line Calculations with Experiment. *Aeronautical Quarterly*, 20(2):99–113.
- Curle, N. (1967). A Two-Parameter Method for Calculating the Two-Dimensional Incompressible Laminar Boundary Layer. *Journal of the Royal Aeronautical Society*, 71(674):117–123.
- Da Ronch, A., Badcock, K. J., McFarlane, C., Beaverstock, C., Ooppelstrup, J., Zhang, M., and Rizzi, A. (2010). Benchmarking CEASIOM software to predict flight control and flying qualities of the B-747. In *27th International Congress of the Aeronautical Sciences*, pages 1–21, Nice, France.
- Da Ronch, A., Ghoreyshi, M., Vallespin, D., Badcock, K. J., Mengmeng, Z., Ooppelstrup, J., and Rizzi, A. (2011). A Framework for Constrained Control Allocation Using CFD-based Tabular Data. In *49th AIAA Aerospace Sciences Meeting including the New Horizons Forum and Aerospace Exposition*, pages 1–18, Orlando, United States of America. American Institute of Aeronautics and Astronautics.
- Dantsker, O. D. and Vahora, M. (2018). Comparison of aerodynamic characterization methods for design of unmanned aerial vehicles. In *2018 AIAA Aerospace Sciences Meeting*, pages 1–19, Kissimmee, United States of America. American Institute of Aeronautics and Astronautics.
- de Bruin, A. and de Boer, E. (1982). Users guide of BOLA-2D, the NLR-method for the calculation of (quasi) two-dimensional boundary layers. Technical Report AE-82-014 U, Netherlands Aerospace Laboratory, The Netherlands.
- de Oliveira, L. F. Q., Cerón-Muñoz, H. D., and Catalano, F. M. (2012). Aerodynamic Analysis Of High Rotation And Low Reynolds Number Propeller. In *48th AIAA/ASME/SAE/ASEE Joint Propulsion Conference & Exhibit*, pages 1–12, Atlanta, United States of America. American Institute of Aeronautics and Astronautics.
- Deepa, A., Ganesh, R. V., Condoor, S., and Sial, S. (2016). Wing Design for a Low Altitude Unmanned Aerial Vehicle: A Nuanced Study of Aerodynamic Drag. In *Aerospace Conference, 2016 IEEE*, pages 1–10.

- Deperrois, A. (2003). XFLR5. <http://www.xflr5.com/ReleaseNotes.htm>. Accessed June 25th, 2018.
- Deperrois, A. (2009). About XFLR5 calculations and experimental measurements.
- Deperrois, A. (2011a). Modal analysis and experimental validation.
- Deperrois, A. (2011b). xflr5 - Analysis of foils and wings operating at low Reynolds numbers - Guidelines for XFLR5 v6.03. Technical report.
- Deperrois, A. (2018). XFLR5. <http://www.xflr5.com/xflr5.htm>. version 6.42.
- Dini, P., Selig, M. S., and Maughmer, M. D. (1992). Simplified Linear Stability Transition Prediction Method for Separated Boundary Layers. *AIAA Journal*, 30(8):1953–1961.
- Drela, M. (1985). *Two-dimensional transonic aerodynamic design and analysis using the Euler equations*. Doctoral dissertation, Massachusetts Institute of Technology.
- Drela, M. (1989). XFOIL: An Analysis and Design System for Low Reynolds Number Airfoils. In Mueller, T. J., editor, *Low Reynolds Number Aerodynamics*, pages 1–12. Springer-Verlag.
- Drela, M. (1990). Newton Solution of Coupled Viscous/Inviscid Multielement Airfoil Flows. In *AIAA 21st Fluid Dynamics, Plasma Dynamics and Lasers Conference*, Seattle, United States of America. American Institute of Aeronautics and Astronautics.
- Drela, M. (1994). MSES Multi-element Airfoil Design / Analysis Software - Summary.
- Drela, M. (2003). Implicit Implementation of the Full e^n Transition Criterion. In *21st Applied Aerodynamics Conference*, Orlando, United States of America. American Institute of Aeronautics and Astronautics.
- Drela, M. (2007). A User's Guide to MSES 3.05. Technical report, Massachusetts Institute of Technology, Massachusetts, United States of America.
- Drela, M. (2013). Summary of changes made for recent mses versions. http://web.mit.edu/drela/Public/web/mses/version_notes.txt. Accessed August 1st, 2018.
- Drela, M. and Giles, M. B. (1987a). ISES - A two-dimensional viscous aerodynamic design and analysis code. In *25th AIAA Aerospace Sciences Meeting*, Reno, United States of America. American Institute of Aeronautics and Astronautics.
- Drela, M. and Giles, M. B. (1987b). Viscous-Inviscid Analysis of Transonic and Low Reynolds Number Airfoils. *AIAA Journal*, 25(10):1347–1355.
- Drela, M. and Youngren, H. (2001). XFOIL 6.9 User Primer. Technical report.
- Drela, M. and Youngren, H. (2010). AVL 3.30 User Primer. Technical report, Massachusetts Institute of Technology, Massachusetts, United States of America.
- Drela, M. and Youngren, H. (2013a). XFOIL - Subsonic Airfoil Development System. <http://web.mit.edu/drela/Public/web/xfoil/>. version 6.99.
- Drela, M. and Youngren, H. (2013b). XFOIL version notes. http://web.mit.edu/drela/Public/web/xfoil/version_notes.txt.
- Drela, M. and Youngren, H. (2017). AVL. <http://web.mit.edu/drela/Public/web/avl/>. version 3.37.
- Driver, J. and Zingg, D. W. (2007). Numerical Aerodynamic Optimization Incorporating Laminar-Turbulent Transition Prediction. *AIAA Journal*, 45(8):1810–1818.
- Dvorak, F. A., Maskew, B., and Woodward, F. A. (1977a). Investigation of Three-Dimensional Flow Separation on Fuselage Configurations. Technical report, U. S. Army Air Mobility Research and De-

- velopment Laboratory, Fort Eustis, United States of America.
- Dvorak, F. A. and Woodward, F. A. (1974). A Viscous/Potential Flow Interaction Analysis Method for Multi-Element Infinite Swept Wings: Volume I. Technical report, National Aeronautics and Space Administration, Kent, United States of America.
- Dvorak, F. A., Woodward, F. A., and Maskew, B. (1977b). A Three-Dimensional Viscous/Potential Flow Interaction Analysis Method for Multi-Element Wings. Technical report, National Aeronautics and Space Administration.
- Economou, T. D., Mudigere, D., Bansal, G., Heinecke, A., Palacios, F., Park, J., Smelyanskiy, M., Alonso, J. J., and Dubey, P. (2016a). Performance optimizations for scalable implicit RANS calculations with SU2. *Computers and Fluids*, 129:146–158.
- Economou, T. D., Palacios, F., Copeland, S. R., Lukaczyk, T. W., and Alonso, J. J. (2016b). SU2: An Open-Source Suite for Multiphysics Simulation and Design. *AIAA Journal*, 54(3):828–846.
- Elham, A. (2013). *Weight Indexing for Multidisciplinary Design Optimization of Lifting Surfaces*. Doctoral dissertation, Delft University of Technology.
- Elham, A. (2015). Adjoint quasi-three-dimensional aerodynamic solver for multi-fidelity wing aerodynamic shape optimization. *Aerospace Science and Technology*, 41(2015):241–249.
- Elham, A. and van Tooren, M. J. (2016). Coupled adjoint aerostructural wing optimization using quasi-three-dimensional aerodynamic analysis. *Structural and Multidisciplinary Optimization*, 54(4):889–906.
- Elham, A. and van Tooren, M. J. L. (2014). Winglet multi-objective shape optimization. *Aerospace Science and Technology*, 37(5):93–109.
- Elham, A., van Tooren, M. J. L., and Sobieszcanski-Sobieski, J. (2014). Bilevel Optimization Strategy for Aircraft Wing Design Using Parallel Computing. *AIAA Journal*, 52(8):1770–1783.
- Eppler, R. (1997). Induced drag and winglets. *Aerospace Science and Technology*, 1(1):3–15.
- Fernandes, G., Make, M., Gueydon, S., and Vaz, G. (2014). Sensitivity to Aerodynamic Forces for the Accurate Modelling of Floating Offshore Wind Turbines. In *1st International Conference on Renewable Energies Offshore*, pages 24–26.
- Ferrer, E. and Munduate, X. (2009). CFD Predictions of Transition and Distributed Roughness Over a Wind Turbine Airfoil. In *47th AIAA Aerospace Sciences Meeting including The New Horizons Forum and Aerospace Exposition*, pages 1–16. American Institute of Aeronautics and Astronautics.
- Ferziger, J. H. and Perić, M. (2002). *Computational Methods for Fluid Dynamics*. Springer-Verlag Berlin Heidelberg, New York, United States of America, 3rd edition.
- Filippone, A. and Selig, M. (1998). Low-aspect-ratio wings for wing-ships. In *36th AIAA Aerospace Sciences Meeting and Exhibit*, pages 1–12. American Institute of Aeronautics and Astronautics.
- Florjancic, D. (2015). *Improved Design of a High Lift System for General Aviation Aircraft*. Master's thesis, Delft University of Technology.
- Freestone, M. M. (1998). Transonic data memorandum - VGK Method for two-dimensional aerofoil sections - Part 4: Estimation of excrescence drag at subsonic speeds. Technical Report ESDU 98031, Royal Aeronautical Society, United Kingdom.
- Freestone, M. M. (1999). Transonic data memorandum structures - VGK method for two-dimensional aerofoil sections - Part 5: Design to a specified upper-surface pressure distribution. Technical Report ESDU 99032, Royal Aeronautical Society, United Kingdom.

- Freestone, M. M. (2001). Transonic data memorandum - VGK method for two-dimensional aerofoil sections - Part 6: Aerofoil with simple hinged flaps. Technical Report ESDU 01033, Royal Aeronautical Society, United Kingdom.
- Freestone, M. M. (2004). VGK method for two-dimensional aerofoil sections - Part 1: principles and results. Technical Report ESDU 96028, Royal Aeronautical Society, United Kingdom.
- Freestone, M. M. (2010). Transonic data memorandum - VGK method for two-dimensional aerofoil sections - Part 2: User manual. Technical Report ESDU 96029, Royal Aeronautical Society, United Kingdom.
- Freestone, M. M. (2011). VGK method for two-dimensional aerofoil sections - Part 3: estimation of a separation boundary in transonic flow. Technical Report ESDU 97030, Royal Aeronautical Society, United Kingdom.
- Fuglsang, P., Bak, C., Gaunaa, M., and Antoniou, I. (2016). Design and Verification of the Risø-B1 Airfoil Family for Wind Turbines. *Journal of Solar Energy Engineering*, 126(4):1002–1010.
- Fujiwara, G. E. C., Chaparro, D., and Nguyen, N. (2016). An Integral Boundary Layer Direct Method Applied to 2D Transonic Small-Disturbance Equations. In *34th AIAA Applied Aerodynamics Conference*, Washington, United States of America. American Institute of Aeronautics and Astronautics.
- Garabedian, P. and McFadden, G. (1982). Design of Supercritical Swept Wings. *AIAA Journal*, 20(3):289–291.
- Garabedian, P. R. (1976). Computation of wave drag for transonic flow. *Journal d'Analyse Mathématique*, 30(1):164–171.
- Garabedian, P. R. and Korn, D. G. (1971). Analysis of Transonic Airfoils. *Communications on Pure and Applied Mathematics*, 24(6):841–851.
- Gary, A. M. and McDonald, R. A. (2014). Aerodynamic Shape Optimization of Propulsion Airframe Integration While Matching Lift Distribution. In *52nd Aerospace Sciences Meeting*, pages 1–13, National Harbor, United States of America. American Institute of Aeronautics and Astronautics.
- Gaster, M. (1967). The Structure and Behaviour of Laminar Separation Bubbles. Technical Report 3595, Aeronautical Research Council, London, United Kingdom.
- Genco, N. and Altman, A. (2009). Parametric Study of the Performance of a Biplane Joined at the Tips. In *47th AIAA Aerospace Sciences Meeting including The New Horizons Forum and Aerospace Exposition*, pages 1–11, Orlando, United States of America. American Institute of Aeronautics and Astronautics.
- Gerritsma, M. I. (2002). *Computational Fluid Dynamics, Incompressible Flow*. Delft University Press, Delft, The Netherlands.
- Ghaffari, F. (1988). An Analytical Method for the Ditching Analysis of an Airborne Vehicle. *Journal of Aircraft*, 27(4):312–319.
- Ghosh, S., Rancourt, D., Daskilewicz, M. J., Lee, C., and Mavis, D. N. (2014). A Visualization Method for Multidisciplinary System under Uncertainty. In *14th AIAA Aviation Technology, Integration, and Operations Conference*, pages 1–13, Reston, Virginia. American Institute of Aeronautics and Astronautics.
- Giesing, J. P. and Barthelemy, J.-F. M. (1998). A summary of industry MDO applications and needs. In *7th AIAA/USAF/NASA/ISSMO Symposium on Multidisciplinary Analysis and Optimization*, pages 1–20. American Institute of Aeronautics and Astronautics.
- Giles, M. B. and Drela, M. (1987). Two-Dimensional Transonic Aerodynamic Design Method. *AIAA*

Journal, 25(9):1199–1206.

- González R., P. J., Boschetti, P. J., Cárdenas, E. M., and Amerio, A. (2010). Evaluation of the Flying Qualities of a Half-Scale Unmanned Airplane via Flight Simulation. In *48th AIAA Aerospace Sciences Meeting Including the New Horizons Forum and Aerospace Exposition*, pages 1–7, Orlando, United States of America. American Institute of Aeronautics and Astronautics.
- Granville, P. S. (1953). The Calculation of the Viscous Drag of Bodies of Revolution. Technical report, U. S. Navy.
- Green, J. E., Weeks, D. J., and Brooman, J. (1977). Prediction of Turbulent Boundary Layers and Wakes in Compressible Flow by a Lag-Entrainment Method. Technical Report 3791, Aeronautical Research Council, London, United Kingdom.
- Green, J. E., Weeks, D. J., and Brooman, J. W. F. (1973). Prediction of turbulent boundary-layers and wakes in compressible flow by a lag-entrainment method. Technical Report 3791, Aeronautical Research Council.
- Greer, D., Hamory, P., Krake, K., and Drela, M. (2000). Design and Predictions for High-Altitude (Low Reynolds Number) Aerodynamic Flight Experiment. *Journal of Aircraft*, 37(4):684–689.
- Gu, X., Ciampa, P. D., and Nagel, B. (2018). An automated CFD analysis workflow in overall aircraft design applications. *CEAS Aeronautical Journal*, 9(1):3–13.
- Guo, Z., Chen, X.-k., Hou, Z.-x., and Guo, J. (2011). Development of a Solar Electric Powered UAV for Long Endurance Flight. In *11th AIAA Aviation Technology, Integration, and Operations (ATIO) Conference*, pages 1–13, Virginia Beach, United States of America. American Institute of Aeronautics and Astronautics.
- Guzel, G., Sankar, L. N., and Rhee, M. (2005). Computational Investigation of the Effects of Gurney Flap on the Aerodynamic Performance of VR-12 Airfoil. In *23rd AIAA Applied Aerodynamics Conference*, pages 1–22, Toronto, Canada. American Institute of Aeronautics and Astronautics.
- Haimes, R. and Drela, M. (2012). On The Construction of Aircraft Conceptual Geometry for High-Fidelity Analysis and Design. In *50th AIAA Aerospace Sciences Meeting including the New Horizons Forum and Aerospace Exposition*, pages 1–21. American Institute of Aeronautics and Astronautics.
- Harris, C. D. (1981). Two-Dimensional Aerodynamic Characteristics of the NACA 0012 Airfoil in the Langley 8-Foot Transonic Pressure Tunnel. Technical Report NASA-TM-81927, National Aeronautics and Space Administration, Hampton, United States of America.
- Hassan, A. A. and Munts, E. A. (2000). Transverse and Near-Tangent Synthetic Jets for Aerodynamic Flow Control. In *18th Applied Aerodynamics Conference*, pages 1–17, Denver, United States of America. American Institute of Aeronautics and Astronautics.
- Hassanalain, M. and Abdelkefi, A. (2017). Design, manufacturing, and flight testing of a fixed wing micro air vehicle with Zimmerman planform. *Meccanica*, 52(6):1265–1282.
- Head, M. R. (1958). Entrainment in the Turbulent Boundary Layer. Technical Report 3152, Aeronautical Research Council, London, United Kingdom.
- Henne, P. A., editor (1990). *Applied Computational Aerodynamics*, volume 125 of *Progress in Astronautics and Aeronautics*. American Institute of Aeronautics and Astronautics.
- Hess, J. L. (1988). Development and Application of Panel Methods. In Cruse, T. A., editor, *Advanced Boundary Element Methods - IUTAM Symposium San Antonio, Texas, 1987*, pages 165–177. Springer-Verlag Berlin Heidelberg.
- Hirsch, C. (2007). *Fundamentals of Computational Fluid Dynamics*, volume 1 of *Numerical Computa-*

- tions of Internal and External Flows*. Butterworth-Heinemann / Elsevier, Oxford, United Kingdom, 2nd edition.
- Hoak, D. E. (1978). USAF Stability and Control DATCOM. Technical report, Air Force Flight Dynamics Laboratory, Ohio, United States of America.
- Holst, T. L. (1988). Viscous Transonic Airfoil Workshop Compendium of Results. *Journal of Aircraft*, 25(12):1073–1087.
- Holst, T. L. (2000). Transonic flow computations using nonlinear potential methods. *Progress in Aerospace Sciences*, 36(1):1–61.
- Houwink, R. and Veldman, A. E. P. (1984). Steady and Unsteady Separated Flow Computations for Transonic Airfoils. In *AIAA 17th Fluid Dynamics, Plasma Dynamics, and Lasers Conference*, pages 1–11, Snowmass, United States of America. American Institute of Aeronautics and Astronautics.
- Iaccarino, G., Ooi, A., Durbin, P. A., and Behnia, M. (2003). Reynolds averaged simulation of unsteady separated flow. *International Journal of Heat and Fluid Flow*, 24:147–156.
- IHS. ESDU Aerospace Package. https://www.esdu.com/cgi-bin/ps.pl?sess=delft_1181011123020mvw&t=col&p=pk_aesp. Accessed October 11th, 2018.
- Innes, F., Hammar, J. N., and Philpott, D. R. (2004). Transonic data memorandum - VGK method for two-dimensional aerofoil sections - Part 7: VGK for Windows. Technical Report ESDU 03015, Royal Aeronautical Society, United Kingdom.
- Jagdale, V., Patil, A., Stanford, B., and Ifju, P. (2009). Conceptual Design of a Bendable UAV Wing Considering Aerodynamic and Structural Performance. In *50th AIAA Structures, Structural Dynamics, and Materials Conference*, pages 1–10, Palm Springs, United States of America. American Institute of Aeronautics and Astronautics.
- Jameson, A. (1999). Re-Engineering the Design Process Through Computation. *Journal of Aircraft*, 36(1):36–50.
- Jameson, A. (2003). CFD for Aerodynamic Design and Optimization: Its Evolution over the Last Three Decades. In *16th AIAA CFD Conference*, pages 1–11, Orlando, United States of America. American Institute of Aeronautics and Astronautics.
- Jameson, A. (2004). Aerodynamics. In Stein, E., de Borst, R., and Hughes, T. J. R., editors, *Encyclopedia of Computational Mechanics*, chapter 11. John Wiley & Sons, Ltd.
- Jameson, A., Schmidt, W., and Turkel, E. (1981). Numerical Solutions of the Euler Equations by Finite Volume Methods Using Runge-Kutta Time-Stepping Schemes. In *14th Fluid and Plasma Dynamics Conference*. American Institute of Aeronautics and Astronautics.
- Johnson, F. T. and Rubbert, P. E. (1975). Advanced panel-type influence coefficient methods applied to subsonic flows. In *AIAA 13th Aerospace Sciences Meeting*, Pasadena, United States of America. American Institute of Aeronautics and Astronautics.
- Jungo, A., Zhang, M., Vos, J. B., and Rizzi, A. (2018). Benchmarking New CEASIOM with CPACS adoption for aerodynamic analysis and flight simulation. *Aircraft Engineering and Aerospace Technology*, 90(4):613–626.
- Katz, J. and Plotkin, A. (1991). *Low-Speed Aerodynamics - From Wing Theory to Panel Methods*. McGraw-Hill, Inc., Singapore.
- Kaul, U. K. and Nguyen, N. T. (2014). Drag Optimization Study of Variable Camber Continuous Trailing Edge Flap (VCCTEF) Using OVERFLOW. In *32nd AIAA Applied Aerodynamics Conference*, pages 1–20, Atlanta, United States of America. American Institute of Aeronautics and Astronautics.

- Keep, J. A., Vitale, S., Pini, M., and Burigana, M. (2017). Preliminary verification of the open-source CFD solver SU2 for radial-inflow turbine applications. *Energy Procedia*, 129:1071–1077.
- Khalid, M., Sun, Y., and Vyriotes, P. (1997). An evaluation of Navier-Stokes and potential methods for helicopter interactional aerodynamics. In *35th AIAA Aerospace Sciences Meeting & Exhibit*, Reno, United States of America. American Institute of Aeronautics and Astronautics.
- Kirk, W. T., Capece, V. R., Pechlivanoglou, G., Nayeri, C. N., and Paschereit, C. O. (2014). Comparative Study of CFD Solver Models for Modeling of Flow over Wind Turbine Airfoils. In *Proceedings of ASME Turbo Expo 2014: Turbine Technical Conference and Exhibition*, pages 1–9, Düsseldorf, Germany.
- Kiyici, F. and Aradag, S. (2015). Design and Optimization of a Supersonic Business Jet. In *22nd Applied Aerodynamics Conference*, pages 1–14, Dallas, United States of America. American Institute of Aeronautics and Astronautics.
- Klausmeyer, S. M. and Lin, J. C. (1997). Comparative Results From a CFD Challenge Over a 2D Three-Element High-Lift Airfoil. Technical Report TR 112858, National Aeronautics and Space Administration, Hampton, United States of America.
- Koning, J. H. (2010). *Development of a KBE application to support aerodynamic design and analysis*. Master's thesis, Delft University of Technology.
- Kroo, I. (2004). Innovations in Aeronautics. In *42nd AIAA Aerospace Sciences Meeting*, pages 1–11, Reno, United States of America. American Institute of Aeronautics and Astronautics.
- Kurukularachchi, P. L., Munasinghe, S. R., and De Silva, H. R. P. S. (2016). Stability analysis for a twin boom H- tail Medium Scale UAV through simulated dynamic model. In *Moratuwa Engineering Research Conference (MERCon) MERCon 2016*, pages 415–420.
- Kusch, L., Albring, T., Walther, A., and Gauger, N. R. (2018). A one-shot optimization framework with additional equality constraints applied to multi- objective aerodynamic shape optimization. *Optimization Methods & Software*, pages 1–14.
- Kuzmin, D. Introduction to computational fluid dynamics. <http://www.mathematik.uni-dortmund.de/%7Ekuzmin/cfdintro/lecture3.pdf>. Downloaded June 5th, 2018.
- Lall, V., Papadakis, M., and Hoffmann, K. (1995). Evaluation of Turbulence Models for Attached and Separated Airfoil Flows. In *33rd Aerospace Sciences Meeting and Exhibit*, pages 1–21, Reno, United States of America. American Institute of Aeronautics and Astronautics.
- Lamar, J. E. (1976). A Vortex-Lattice for of the Mean Method Shapes of Trimmed Noncoplanar Planforms with Minimum Vortex With. Technical Report NASA TN D-8090, National Aeronautics and Space Administration, Hampton, United States of America.
- Langtry, R. B. and Menter, F. R. (2009). Correlation-Based Transition Modeling for Unstructured Parallelized Computational Fluid Dynamics Codes. *AIAA Journal*, 47(12):2894–2906.
- Lasauskas, E. (2005). Influence of transition location on airfoil drag. *Aviation*, 9(3):19–22.
- Lasauskas, E. and Naujokaitis, L. (2009). Analysis of three wing sections. *Aviation*, 13(1):3–10.
- Launder, B. E. and Spalding, D. B. (1974). The Numerical Computation of Turbulent Flows. *Computer Methods in Applied Mechanics and Engineering*, 3:269–289.
- le Balleur, J. (1981). Strong matching method for computing transonic viscous flows including wakes and separations - lifting airfoils. *Recherche Aérospatiale (English Edition)*, 3:21–45.
- Lednicer, D. A. and Gilchrist, I. J. (1991). A retrospective: Computational aerodynamic analysis methods applied to the P-51 Mustang. In *9th Applied Aerodynamics Conference*, pages 688–700. American

- Institute of Aeronautics and Astronautics.
- Lee, D., Van Nguyen, N., Tyan, M., Chun, H. G., Kim, S., and Lee, J.-W. (2017). Enhanced multi-fidelity model for flight simulation using global exploration and the Kriging method. *Proceedings of the Institution of Mechanical Engineers, Part G: Journal of Aerospace Engineering*, 231(4):606–620.
- Lee, M. W. and Visser, K. D. (2016). Towards an Effective Nonplanar Wing Design Strategy. In *34th AIAA Applied Aerodynamics Conference*, pages 1–15, Washington, United States of America. American Institute of Aeronautics and Astronautics.
- Leifsson, L., Koziel, S., Tesfahunegn, Y. A., Hosder, S., and Gramanzini, J.-R. (2014). Aerodynamic Design Optimization: Physics-based Surrogate Approaches for Airfoil and Wing Design. In *52nd Aerospace Sciences Meeting*, pages 1–13, National Harbor, United States of America. American Institute of Aeronautics and Astronautics.
- Léonard, T., Gicquel, L. Y. M., Gourdain, N., and Duchaine, F. (2015). Steady / Unsteady Reynolds-Averaged Navier-Stokes and Large Eddy Simulations of a Turbine Blade at High Subsonic Outlet Mach Number. *Journal of Turbomachinery*, 137:041001–1.
- Leschziner, M. A. (2010). Reynolds-Averaged Navier-Stokes Methods. In *Encyclopedia of Aerospace Engineering*, pages 1–14. John Wiley & Sons, Ltd.
- Letcher Jr., J. S. (1989). Convergence of Lift and Drag Predictions by a Morino Panel Method (VSAERO). *AIAA Journal*, 27(8):1019–1020.
- Lock, R. C. (1995). A method of determining the wave drag and its spanwise distribution on a finite wing in transonic flow. Technical Report ESDU 87003, Royal Aeronautical Society, United Kingdom.
- Lock, R. C. and Williams, B. R. (1987). Viscous-Inviscid Interactions in External Aerodynamics. *Progress in Aerospace Sciences*, 24(2):51–171.
- Lord, W. K. and Zysman, S. H. (1986). VSAERO Analysis of a Wing / Pylon / Nacelle Configuration. In *AIAA/IASME/ISAE/IASEE 22nd Joint Propulsion Conference*, pages 1–8, Huntsville, United States of America. American Institute of Aeronautics and Astronautics.
- Lykins, R., Keshmiri, S., Riley, R., and Garcia, G. (2011). Modal Analysis of 1/3-Scale Yak-54 Aircraft Through Simulation and Flight Testing. In *AIAA Atmospheric Flight Mechanics Conference*, pages 1–7, Portland, United States of America. American Institute of Aeronautics and Astronautics.
- Madsen, H. A. and Filippone, A. (1995). *Implementation and Test of the XFOIL Code for Airfoil Analysis and Design*. Risø National Laboratory, Roskilde, Denmark.
- Maksymiuk, C. M. and Pulliam, T. H. (1987). Viscous Transonic Airfoil Workshop Results Using ARC2D. In *AIAA 25th Aerospace Sciences Meeting*, pages 1–54, Reno, United States of America. American Institute of Aeronautics and Astronautics.
- Manzi, P. (1998). Investigation of Modeling and Simulation Tools Used in Aerospace Design Education. Technical report, Royal Institute of Technology (KTH).
- Margason, R. J., Kjelgaard, S. O., Sellers, W. L., Morris, C. E. K., Walkley, K. B., and Shields, E. W. (1985). Subsonic Panel Methods - A Comparison of Several Production Codes. In *23rd Aerospace Sciences Meeting*, pages 1–12. American Institute of Aeronautics and Astronautics.
- Mariens, J. (2012). *Wing Shape Multidisciplinary Design Optimization*. Master's thesis, Delft University of Technology.
- Mariens, J., Elham, A., and van Tooren, M. J. L. (2014). Quasi-Three-Dimensional Aerodynamic Solver for Multidisciplinary Design Optimization of Lifting Surfaces. *Journal of Aircraft*, 51(2):547–558.

- Martin, J. D. and Simpson, T. W. (2006). A Methodology to Manage System-level Uncertainty During Conceptual Design. *Journal of Mechanical Design*, 128(4):959–968.
- Martindale, T., Law, C., and Pedro, J. (2010). A Vortex Lattice Aerodynamic Model for Active Camber Controlled Wings. In *Seventh South African Conference on Computational and Applied Mechanics*, pages 1–10, Pretoria, South-Africa.
- Maskew, B. (1982a). Prediction of Subsonic Aerodynamic Characteristics: A Case for Low-Order Panel Methods. *Journal of Aircraft*, 19(2):157–166.
- Maskew, B. (1982b). Program VSAERO: A Computer Program for Calculating the Non-linear Aerodynamic Characteristics of Arbitrary Configurations – User’s Manual. Technical report, National Aeronautics and Space Administration, Moffett Field, United States of America.
- Maskew, B. (1987). Program VSAERO Theory Document. Technical report, National Aeronautics and Space Administration, Moffett Field, United States of America.
- Maskew, B. and Katz, J. (1987). Unsteady Low-Speed Aerodynamic Model for Complete Aircraft Configurations. *Journal of Aircraft*, 25(4):302–310.
- Mason, W. H. (1995). Incompressible Potential Flow Using Panel Methods. In *Applied Computational Aerodynamics Text*, chapter 4. Virginia Polytechnic Institute and State University.
- Maughmer, M. D. and Coder, J. G. (2010). Comparisons of Theoretical Methods for Predicting Airfoil Aerodynamic Characteristics. Technical Report TR 10-D-106, U.S. Army Research, Development and Engineering Command, Fort Eustis, United States of America.
- Maughmer, M. D. and Somers, D. M. (2007). Low-speed experimental results for two heavy-lift tiltrotor airfoils. Technical report, Airfoils Inc., Port Matilda, United States of America.
- Mayda, E. A. and van Dam, C. P. (2005). Automated Generation of Airfoil Performance Tables Using a Two-Dimensional Navier-Stokes Solver. *Journal of the American Helicopter Society*, 50(4):338–348.
- McCroskey, W. J., Baeder, J. D., and Bridgeman, J. O. (1986). Calculation of Helicopter Airfoil Characteristics for High Tip-Speed Applications. *Journal of the American Helicopter Society*, 31(2):3–9.
- McMasters, J. H. and Cummings, R. M. (2004). Rethinking the Airplane Design Process - An Early 21st Century Perspective. In *42nd AIAA Aerospace Sciences Meeting and Exhibit*, pages 2 – 26. American Institute of Aeronautics and Astronautics.
- Medida, S. and Baeder, J. (2011a). Application of the Correlation-based $\gamma - Re_{\theta t}$ Transition Model to the Spalart-Allmaras Turbulence Model. In *20th AIAA Computational Fluid Dynamics Conference*, pages 1–21, Honolulu, United States of America. American Institute of Aeronautics and Astronautics.
- Medida, S. and Baeder, J. (2011b). Numerical prediction of static and dynamic stall phenomena using the $\gamma - Re_{\theta t}$ transition model. In *American Helicopter Society 67 th Annual Forum, Virginia Beach, VA*.
- Meijerink, J. A. and van der Vorst, H. A. (1977). An iterative solution method for linear systems of which the coefficient matrix is a symmetric M -matrix. *Mathematics of Computation*, 31(137):148–162.
- Melin, T. (2000). *A Vortex Lattice MATLAB Implementation for Linear Aerodynamic Wing Applications*. Master’s thesis, Royal Institute of Technology (KTH).
- Melin, T. (2015a). Tornado - code development history. <http://tornado.redhammer.se/index.php/theory/changelog>. Accessed June 28th, 2018.
- Melin, T. (2015b). Tornado - documentation. <http://tornado.redhammer.se/index.php/documentation/documents>. Accessed June 28th, 2018.

- Melin, T. and Berard, A. Tornado - a vortex lattice method implemented in MATLAB. <http://tornado.redhammer.se/index.php>. development version T 135-001.
- Melnik, R. and Brook, J. (1985). The computation of viscous/inviscid interaction on airfoils with separated flow. In *3rd symposium on numerical and physical aspects of aerodynamic flows*, Long Beach, United States of America.
- Menter, F. R. (1993). Zonal Two Equation $k-\omega$ Turbulence Models For Aerodynamic Flows. In *24th Fluid Dynamics Conference*, pages 1–21, Orlando, United States of America. American Institute of Aeronautics and Astronautics.
- Merchant, A. and Drela, M. (1996). Design and Analysis of Supercritical Suction Airfoil. In *14th Applied Aerodynamics Conference*, pages 206–215. American Institute of Aeronautics and Astronautics.
- Meschia, F. (2008). Model analysis with XFLR5. *Radio Controlled Soaring Digest*, 25(2):27–51.
- Miranda, L. R., Elliot, R. D., and Baker, W. M. (1977). A Generalized Vortex Lattice Method for Subsonic and Supersonic Flow Applications. Technical Report NASA CR-2865, National Aeronautics and Space Administration, Hampton, United States of America.
- MIT Technology Licensing Office (2018). MSES - software for high lift multielement airfoil configurations. <https://tlo.mit.edu/technologies/mSES-software-high-lift-multielement-airfoil-configurations>. Accessed June 29th, 2018.
- Moran, J. (1984). *An Introduction to Theoretical and Computational Aerodynamics*. John Wiley & Sons, New York, United States of America.
- Morgado, J., Vizinho, R., Silvestre, M. A. R., and Páscoa, J. C. (2016). XFOIL vs CFD performance predictions for high lift low Reynolds number airfoils. *Aerospace Science and Technology*, 52(2016):207–214.
- Morino, L., Chen, L.-T., and Suciut, E. O. (1975). Steady and Oscillatory Subsonic and Supersonic Aerodynamics around Complex Configurations. *AIAA Journal*, 13(3):368–374.
- Mouch, T. N. and Lan, C. E. (1993). Computational Fluid Dynamics with Icing Effects. In *Aerotech '93*, SAE Technical Papers, pages 1–12, Costa Mesa, United States of America. SAE International.
- Müller, M., Liebenberg, L., Mathews, E. H., and Young, P. W. (2012). Quick estimates for analysis and prediction of the flight mechanics of unmanned aerial vehicles. *International Journal of Mechanical Engineering Education*, 40(2):121–145.
- Munguía, B. C., Economon, T. D., and Alonso, J. J. (2017). A Discrete Adjoint Framework for Low-Boom Supersonic Aircraft Shape Optimization. In *18th AIAA/ISSMO Multidisciplinary Analysis and Optimization Conference*, pages 1–11, Denver, United States of America. American Institute of Aeronautics and Astronautics.
- Mushynski, A. T. and Jon (2017). Analysis and Design of a Low Reynolds Propeller for Optimal Unmanned Aerial Vehicle (UAV) Flight. In *Proceedings of the ASME 2017 International Mechanical Engineering Congress and Exposition*, pages 1–11, Tampa, United States of America.
- Myers, A. (2012). Stanford software allows aero-engineering students to focus on aircraft design instead of computer code.
- Myring, D. F. (1970). An integral prediction method for three-dimensional turbulent boundary layers in incompressible flow. Technical Report 70147, Royal Aircraft Establishment, United Kingdom. Also published as Technical Report 32647 by the Aeronautical Research Council.
- Nanda, S. (2016). *Flow past a square-prism: A numerical study*. Master's thesis, Delft University of Technology, Delft, The Netherlands.

- Nash, J. F. and Hicks, J. G. (1968). An integral method including the effect of upstream history on the turbulent shear stress. In *Computation of turbulent boundary layers*, volume 1, Stanford, United States of America. Stanford University.
- Nathman, J. K. (2005). Induced Drag of High-Aspect Ratio Wings. In *43rd AIAA Aerospace Sciences Meeting and Exhibit*, pages 1–8, Reno, United States of America. American Institute of Aeronautics and Astronautics.
- Nathman, J. K. (2006). Potential-Based Panel Method for Oscillatory Motion. In *44th AIAA Aerospace Sciences Meeting and Exhibit*, pages 1–10, Reno, United States of America. American Institute of Aeronautics and Astronautics.
- Nathman, J. K. and McComas, A. (2008). Comparison of Stability and Control Calculations from Vortex Lattice and Panel Methods. In *46th AIAA Aerospace Sciences Meeting and Exhibit*, pages 1–7, Reno, United States of America. American Institute of Aeronautics and Astronautics.
- National Aeronautics and Space Administration. ARC2D (efficient two-dimensional solution methods for the navier-stokes equations). <https://software.nasa.gov/software/ARC-12112-1>. Accessed October 18th, 2018.
- National Aeronautics and Space Administration (1994). PMARC - panel method Ames Research Center. <https://ntrs.nasa.gov/search.jsp?R=19940002495>. Accessed October 21st, 2018.
- Omar, E., Zierten, T., Hahn, M., Szipro, E., and Mahal, A. (1973). Two-Dimensional Wind-Tunnel Tests of a NASA Supercritical Airfoil with Various High-Lift Systems: Volume II - Test Data. Technical Report CR-2215, National Aeronautics and Space Administration, Washington, United States of America.
- Padulo, M., Maginot, J., Guenov, M., and Holden, C. (2009). Airfoil Design under Uncertainty with Robust Geometric Parameterization. In *50th AIAA/ASME/ASCE/AHS/ASC Structures, Structural Dynamics, and Materials Conference*, pages 1–14, Palm Springs, United States of America. American Institute of Aeronautics and Astronautics.
- Palacios, F., Colonno, M. R., Aranake, A. C., Campos, A., Copeland, S. R., Economon, T. D., Lonkar, A. K., Lukaczyk, T. W., Taylor, T. W. R., and Alonso, J. J. (2013). Stanford University Unstructured (SU2): An open-source integrated computational environment for multi-physics simulation and design. In *51st AIAA Aerospace Sciences Meeting including the New Horizons Forum and Aerospace Exposition*, pages 1–60, Reston, Virginia. American Institute of Aeronautics and Astronautics.
- Palacios, F., Economon, T. D., Aranake, A. C., Copeland, S. R., Lonkar, A. K., Lukaczyk, T. W., Manosalvas, D. E., Naik, K. R., Padrón, A. S., Tracey, B., Variyar, A., and Alonso, J. J. (2014). Stanford University Unstructured (SU²): Open-source Analysis and Design Technology for Turbulent Flows. In *52nd Aerospace Sciences Meeting*, pages 1–33, National Harbor, United States of America. American Institute of Aeronautics and Astronautics.
- Palacios, F., Economon, T. D., Wendorff, A. D., and Alonso, J. J. (2015). Large-scale aircraft design using SU2. In *53rd AIAA Aerospace Sciences Meeting*, pages 1–20, Kissimmee, United States of America. American Institute of Aeronautics and Astronautics.
- Peyret, R. and Viviand, H. (1975). Computation of Viscous Compressible Flows Based on the Navier-Stokes Equations. Technical Report 212, North Atlantic Treaty Organization, Neuilly-Sur-Seine.
- Pini, M., Vitale, S., Colonna, P., Gori, G., Guardone, A., Economon, T., Alonso, J. J., and Palacios, F. (2017). SU2: the Open-Source Software for Non-ideal Compressible Flows. *Journal of Physics: Conference Series*, 821(2017):012013.
- Pletcher, R. H., Tannehill, J. C., and Anderson, D. A. (2012). *Computational Fluid Mechanics and Heat Transfer*. Taylor & Francis Group, Boca Raton, Florida, United States of America, 3rd edition.

- Popov, A. V., Botez, R. M., Mamou, M., and Grigorie, L. T. (2009). Variations in Optical Sensor Pressure Measurements due to Temperature in Wind-Tunnel Testing. *Journal of Aircraft*, 46(4):1314–1318.
- Potapczuk, M. G. (1988). Numerical Analysis of an NACA 0012 Airfoil with Leading-Edge Ice Accretions. *Journal of Aircraft*, 25(3):193–194.
- Pulliam, T. H. (1984). Euler and thin layer Navier-Stokes codes: ARC2D, ARC3D. In *Notes for computational fluid dynamics user's workshop*.
- Pulliam, T. H. (1986). Solution Methods In Computational Fluid Dynamics. In *Notes for the von Kármán Institute For Fluid Dynamics Lecture Series*.
- Pulliam, T. H. (1993). Time Accuracy and the Use of Implicit Methods. In *11th Computational Fluid Dynamics Conference*, pages 685–693. American Institute of Aeronautics and Astronautics.
- Pulliam, T. H., Jespersen, D. C., and Barth, T. (1986). Navier-Stokes Computations for Circulation Controlled Airfoils. In *18th Fluid Dynamics and Plasmadynamics and Lasers Conference*, pages 1–16. American Institute of Aeronautics and Astronautics.
- Pulliam, T. H., Jespersen, D. C., and Childs, R. E. (1983). An Enhanced Version of an Implicit Code for the Euler Equations. In *AIAA 21st Aerospace Sciences Meeting*, pages 1–16, Reno, United States of America. American Institute of Aeronautics and Astronautics.
- Pulliam, T. H. and Steger, J. L. (1978). On Implicit Finite-Difference Simulations of Three Dimensional Flow. In *AIAA 16th Aerospace Sciences Meeting*, pages 1–11, Huntsville, United States of America. American Institute of Aeronautics and Astronautics.
- Pulliam, T. H. and Steger, J. L. (1980). Implicit Finite-Difference Simulations of Three-Dimensional Compressible Flow. *AIAA Journal*, 18(2):159–167.
- Pulliam, T. H. and Steger, J. L. (1985). Recent Improvements in Efficiency, Accuracy and Convergence for Implicit Approximate Factorization Algorithms. In *23rd Aerospace Sciences Meeting*, Reno, United States of America. American Institute of Aeronautics and Astronautics.
- Pulliam, T. H. and Vastano, J. A. (1993). Transition to Chaos in an Open Unforced 2D Flow. *Journal of Computational Physics*, 105(1):133–149.
- QinetiQ. Our History - About us. <https://www.qinetiq.com/About-us/Our-History>. Accessed July 3rd, 2018.
- Raghunath, K., Rancour, D., and Mavris, D. N. (2014). Uncertainty propagation for a subsonic aircraft in a coupled fluid-structure interaction environment during conceptual design. In *15th AIAA/ISSMO Multidisciplinary Analysis and Optimization Conference*, pages 1–10, Atlanta, United States of America. American Institute of Aeronautics and Astronautics.
- Rajagopal, S. and Ganguli, R. (2009). Multidisciplinary Design Optimization of a UAV Wing Using Kriging Based Multi-Objective Genetic Algorithm. In *50th AIAA/ASME/ASCE/AHS/ASC Structures, Structural Dynamics, and Materials Conference*, pages 1–18, Palm Springs, United States of America. American Institute of Aeronautics and Astronautics.
- Rajagopal, S. and Ganguli, R. (2011). Multidisciplinary Design Optimization of Long Endurance Unmanned Aerial Vehicle Wing. *Computer Modeling in Engineering & Sciences*, 81(1):1–34.
- Ramanujam, G., Özdemir, H., and Hoeijmakers, H. W. M. (2016). Improving Airfoil Drag Prediction. In *34th Wind Energy Symposium*, pages 1–12, San Diego, United States of America. American Institute of Aeronautics and Astronautics.
- Raymer, D. P. (1992). *Aircraft Design: A Conceptual Approach*. American Institute of Aeronautics and Astronautics, Washington, D.C., United States of America, 2nd edition.

- Raymer, D. P. (2002). *Enhancing Aircraft Conceptual Design using Multidisciplinary Optimization*. Doctoral dissertation, Royal Institute of Technology, Stockholm, Sweden.
- Roe, P. L. (1981). Approximate Riemann Solvers, Parameter Vectors, and Difference Schemes. *Journal of Computational Physics*, 43(2):357–372.
- Roelofs, M. and Vos, R. (2018). Technology Evaluation and Uncertainty-Based Design Optimization: A Review. In *2018 AIAA Aerospace Sciences Meeting*, pages 1–21, Kissimmee, United States of America. American Institute of Aeronautics and Astronautics.
- Rose, M., Yaralian, H., Wagster, J., and Bhandari, S. (2012). Development and Validation of Flight Dynamics Model of a UAV Airplane. In *Infotech@Aerospace 2012*, pages 1–12, Garden Grove, United States of America. American Institute of Aeronautics and Astronautics.
- Roskam, J. (1985). *Airplane Design*. Roskam Aviation and Engineering Corporation, Ottawa, United States of America.
- Ross, D. S. (1987). Redesign of a Supercritical Wing in the Presence of an Engine Nacelle. *Journal of Computational Physics*, 73:233–243.
- Rumsey, C. L. and Slotnick, J. P. (2014). Overview and Summary of the Second AIAA High Lift Prediction Workshop (Invited). In *52nd Aerospace Sciences Meeting*, pages 1–37, National Harbor, United States of America. American Institute of Aeronautics and Astronautics.
- Sadraey, M. (2013). *Aircraft Design*. John Wiley & Sons, Ltd, Chichester, West Sussex, United Kingdom.
- Salichon, M. and Tumer, K. (2013). A neuro-evolutionary approach to control surface segmentation for micro aerial vehicles. *International Journal of General Systems*, 42(7):793–805.
- Salim, S. M., Ong, K. C., and Cheah, S. C. (2011). Comparison of RANS, URANS and LES in the Prediction of Airflow and Pollutant Dispersion. In *Proceedings of the World Congress on Engineering and Computer Science 2011*, volume II, pages 1–6, San Francisco, United States of America.
- Schippers, H. (1988). On the Evaluation of Aerodynamic Influence Coefficients. In *Notes on Numerical Fluid Mechanics, Volume 21: Panel Methods in Fluid Mechanics with Emphasis on Aerodynamics, Proceedings of the 3rd GAMM*, pages 210–219. Vieweg+Teubner Verlag, Kiel, Germany.
- Schmidt, K. (2013). *A Semi-Analytical Weight Estimation Method for Oval Fuselages in Conventional and Novel Aircraft*. Master's thesis, Delft University of Technology.
- Selig, M. S. (2003). Low Reynolds Number Airfoil Design Lecture Notes.
- Sforza, P. (2014). *Commercial Airplane Design Principles*. Butterworth-Heinemann / Elsevier, Oxford, United Kingdom, 1st edition.
- Shengjun, J., Chao, Y., and Zhifei, Y. (2016). Integrating Stanford University Unstructured Code with Transition Model. In *7th International Conference on Mechanical and Aerospace Engineering*, pages 573–577.
- Simpson, L. B. (1989). Unsteady Three-Dimensional Thin-Layer Navier Stokes Solutions on Dynamic Blocked Grids. Technical Report AFATL-TR-89-19, United States Air Force.
- Sinsay, J. D. and Nuñez, G. (2010). Toward Right-Fidelity Rotorcraft Conceptual Design. In *51st AIAA/ASME/ASCE/AHS/ASC Structures, Structural Dynamics, and Materials Conference*, pages 1–14. American Institute of Aeronautics and Astronautics.
- Sivellis, J. C. and Neely, R. H. (1947). Method for Calculating Wing Characteristics by Lifting-Line Theory Using Nonlinear Section Lift Data. Technical report, National Advisory Committee for Aeronautics, Washington, United States of America.

- Smith, A. M. O. (1957). Transition, pressure gradient, and stability theory. In *Proceedings of the 9th International Congress of Applied Mechanics*, volume 7, Brussels.
- Smith, A. M. O. and Gamberoni, N. (1956). Transition, pressure gradient, and stability theory. Technical Report ES 26388, Douglas Aircraft Company.
- Smith, P. D. (1972). An Integral Prediction Method for Three-Dimensional Compressible Turbulent Boundary Layers. Technical Report 3739, Aeronautical Research Council, London, United Kingdom.
- Spalart, P. R. (2000). Strategies for turbulence modelling and simulations. *International Journal of Heat and Fluid Flow*, 21(3):252–263.
- Spalart, P. R. and Allmaras, S. R. (1992). A one-equation turbulence model for aerodynamic flows. In *30th Aerospace Sciences Meeting and Exhibit*, pages 1–22, Reno, United States of America. American Institute of Aeronautics and Astronautics.
- Speziale, C. G. (1998). Turbulence Modeling for Time-Dependent RANS and VLES: A Review. *AIAA Journal*, 36(2):173–184.
- Steger, J. L. (1977). Implicit Finite Difference Simulation of Flow About Arbitrary Geometries with Application to Airfoils. In *AIAA 10th Fluid & Plasmadynamics Conference*, pages 1–14, Albuquerque, United States of America. American Institute of Aeronautics and Astronautics.
- Steger, J. L. and Pulliam, T. H. (1980). An Implicit Finite Difference Code for Inviscid and Viscous Cascade Flow. In *AIAA 13th Fluid & Plasma Dynamics Conference*, pages 1–14, Snowmass, United States of America. American Institute of Aeronautics and Astronautics.
- Stewartson, K. (1949). Correlated Incompressible and Compressible Boundary Layers. In *Proceedings of the Royal Society. Series A, Mathematical, Physical & Engineering Sciences*, pages 84–100.
- Stone, H. L. (1968). Iterative Solution of Implicit Approximations of Multidimensional Partial Differential Equations. *SIAM Journal on Numerical Analysis*, 5(3):530–558.
- Straathof, M. H. and van Tooren, M. J. L. (2011). Extension to the Class-Shape-Transformation Method Based on B-Splines. *AIAA Journal*, 49(4):780–790.
- Straathof, M. H., van Tooren, M. J. L., Voskuil, M., and Vos, R. (2010). Development and Implementation of Novel Parametrization Techniques for Multidisciplinary Design Initialization. In *51st AIAA/ASME/ASCE/AHS/ASC Structures, Structural Dynamics, and Materials Conference*, pages 1–17, Orlando, United States of America. American Institute of Aeronautics and Astronautics.
- Strang, W. Z., Berdahl, C. H., Nutley, E. L., and Murn, A. L. (1985). Evaluation of Four Panel Aerodynamic Prediction Methods (MCAERO, Pan Air, Quadpan, and VSAERO). In *AIAA 3rd Applied Aerodynamics Conference*, pages 1–16, Colorado Springs, United States of America. American Institute of Aeronautics and Astronautics.
- SU2 (2018). SU2, the open-source CFD code - docs. <https://su2code.github.io/docs/home/>. Accessed August 8th, 2018.
- su2code (2018). Releases su2code / SU2. <https://github.com/su2code/SU2/releases>. Accessed August 8th, 2018.
- Suwarantana, D. and Rodriguez, D. (2011). A More Efficient Conceptual Design Process Using the RAGE Geometry Modeler. In *49th AIAA Aerospace Sciences Meeting including the New Horizons Forum and Aerospace Exposition*, pages 1–10, Reston, Virginia. American Institute of Aeronautics and Astronautics.
- Swafford, T. W. (1980). Analytical Approximation of Two-Dimensional Separated Turbulent Boundary-Layer Velocity Profiles. Technical Report AEDC-TR-79-99, Arnold Air Force Station, Tennessee,

United States of America.

- Swafford, T. W. (1983). Analytical Approximation of Two-Dimensional Separated Turbulent Boundary-Layer Velocity Profiles. *AIAA Journal*, 21(6):923–926.
- Syms, G. F. (2006). Analysis of General-Aviation Aircraft Wing Sections. *Journal of Aircraft*, 43(4):1029–1035.
- Sytsma, H. S., Hewitt, B. L., and Rubbert, P. E. (1979). A Comparison of Panel Methods for Subsonic Flow Computations. Technical report, Advisory Group for Aerospace Research & Development.
- Tatineni, M. and Zhong, X. (1998). Numerical Simulations of Unsteady Low-Reynolds-Number Flows Over the APEX Airfoil. In *36th AIAA Aerospace Sciences Meeting and Exhibit*. American Institute of Aeronautics and Astronautics.
- The MathWorks (2017). MATLAB. <https://nl.mathworks.com/products/matlab.html>. Version R2017a (9.2.0.556344), 64-bit (win64).
- Thomas, J. L. and Salasf, M. D. (1986). Far-Field Boundary Conditions for Transonic Lifting Solutions to the Euler Equations. *AIAA Journal*, 24(7):1074–1080.
- Thomas, P. R. and Richardson, T. S. (2012). Estimation of Stability and Control Derivatives for a Piper Cub J-3 Remotely Piloted Vehicle. In *AIAA Modeling and Simulation Technologies Conference*, pages 1–26, Minneapolis, Minnesota. American Institute of Aeronautics and Astronautics.
- Thwaites, B. (1949). Approximate Calculation of the Laminar Boundary Layer. *Aeronautical Quarterly*, 1(3):245–280.
- Torenbeek, E. (1982). *Synthesis of Subsonic Airplane Design*. Springer-Science+Business Media, B.V., Dordrecht, The Netherlands.
- Troeger, L. P. and Selby, G. V. (1998). Computation of the Aerodynamic Characteristics of a Subsonic Transport. *Journal of Aircraft*, 35(2):183–190.
- Tysell, L. G. and Hedman, S. G. (1988). Towards a General Three-Dimensional Grid Generation System. In *ICAS Congress*, pages 1048–1058, Jerusalem, Israel.
- Vaithyanathasamy, R., Ozdemir, H., Bedon, G., and van Garrel, A. (2018). A double wake model for interacting boundary layer methods. In *2018 Wind Energy Symposium*, pages 1–15, Kissimmee, United States of America.
- van Craenenbroeck, J. (2016). *Boundary layer suction configurations with minimal pump requirements for multi-element airfoils*. Master's thesis, Delft University of Technology.
- van den Kieboom, K. T. H. and Elham, A. (2018). Concurrent wing and high-lift system aerostructural optimization. *Structural and Multidisciplinary Optimization*, 57(3):947–963.
- van der Vooren, J. (1989). Aircraft Drag Prediction for Transonic Potential Flow. In *Technical Status Review on Drag Prediction and Analysis from Computational Fluid Dynamics: State of the Art*, chapter 5, pages 1–17. Advisory Group for Aerospace Research & Development.
- van der Vooren, J. and van der Wees, A. J. (1991). Inviscid Drag Prediction for Transonic Transport Wings Using a Full-Potential Method. *Journal of Aircraft*, 28(12):869–875.
- van der Vooren, J., van der Wees, A. J., and Meelker, J. H. (1986). MATRICS, Transonic Potential Flow Calculations About Transport Aircraft. In *AGARD Symposium on Applications of Computational Fluid Dynamics in Aeronautics*, Aix-en-Provence, France.
- van der Wees, A. J. (1985). FAS Multigrid Employing ILU/SIP Smoothing: A Robust Fast Solver for

- 3D Transonic Potential Flow. In *2nd European Conference on Multigrid Methods*, pages 315–331, Cologne, Germany.
- van der Wees, A. J., van der Vooren, J., and Meelker, J. H. (1983). Robust calculation of 3D transonic potential flow based on the nonlinear FAS multi-grid method and incomplete LU decomposition. In *6th Computational Fluid Dynamics Conference Danvers*, pages 584–601.
- van der Wees, A. J., van Muiden, J., and van der Vooren, J. (1993). A Fast and Robust Viscous-Inviscid Interaction Solver for Transonic Flow about Wing / Body Configurations on the Basis of Full Potential Theory. In *AIAA 24th Fluid Dynamics Conference*, pages 1–9, Orlando, United States of America. American Institute of Aeronautics and Astronautics.
- van der Wees, A. J. and van Muijden, J. (1992). A robust quasi-simultaneous interaction method for a full potential flow with a boundary layer with application to wing/body configurations.
- van Ingen, J. L. (1956). A suggested semi-empirical method for the calculation of the boundary layer transition region. Technical Report V.T.H.-74., Technische Hogeschool, Delft, The Netherlands.
- van Ingen, J. L. (2008). The e^N method for transition prediction. Historical review of work at TU Delft. In *38th Fluid Dynamics Conference and Exhibit*, pages 1–49, Seattle, United States of America. American Institute of Aeronautics and Astronautics.
- van Muijden, J., Broekhuizen, A., van der Wees, A., and van der Vooren, J. (1996). Flow analysis and drag prediction for transonic transport wing/body configurations using a viscous-inviscid interaction type method. Technical Report TP 94161 U, Netherlands Aerospace Laboratory.
- Van Treuren, K. W. (2015). Small-Scale Wind Turbine Testing in Wind Tunnels Under Low Reynolds Number Conditions. *Journal of Energy Resources Technology*, 137(5):051208.
- Velázquez, O. E., Weiss, J., and Morency, F. (2017). Preliminary investigation on stall characteristics of a Regional BWB for low speed approach. In *35th AIAA Applied Aerodynamics Conference*, pages 1–17, Denver, United States of America. American Institute of Aeronautics and Astronautics.
- Venkateswaran, S., Li, D., and Merkle, C. L. (2003). Influence of Stagnation Regions on Preconditioned Solutions at Low Speeds. In *41st Aerospace Sciences Meeting and Exhibit*, pages 1–10, Reno, United States of America. American Institute of Aeronautics and Astronautics.
- Venters, R. and Helenbrook, B. (2013). A Numerical Investigation of High Lift Coefficient Airfoils Near Regions of Stall. In *Proceedings of the ASME 2013 Fluids Engineering Division Summer Meeting*, pages 1–9, Incline Village, United States of America.
- Vitale, S., Pini, M., Gori, G., Guardone, A. A., Economon, T. D., Palacios, F., and Alonso, J. J. (2015). Extension of the SU2 Open Source CFD code to the simulation of turbulent flows of fluids modelled with complex thermophysical laws. In *22nd AIAA Computational Fluid Dynamics Conference*, pages 1–22, Dallas, United States of America. American Institute of Aeronautics and Astronautics.
- Vogeltanz, T. (2015). Comparison of Open-Source CFD Software for Aerodynamic Analysis of Mini-UAV. In *AIAA/IEEE Digital Avionics Systems Conference*, pages 5E31–5E315. American Institute of Aeronautics and Astronautics.
- Vos, R. (2016). *FPPWiki - Synthesis/Initiator*. Delft, The Netherlands.
- Vos, R. and Farokhi, S. (2015). *Introduction to Transonic Aerodynamics*. Springer Science+Business Media B.V., Dordrecht, The Netherlands.
- White, F. M. (1991). *Viscous Fluid Flow*. McGraw-Hill, Inc., 2nd edition.
- Whitfield, D. L. (1978). Integral Solution of Compressible Turbulent Boundary Layers Using Improved Velocity Profiles. Technical Report AEDC-TR-78-42, Arnold Air Force Station, United States of Amer-

ica.

- Wilcox, D. C. (1988). Reassessment of the scale-determining equation for advanced turbulence models. *AIAA Journal*, 26(11):1299–1310.
- Wilcox, D. C. (2006). *Turbulence Modeling for CFD*. DCW Industries, Inc., 3rd edition.
- Williams, B. R. (1989). Coupling procedures for viscous-inviscid interaction in external aerodynamics. In *4th Symposium on Numerical and Physical Aspects of Aerodynamic Flows*, volume 16, Long Beach, United States of America.
- Xia, Y., Ajaj, R. M., and Friswell, M. I. (2014). Design and Optimisation of Composite Corrugated Skin for a Span Morphing Wing. In *22nd AIAA/ASME/AHS Adaptive Structures Conference*, pages 1–12, National Harbor, United States of America. American Institute of Aeronautics and Astronautics.
- Yaman, Y., Tunçöz, İ. O., Yang, Y., Arslan, P., Kalkan, U., Tıraş, H., Gürses, E., Şahin, M., and Özgen, S. (2015). Decamber Morphing Concepts by Using a Hybrid Trailing Edge Control Surface. *Aerospace*, 2(3):482–504.
- Yang, G. and da Ronch, A. (2018). Aerodynamic Shape Optimisation of Benchmark Problems Using SU2. In *2018 AIAA/ASCE/AHS/ASC Structures, Structural Dynamics, and Materials Conference*, pages 1–28, Kissimmee, United States of America. American Institute of Aeronautics and Astronautics.
- Yerly, E. T. (2016). *Investigation into Active Spanwise Camber Deformation on the Lateral Stability and Roll Control of the X-56A Compared to Conventional Ailerons*. Master's thesis, Air Force Institute of Technology, Ohio, United States of America.
- Yerly, E. T., DeLuca, A., and Joo, J. J. (2016). Investigation into Active Spanwise Camber Deformation on the Lateral Stability and Roll Control of the X-56A Compared to Conventional Ailerons. In *34th AIAA Applied Aerodynamics Conference*, pages 1–19, Washington, United States of America. American Institute of Aeronautics and Astronautics.
- Yoo, S., Summa, J. M., and Strash, D. J. (1990). Angle-of-Attack Validation of New Zonal CFD Method for Airfoil Simulations. In *8th Applied Aerodynamics Conference*, pages 704–712, Portland, United States of America. American Institute of Aeronautics and Astronautics.